

1 **Alpacas in Space - An Autobiography**
2

3 By
4

5 JOSEPH LEVINE
6 DISSERTATION
7

8 Submitted in partial satisfaction of the requirements for the degree of
9
10 DOCTOR OF PHILOSOPHY

11 in
12

13 Physics
14

15 in the
16

17 OFFICE OF GRADUATE STUDIES
18
19 of the
20

21 UNIVERSITY OF CALIFORNIA
22

23 DAVIS
24

25 Approved:
26

27 J. Anthony Tyson, Chair
28

30 S. Mani Tripathi
31

33 Brian Kolner
34

36 Committee in Charge
37

38 2025

39

Abstract

40 comment: This is my qual write up and is here only as a place holder. Don't edit this
41 yet It is believed that a large majority of the mass in the universe comes from an as yet
42 undetermined source. This claim stems originally from work performed in 1933 by Fritz
43 Zwicky who noticed a discrepancy between measured velocities of galaxies within the Coma
44 Cluster and velocities predicted by applying the virial theorem. He wrote

45 *If this [experimental result] would be confirmed we would get the surprising result
46 that dark matter is present in much greater amount than luminous matter [1].*

47 Vera Rubin furthered this work by measuring velocities of stars rotating in the M31 galaxy
48 and concluded there must be additional non-luminous mass (originally published in [2],
49 and shown in Fig.0.1). Studies of other phenomena, such as lensing (see [**lensing2**]) have
50 confirmed the existence of this dark matter, and it is currently one of the major mysteries
51 in modern physics.

52 Since the 1980's, the leading theories have consisted of an unknown species of elementary
53 particle. The search for weakly interacting massive particles (WIMPs) have dominated
54 the budgets and schedules of the dark matter search effort but have yet to provide any
55 experimental evidence.

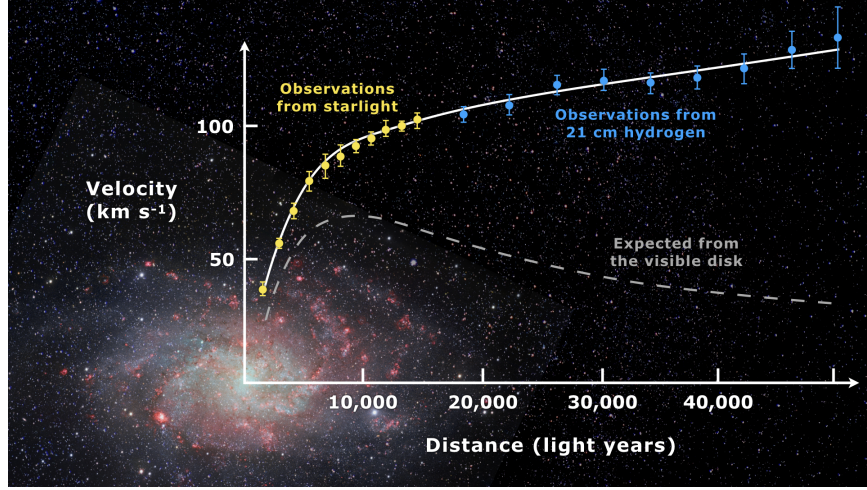


Figure 0.1: Expected vs observed velocity distributions of M33

56 In light of this, the 2017 community report on dark matter [3] highlights a need for a multi-
 57 experiment program in which many small scale experiments (< \$10M) split up to cover the
 58 vast landscape of potential dark matter candidates (see Fig. 0.2). Since very little is known
 59 about the dark matter, it is a playground for theoretical physicists to invent candidates.
 60 This overwhelming search should be narrowed down.

61 The enormous mass range splits nicely into two regimes; waves and particles. At a mass of
 62 order 1eV the inter-particle spacing \approx wavelength. Lighter than this it is more convenient
 63 to think of dark matter as a wave. Alternatively, dark matter candidates heavier than this
 64 are more conveniently modeled as exhibiting particle-like behavior. The Dark E-Field Radio
 65 experiment searches for dark photons in the nano- to milli-eV mass range where dark matter
 66 is best described as a wave. This property means one would search for a dark photon using
 67 wave-like detectors, e.g. antennas.

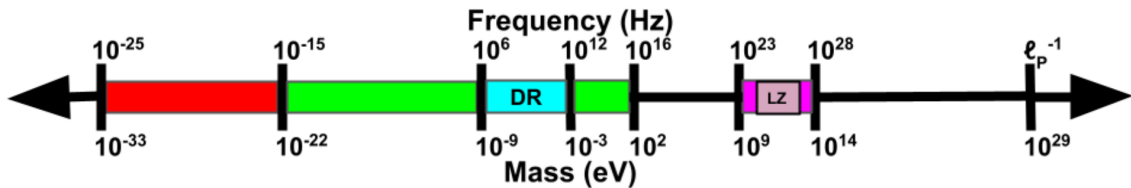


Figure 0.2: Cartoon depicting the mass scales over which dark matter may be found. Corresponding frequencies shown above. At heavy mass scales $> \mathcal{O}(1\text{ eV})$ the dark matter would behave like a particle, while on the lighter end it would behave like a wave. The Dark Radio Experiment searches at radio/microwave frequencies (blue) for a hidden photon using an antenna and spectrum analyzer. LUX-ZEPLIN Experiment (LZ) also shown.

68 comment: Discussion from paper. Good to pull from

69 This experiment extends the earlier results of our pilot experiment [4], which was designed to
 70 demonstrate feasibility of the Dark E-field Radio technique. The pilot experiment was run
 71 over the same frequency range as the experiment reported here, but did not make use of the
 72 calibration techniques to approximate statistical uniformity, nor did it fully account for the
 73 resonant enhancement of the cavity. In this paper we describe how we randomize antenna
 74 positions by moving it many times during the run. In addition, we detail EM simulations
 75 which give the average relation between the E-field at the antenna and the voltage into
 76 the LNA, accounting for resonant enhancement of the cavity. A 2^{24} -point FFT produces a
 77 spectrum dominated by background thermal noise which varies gradually with frequency.

78 We then searched over the full 50-300 MHz frequency span for any narrow-band dark photon
 79 signal of at least 5% global significance. Optimally filtering the resulting spectrum, we detect
 80 a single candidate which we are able to identify as interference, likely from our electronics.

81 Rejecting this candidate, we obtain a null result for any signal which could be attributed
82 to the dark photon in our frequency range. The resulting 95% exclusion limit for the dark
83 photon kinetic coupling ϵ is then obtained over this mass range of 0.2-1.2 μeV . Our null result
84 is a factor of ≈ 100 more sensitive than current astrophysical limits.

85 Ultimately, we can apply this detection technique at higher frequencies, ultimately going up
86 to the sub-THz band. This will require new antennas and microwave electronics. Cryogenic
87 cavities and LNAs could improve our sensitivity by an order of magnitude.

88 **Contents**

89	Contents	vi
90	List of Figures	ix
91	List of Tables	xii
92	1 The Dark Matter Story	1
93	1.1 The History of Dark Matter	2
94	1.1.1 Early ideas in dark matter	2
95	1.1.2 Into the modern era	3
96	1.1.2.1 Galactic rotation curves	7
97	1.1.3 Local dark matter density measurements	7
98	1.2 From “History” to “Current Events”	7
99	1.2.1 Modern evidence and observations of dark matter	8
100	1.2.1.1 The cosmic microwave background	8
101	1.2.1.2 Gravitational lensing	8
102	1.2.1.3 MOND and the bullet cluster	8
103	1.3 MACHOs, WIMPs and WISPs, oh my!	8
104	1.4 Dark Photon Physics	9
105	1.5 Detection Strategy: a Resource Allocation Problem	9
106	2 Experiment Overview and Design	10
107	2.1 Sources of Power in Measured Spectrum	13
108	2.1.1 Thermal Noise	13
109	2.1.1.1 Blackbody Electric Field Density	13
110	2.1.1.2 Antenna Noise	16
111	2.1.1.3 Dicke radiometer equation	19
112	2.1.2 Dark Photon Signal	24
113	2.1.3 Radio Frequency Interference	26
114	2.1.4 Amplifier Chain Noise	27
115	2.1.5 ADC effects	31
116	2.1.5.1 Spurious signals	32
117	2.1.5.2 ADC noise	32

118	2.2	Toy Analysis	33
119	2.2.1	Signal significance	34
120	2.2.1.1	Computing an exclusion limit	37
121	2.2.2	Predicted time to detection	41
122	2.3	Thermal Noise in A Cavity: Thermal Wiggles ®	42
123	2.3.1	Theory of thermal radiation in a cavity	42
124	2.3.2	Inspection of thermal noise spectra	46
125	2.3.3	A simple resonator: shorted coax cable	47
126	2.3.3.1	RF circulators	50
127	2.3.4	A simpler resonator: shorted coax cable and circulator	53
128	2.3.5	A more complex resonator: antenna in room	54
129	2.3.6	Effective temperature of amplifier	55
130	2.3.7	Intentional breaking of thermal equilibrium	59
131	2.3.8	Relation of antenna S_{11} to thermal noise without a circulator	59
132	2.4	Reverberation Chambers and Statistical Uniformity	60
133	2.5	System Design	60
134	2.5.1	Shielded room	63
135	2.5.2	Antenna	64
136	2.5.3	Terminator and fiber-optic switch control	68
137	2.5.4	Signal conditioning	68
138	2.5.4.1	Low noise amplifier	69
139	2.5.4.2	Secondary amplifier	69
140	2.5.4.3	Band pass filter	70
141	2.5.4.4	Putting together a signal conditioning chain	71
142	2.5.5	Veto antenna	74
143	2.5.6	12 V power system	75
144	2.5.7	GPU-Based Real-Time Spectrum Analyzer	78
145	3	System Characterization and Data Acquisition System	82
146	3.1	Measurement of Amplifier Chain Performance	83
147	3.1.1	Y-factor method	83
148	3.1.2	Confirming gain with tracking generator measurement	92
149	3.1.3	System stability over a run period	93
150	3.2	Measurement of shielding effectiveness and radio frequency interference	97
151	3.3	Spectrum Analyzer Characterization	103
152	3.3.1	Spectrum analyzer calibration	103
153	3.3.2	Spurious signal performance of the ADC	104
154	3.3.3	ADC clock performance	106
155	3.3.4	Real-time data collection efficiency	107
156	4	Data Acquisition, Data Analysis and Calibration	109
157	4.1	Data Acquisition	111
158	4.1.1	Raw data, S_o	112

159	4.2 Data Analysis	115
160	4.2.1 Fit background, $\hat{\mathbf{B}}(\nu)$	117
161	4.2.2 Normalized spectrum, $\mathbf{S}_o^{\text{norm}}$	119
162	4.2.3 Signal-matched filter	120
163	4.2.4 Monte carlo: pseudo experiments	123
164	4.2.5 Rejection of a single candidate	128
165	4.3 Calibration	129
166	4.3.1 Average effective aperture, $\langle \mathbf{A}_e(\nu) \rangle$	130
167	4.3.2 Simulation of $\langle \tilde{Q} A_e \rangle$	131
168	4.3.3 Correction and uncertainty of $\langle \tilde{Q} A_e \rangle$	134
169	4.4 Hardware Injection Test	138
170	4.4.1 Injection test prerequisites	138
171	4.4.1.1 Determination of required injected power	138
172	4.4.1.2 Proxy dark photon signal injection	141
173	4.4.2 Performing the injection test	143
174	4.4.3 Inspection of Data	147
175	4.5 Results	151
176	4.5.1 Discussion of uncertainties	151
177	5 Beyond 300 MHz	154
178	5.1 Preliminary Run 1B results	155
179	5.2 Mixer System	155
180	5.3 Cryogenics	155
181	A Overview of RTSA code base	156
182	A Tips for using the RTSA system	158
183	B Data structure and processing	159
184	B.1 Writing data	159
185	B.2 Reading and averaging data	163
186	Bibliography	166

¹⁸⁷ List of Figures

188	0.1	Expected vs observed velocity distributions of M33	iii
189	0.2	Dark matter mass regimes	iv
190	2.1	Overview of Dark E-field Radio experiment	12
191	2.2	Blackbody electric field spectral density from radio to UV frequencies	15
192	2.3	An antenna and matched resistor in cavities which are in thermal equilibrium.	18
193	2.4	Simulated antenna noise voltage at room temperature in the time domain	20
194	2.5	Simulated antenna noise power spectral density at room temperature in the frequency domain	21
195	2.6	Effect of averaging on simulated antenna noise power spectral density at room temperature in the frequency domain	23
196	2.7	Schematic of LNA adding input referred noise	27
197	2.8	Schematic of cascade of amplifiers and their added noise	29
198	2.9	Cascaded noise temperature for system with two amplifiers	30
199	2.10	Input-referred power spectral density from simplified simulation	35
200	2.11	Noise spectrum containing sub-detection-threshold signal	38
201	2.12	Noise spectrum containing sub-detection-threshold signal, various number of averages	40
202	2.13	Predicted time to detection for the toy analysis spectra	41
203	2.14	Two cavities in thermal equilibrium of arbitrary shape, material and physical contents contain equivalent radiation fields	44
204	2.15	A cavity with a small hole behaves like a black body as long as the probability of absorption << 1. The probability of absorption at each reflection is given by the emissivity, so the total probability of <i>reflection</i> is the emissivity raised to the power of the average number of bounces. Figure from Wikipedia.	45
205	2.16	Output-referred vivaldi antenna and terminator spectra as measured through Run 1A amplifier chain	47
206	2.17	A coax cable with a short on the end and a matched measurement device on the other behaves like a “closed-open” resonator.	48
207	2.18	Power spectrum of short and open terminations at the end of 1.85 m of RG400 coax cable	49
208	2.19	Schematic symbol of a circulator	50
209	2.20	Photo of Teledyne C-0S03A-3M RF circulator	51
210	2.21	3-port, frequency dependant S-parameter data for Teledyne C-0S03A-3M circulator	52

221	2.22	A coax cable with a short on one end and a circulator isolating the system from the amplifier.	53
223	2.23	Power spectrum of 185 cm coax resonator as measured through circulator.	54
224	2.24	Schematic of experimental set-up using circulator to isolate antenna from amplifier effects	55
226	2.25	Normalized power spectrum for vivaldi antenna in room with circulator	56
227	2.26	Schematic of set-up to measure the noise emerging <i>out</i> of an amplifiers input	57
228	2.27	Power spectrum of noise emerging <i>out</i> of the input of an amplifier's input	58
229	2.28	Schematic of the RF receiver system	61
230	2.29	Photo of dark radio lab	62
231	2.30	AB-900A biconical antenna free space effective aperture, simulated, measured and theoretical	66
233	2.31	simulated AB-900A biconical antenna free space complex input impedance, vs measured biconical data	67
235	2.32	Through gain (S_{21}) of bandpass filter	73
236	2.33	Schematic of Run 1A Amplifier chain	74
237	2.34	Schematic of Interlock board	76
238	2.35	Photo of lead-acid battery and slow turn on circuit	77
239	2.36	Real time DAQ data stream.	80
240	3.1	Cartoon showing Y-factor data	84
241	3.2	Cryogenic hardware setup for the Y-factor measurement.	86
242	3.3	Raw output power spectra used to compute the gain and noise temperature for the Run 1.4 amp chain using the Y-factor method	87
244	3.4	Y-factor data from Run 1.4 amp chain at a single frequency (625 MHz)	88
245	3.5	Frequency dependent noise temperature of Run 1.4 amplifier chain, measured using the Y-factor method	89
247	3.6	Frequency dependent gain of the Run 1.4 amplifier chain, measured using the Y-factor method	90
249	3.7	Run 1.4 terminator, input-referred power spectral density	91
250	3.8	Gain vs. frequency of Run 1.4 amplifier chain	92
251	3.9	Gain vs. LNA voltage of Run 1.4 amplifier chain	94
252	3.10	Voltage at LNA vs. time	95
253	3.11	Frequency-averaged power vs. time of the terminator from Run 1.4	96
254	3.12	Photo of setup to measure Shielding effectiveness of shielded room	99
255	3.13	Shielding effectiveness of shielded room, 50-300 MHz	100
256	3.14	Shielding effectiveness of shielded room, 125-3000 MHz	101
257	3.15	Spectrum from veto antenna during 300 MHz data run	102
258	3.16	Scan of terminated input of Teledyne spectrum analyzer system to measure spur performance	105
260	3.17	Acquisition efficiency for GPU-based Real-time spectrum analyzer	108
261	4.1	Run 1A averaged, output-referred antenna power spectrum S_o	113

262	4.2	Run 1A averaged, output-referred, antenna and terminator power spectra	114
263	4.3	Flow chart outlining the logic of signal processing in the detection algorithm of sections 4.2.1 through 4.2.3.	116
265	4.4	Fitting background \hat{B} in the presence of a synthetic signal.	119
266	4.5	Normalized, output-referred power spectrum S_o^{norm}	121
267	4.6	S_o^{norm} after it has been passed through a matched filter.	123
268	4.7	Result of Monte Carlo pseudo experiments on signal detection.	126
269	4.8	Limit on output-referred total integrated signal power, P_o^{lim}	127
270	4.9	Screenshot of COMSOL simulation GUI for two-antenna validation	133
271	4.10	Simulated vs measured $\langle S_{21} \rangle$	134
272	4.11	Corrected average effective aperture.	136
273	4.12	Schematic of hardware injection test	139
274	4.13	Average S parameters of hardware injection test	140
275	4.14	Histogram of frequencies used for hardware injection test	143
276	4.15	Output-referred power spectral density from the hardware injection test	145
277	4.16	Standard deviation of output-referred power spectral density from the hardware injection test, computed with median absolute deviation	146
279	4.17	Output-referred power spectrum from hardware injection test, various levels of zoom	148
281	4.18	Normalized, output-referred power spectrum from hardware injection test, various levels of zoom	149
283	4.19	Matched filtered, output-referred power spectrum from hardware injection test, various levels of zoom	150
285	4.20	Zoom of 95 % exclusion limit on ϵ from Dark E-field Radio run 1A	152
286	4.21	Dark photon limits of various experiments with this work shown in red	153
287	A.1	Real-time heads up window for data acquisition.	162

²⁸⁸ List of Tables

289	2.1	Statistics of simple Monte Carlo simulation for probability of signal detection in the toy analysis	42
290	2.2	Direction, coordinate, and length measurements of shielded room in lab 314. Note that Fig. 2.29 is looking south, so x is right-left and z in into the page. Note that these are the mean values of several measurements. The room was found to be about 5mm out of square, so these should be interpreted as ± 5 mm.	64
291	2.3	Specifications for the Pasternack PE15A1012-E. The voltage is regulated internally, so the exact voltage supplied is not critical, though there is a slight gain dependence on voltage since a higher voltage causes the amp to run warmer, see Fig 3.9.	69
292	2.4	Specifications for the Mini-Circuits ZKL-1R5+ as measured with 9.05 V bias. There is no internal regulator, so the voltage is set using an external regulator (built around a TI LM317 [49]).	70
293	2.5	Specifications for the custom, real time spectrum analyzer used for run 1A.	79
303	4.1	Run 1.4 Details. Many specifications are related and can be computed from each other but are listed for reference. Efficacy differs from calculation in Fig. 3.17 mainly because of switching to terminator and brief daily pauses to move the antenna.	111
304	4.2	Threshold parameters that are part of the detection algorithm and Monte Carlo. X is the significance of the analysis. It is a parameter passed to the detection algorithm which specifies the significance threshold. The quantity $100\% - Y$ is the statistical power of the analysis. It is a parameter in the MC, which specifies a threshold on signal power where a given signal is detected in $100\% - Y$ of the MC iterations. We choose both X and Y = 5%.	125
313	A.1	Example database file.	160

314

Acknowledgments

315 Thank you to: Ben

316 Dave Hemmer

317 Nathan IT

318 Monda

319 emiljia

320 Bill Tuck

321 Buchholtz/Ayars/Nelson/Kagan/Clare/Patrova/Rick Danner/pechkis

322 parents

323 janet/joel

324 baba/papa

325 Belva

326 chatGPT

327 Mr Keye

328 Bill Nye

329 pechkis

330 Self plagiarism statement <https://journals.aps.org/copyrightFAQ.html>

331 As the author of an APS-published article, may I include my article or a portion
332 of my article in my thesis or dissertation? Yes, the author has the right to use
333 the article or a portion of the article in a thesis or dissertation without requesting
334 permission from APS, provided the bibliographic citation and the APS copyright
335 credit line are given on the appropriate pages.

336 <https://grad.ucdavis.edu/preparing-filing-your-thesis-or-dissertation>

337 Published or publishing pending material may be used with permission from the
338 copyright owner, if not you, and the Graduate Chair, if you are not the first-
339 author. See the Copyright FAQ for information about permissions when using
340 published material.

341 Material you have authored, and which has been previously published or is pend-
342 ing publishing, may be used in its published format with three exceptions: 1)
343 Margins - You must maintain 1" margins on all sides throughout the paper. 2)
344 Pagination - page numbers must follow the UC Davis standards. 3) The title
345 page must follow UC Davis standards and you must include an overall abstract.

346 comment: Need to add note about github and where code comes from

³⁴⁷ Chapter 1

³⁴⁸ The Dark Matter Story

349

If we start making a list of things that aren't here, we could be here all night. You know, pens for instance. Let's stick with things we can see.

Wheatley

350 While there are many ways to begin a thesis on a dark matter search (of which many
351 hundreds are written every year), I have opted to prioritize narrative over completeness. I
352 will aim to answer the following questions:

- 353 • Why do we believe there to be some mysterious “dark matter” which we can’t even
354 see?
- 355 • Can we back up this prediction?
- 356 • What is the best way to balance answering this question with the economic reality of
357 finite money?

358 There will be a few digressions along the way, however the goal of this chapter is simply
359 to motivate what brought society to the point of paying young scientists to put antennas in
360 metal boxes and measure noise.

361 **1.1 The History of Dark Matter**

362 **1.1.1 Early ideas in dark matter**

363 The fundamental idea that things exist which can not be easily observed by human senses is
364 not a new one. Following a long history of discovery of previously unobserved phenomena,
365 the study of dark matter began to take shape around the end of the 19th century with the
366 discovery of dark regions among areas with a high density of stars [5]. It was Lord Kelvin
367 who began a dynamical study of the motions of stars in order to tease out the weight of

368 the luminiferous aether (who's "existence is a fact that can not be questioned" as stated
369 in his 1901 lecture which is transcribed on page 260 of [6]). Eventually the theory of the
370 aether would give way to special relativity, which ruled out a potential candidate for the
371 dark regions. This proposing of dark matter candidates and their rejection is a cycle that
372 continues to this day, and is the topic of this thesis.

373 1.1.2 Into the modern era

374 1905, known as Einstein's miracle year, ushered in a new era of "modern physics". The
375 aether that Lord Kelvin was trying to weigh was accepted as non-existent, but that didn't
376 answer the questions of galactic dynamics which were posed by those who believed in it.
377 Fritz Zwicky is credited with the first discovery of dark matter in 1933 [1], though it was
378 not widely accepted at this time. This lack of acceptance was in part due to his technique
379 of "morphological analysis" which is similar to arranging refrigerator magnets to arrive at
380 creative solutions¹. The many "creative" solutions are simultaneously to the benefit and
381 detriment of this technique. To quote Stephen Maurer[7],

382 *When researchers talk about neutron stars, dark matter, and gravitational lenses,*
383 *they all start the same way: "Zwicky noticed this problem in the 1930s. Back then,*
384 *nobody listened..."*.

385 It even seems if Zwicky himself didn't believe his own result[1],

¹This analogy is from a class I took from Andrew Wetzel at U.C. Davis. In researching it for this thesis, it is surprisingly accurate

386 *If this [experimental result] would be confirmed we would get the surprising result*
387 *that dark matter is present in much greater amount than luminous matter [1].*

388 comment: Tony summarizes virial therm this in his '97 physics today article [8] In retrospect
389 however, this idea is seemingly on firm theoretical footing. The viral theorem is a well known
390 from statistical mechanics. It was formalized 1870 by Rudolf Clausius (English translation
391 can be found here [9]). The name *virial* was coined by Clausius. Kinetic energy was, at
392 the time, referred to as *vis viva* latin for “living force”. The plural of vis is virias, and
393 since the theorem is concerned with many particles each with their own vis via the name
394 *virial* theorem was chosen. The theorem is derived briefly here (following chapter 3 of
395 Goldstein[10]) since it is informative, however the reader can skip to Eq. 1.6 for the result
396 as it applies to galacite dynamics.

397 The “virial” the system is defined as

$$G \equiv \sum_{i=1}^N \mathbf{r}_i \cdot \mathbf{p}_i \quad (1.1)$$

398 Where \mathbf{r}_i is the position of the ith particle and \mathbf{p}_i is it's momentum, $m_i \mathbf{v}_i$.

399 By the product rule, the time derivative of G is

$$\dot{G} = \sum_{i=1}^N (\dot{\mathbf{r}}_i \cdot \mathbf{p}_i + \mathbf{r}_i \cdot \dot{\mathbf{p}}_i) . \quad (1.2)$$

400 Since the first term is really $m_i \mathbf{v}_i \cdot \mathbf{v}_i$ it can be seen as twice the kinetic energy, $2T$. The
401 second term can be simplified by Newton's second law, $\mathbf{F} = \dot{\mathbf{p}}$. So,

$$\dot{G} = 2T + \sum_{i=1}^N (\mathbf{r}_i \cdot \mathbf{F}_i) . \quad (1.3)$$

Solving for the time-averaged, time-derivative of G ,

$$\begin{aligned}\bar{\dot{G}} &= \frac{1}{T} \int_0^\tau dt \dot{G} \\ &= \frac{G(\tau) - G(0)}{\tau}\end{aligned}$$

402 Where T is the period the average is taken over, not to be confused with the Kinetic energy.

403 In the case that the system is bound together (i.e. $\mathbf{r}_i, \mathbf{p}_i > \infty$), G is finite and as τ
404 approaches ∞ , $\bar{\dot{G}}$ approaches 0

405 Returning to Eq. 1.2, we can now say

$$\overline{T} = -\frac{1}{2} \overline{\sum_{i=1}^N (\mathbf{r}_i \cdot \mathbf{F}_i)}, \quad (1.4)$$

406 A familiar statement of the virial theorem, where the term on the right hand side is
407 known as *the virial of Clausius*.

408 While incredibly general (one can pull the ideal gas law out of this in just a few steps,
409 see again Ch. 3 of Goldstein [10]), we are concerned not with a jar filled with gas in some
410 lab, but with “gas” of stars (among which all labs are contained!).

411 To specify the equation to that of galactic dynamics, recognize for a conservative central
412 force, $\mathbf{F} = -\nabla U$ and $\mathbf{r} \cdot \mathbf{F} = rF$. If U is in a power law, i.e. of the form $k r^{n+1}$, it can quickly
413 be seen that the virial of Clausius of Eq. 1.4 can be written $\frac{n+1}{2} \overline{U}$.

414 For a problem involving an inverse square force as we are concerned with, $n = -2$, and we
415 arrive at the well known result which is usually just called “the virial theorem”, though as we
416 have seen, it reaches much deeper than a simple statement of kinetic vs potential energies
417 for galaxies:

$$\overline{T} = -\frac{1}{2}\overline{U}. \quad (1.5)$$

418 Finally following Edington's 1916 paper [11] we can form a useful formula which ul-
 419 timately gave a clue to the existence of dark matter. By setting $T = 1/2M\overline{v^2}$ and $U =$
 420 $GM^2/2R$ where M is the total mass of a cluster or galaxy, v is it's velocity, and R is it's
 421 radius, we arrive at

$$M \approx \frac{2R\overline{v^2}}{G} \quad (1.6)$$

422 As pointed out by Bertone [12], one of the earliest "clean" arguments for the existence
 423 of dark matter is known as the timing argument. It was derived by Kahn and Woltjer [13].
 424 The basic idea is given the negative red-shift (i.e. blue-shift) of the Andromeda galaxy, they
 425 are approaching (at 125 [km/s]), an indication that they are bound system. Given that the
 426 period of this system must be less than the age of the universe (assumed to be 10^{10} [yr]), a
 427 lower bound can be set on the reduced mass of the system (since orbital period T is inversely
 428 proportional to the reduced mass).

429 In the years following these arguments, WWII brought unprecedeted destruction, the
 430 reconstruction of which slowed the progress of all science that was not essential to the war
 431 effort, especially in Europe. The focus astronomy and astrophysics largely shifted to stellar
 432 structure and evolution, in large part due to the work and understanding of nuclear reactions
 433 around this time. The war also brought with it advances in radar technology. At the end of
 434 the war, the German occupation forces left large amounts of radar equipment strewn about

435 Europe. This included a large number of 7.5 [m] Würzburg antennas designed to 54[cm]
436 aircraft radar, but were also sensitive to the famous Hydrogen 21[cm] line [14]. This would
437 play a major roll in what was to come.

438 **1.1.2.1 Galactic rotation curves**

439 **1.1.3 Local dark matter density measurements**

440 comment: Add plots of local dark matter density estimate. <https://arxiv.org/pdf/1404.1938>
441 <https://arxiv.org/pdf/2201.01822> <https://arxiv.org/pdf/2305.13358>

442 **1.2 From “History” to “Current Events”**

443 As pointed out by Trimble, “Practicing scientists will normally put the cut between history
444 and current events at the time when they started reading the literature for themselves,
445 probably early in graduate school.” [15]. While that puts my personal cut off around 2020,
446 the cut off of the Dark E-field Radio group is closer to the mid-1960’s; a fruitful time for
447 research into dark matter.

448 A characteristic shift in the dark matter problem takes place in this era of current events.
449 Instead of asking “is there dark matter (and if so how much)”, we ask “what is this stuff?!”.
450 To be sure, the first question is still relevant today and the ever more precise answer was
451 outlined in Sec. 1.1.3. This section is concerned with more modern evidence for dark matter,
452 which tend to point to the modern non-baryonic particle models, which the Dark E-Field
453 Radio Experiment is searching for.

454 **1.2.1 Modern evidence and observations of dark matter**

455 **1.2.1.1 The cosmic microwave background**

456 Billy and Ben's thesis

457 **1.2.1.2 Gravitational lensing**

458 -ben thesis

459 -tony 92 article// -J. A. Tyson, G. P. Kochanski, and I. P. Dell'Antonio, Detailed mass map

460 of CL0024+1654 from strong lensing

461 **1.2.1.3 MOND and the bullet cluster**

462 -history of dark matter bertone

463 - billy and ben

464 - D. Clowe, M. Bradac, A. H. Gonzalez, M. Markevitch, S. W. Randall, et al., A direct

465 empirical proof of the existence of dark matter,

466 **1.3 MACHOs, WIMPs and WISPs, oh my!**

467 -Billy thesis sec 1.2

468 - G. Bertone, D. Hooper, and J. Silk, Particle dark matter: Evidence, candidates and con-

469 straints

⁴⁷⁰ **1.4 Dark Photon Physics**

⁴⁷¹ - Ben's thesis

⁴⁷²

$$|\mathbf{E}_{\text{ant}}| \approx \epsilon \sqrt{\frac{2}{\varepsilon_0} \rho_{\text{DM}}}, \quad (1.7)$$

⁴⁷³ Tony says 9/23/25 – Production mechanisms: fluctuation occurs early in inflation or mis-
⁴⁷⁴ alignment mechanism.

⁴⁷⁵

⁴⁷⁶ Point out that DP doesn't have a thermal origin like a WIMP does

⁴⁷⁷ **1.5 Detection Strategy: a Resource Allocation**

⁴⁷⁸ **Problem**

⁴⁷⁹ - US Cosmic Visions 2017

⁴⁸⁰

⁴⁸¹ Chapter 2

⁴⁸² Experiment Overview and Design

⁴⁸³

A month in the laboratory can often save an hour in the library.

Frank Westheimer

484 Veljko Radeka said of detectors “One would imagine that in each particular case the best
485 solution is arrived at by 1) the detector design to maximize the significant signal, 2) reduction
486 of noise at its physical source, and 3) optimum filtering of signal and noise.” [16]. While
487 he was referring to position sensitive particle detectors, the same three principles apply to
488 this experiment. Put more directly, the goal is to maximize the signal to noise ratio. The
489 detector in this case is a low-noise, wide-band radio receiver system searching not for discrete
490 instances of particle-like interactions, but for coherent waves which are constant over long
491 periods. The signal is a small excess of narrow-band, radio frequency power received by an
492 antenna in a cavity. The noise is the white, thermal background due to the 300 K walls. An
493 overview of the entier experiment is shown in Fig. 2.1.

494 This chapter begins with Sec. 2.1, devoted to exploring the sources of power in the mea-
495 sured spectrum. It walks through several back-of-the-envelope calculations to follow the
496 signal and noises as they progress from fields in free space through a simplified detector.
497 Section 2.2 takes the next step; it simulates these signals and noises and shows a frame-
498 work for statistical data analysis. These two sections serve to build up intuition about the
499 experiment which will explain design choices discussed in the later chapters. Furthermore,
500 this section is useful because the actual experiment will report a null result, i.e. a lack of
501 detection of a signal on a background. By following a signal *forward* through the system
502 and toy data analysis, it will be more clear how to infer an exclusion limit from a power
503 spectrum and working *backward* through the experiment. In the following two sections, 2.3
504 and 2.4, effects will be introduced that were not apparent from the simplistic analysis of
505 the first section. The final section, 2.5, details each piece of the system. Measurements of

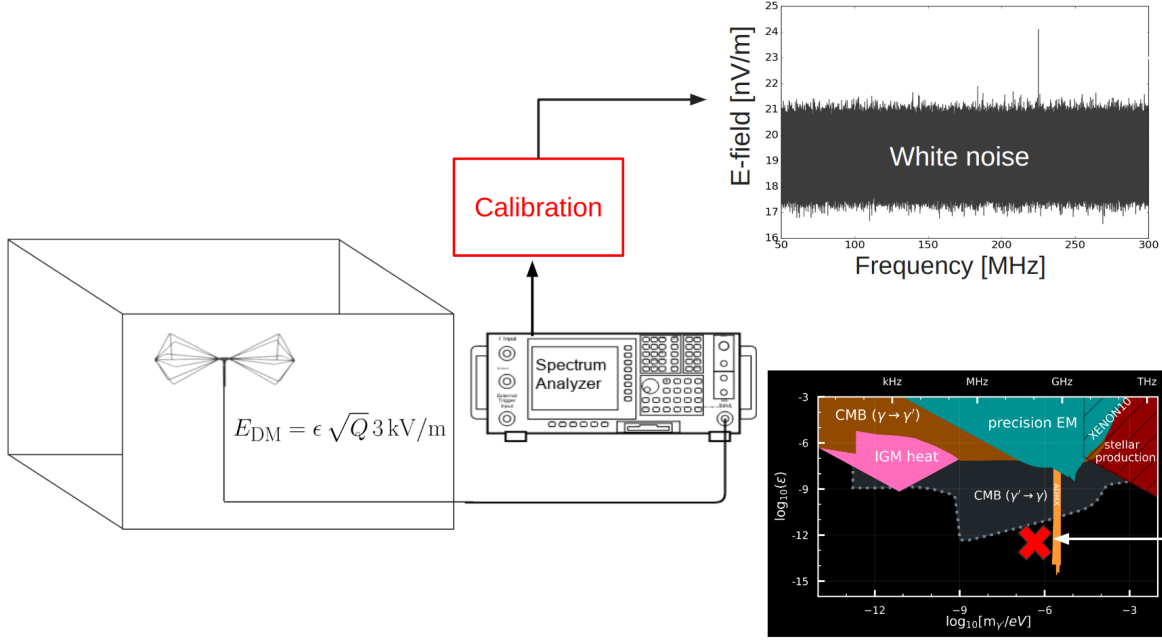


Figure 2.1: Overview of Dark E-field Radio experiment. The free space electric field strength was calculated in Sec. 1.4, and will be modified to include the Q of the cavity in Sec. 2.1.2. The design of the system is outlined in this chapter, while it's performance is measured in Ch. 3. The use of the system, its calibration, and setting a limit are all discussed in Ch. 4. **comment: Remake this. Change E_{DM} to E_{ant} , 3kV to 4.5kV, change limit plot. Image from google slide called "schematic"**

506 system performance are put off until Ch. 3).

507 A note on experiment “run numbers”. Run 1A is the 50-300 MHz run. There have been
 508 four attempts at collecting run 1A data. The final, published data run was collected between
 509 May 10 and May 19, 2023 and is called run 1.4 or run 1p4 throughout my power points and
 510 file names. I will refer to this run interchangeably as run 1A or run 1.4. Strictly speaking, it
 511 should be run 1A.4, but if I change it now it will be inconsistent with file names. When you
 512 forget about this note, you will have a hard time finding data in my file structure, especially

513 as future runs are completed.

514 2.1 Sources of Power in Measured Spectrum

515 This section will break down each term in the following equation for the input-referred power

$$P_i = \text{Thermal Noise} + \text{Dark Photon Signal} + \text{RFI} + \text{Amp Chain Noise} + \text{ADC Effects}/G, \quad (2.1)$$

516 where G is a gain factor. While convenient, this word equation is not rigorous, and relies
517 on the following subsections 2.1.1 - 2.1.5 for definition.

518 2.1.1 Thermal Noise

519 2.1.1.1 Blackbody Electric Field Density

520 This subsection estimates the noise-like¹ electric field in free space due to black body radi-
521 ation. It assumes to be in *some* enclosure in that the ambient temperature is known to be
522 300 K and not, for example, the 3.6 K of the sky.

523 Planck's law gives the black body spectral energy density as

$$u_\nu(\nu, T) d\nu = \frac{8\pi h\nu^3}{c^3} \frac{1}{e^{h\nu/kT} - 1} d\nu \quad \left[\frac{J}{m^3} \right]. \quad (2.2)$$

524 This is frequently written in terms of spectral radiance,

¹“Noise-like” simply means that the power contained in a signal is proportional to the bandwidth measured. Noise-like signals are more conveniently described as a power spectral density (PSD) which we will describe with the symbol S . As we will see, coherent signals which have finite width in frequency space $\Delta\nu_{\text{sig}}$ can share this property if the measurement bandwidth $\Delta\nu_{\text{RF}} \lesssim \Delta\nu_{\text{sig}}$, even though one wouldn't think of a coherent signal as being “noise-like”

$$B_\nu(\nu, T) d\nu = \frac{2h\nu^3}{c^2} \frac{1}{e^{h\nu/kT} - 1} d\nu d\Omega \quad \left[\frac{W}{m^2} \right]. \quad (2.3)$$

525 Integrating this isotropic radiance over a solid angle 4π sr as well as a small frequency
 526 band $\Delta\nu$ gives the flux density $|\mathbf{S}|$ (AKA, the magnitude of the Poynting vector),

$$\begin{aligned} |\mathbf{S}| &= \int_0^{4\pi} \int_\nu^{\nu+\Delta\nu} B_\nu(\nu, T) d\nu d\Omega \\ &= \int_0^{4\pi} \int_\nu^{\nu+\Delta\nu} \frac{2h\nu^3}{c^2} \frac{1}{e^{h\nu/kT} - 1} d\nu d\Omega \quad \left[\frac{W}{m^2} \right]. \\ &\approx \frac{8\pi h\nu^3}{c^2} \frac{1}{e^{h\nu/kT} - 1} \Delta\nu \end{aligned} \quad (2.4)$$

527 Poynting's theorem relates this flux density to the RMS electric field

$$|\mathbf{S}| = \frac{|E_{rms}|^2}{\eta} \quad \left[\frac{W}{m^2} \right], \quad (2.5)$$

528 where η is the impedance of free space. Equating Eqs. 2.4 and 2.5 and solving for the
 529 electric field gives

$$\frac{|E_{rms}|}{\sqrt{\Delta\nu}} = \sqrt{\eta \frac{8\pi h\nu^3}{c^2} \frac{1}{e^{h\nu/kT} - 1}} \quad \left[\frac{V}{m \cdot \sqrt{Hz}} \right], \quad (2.6)$$

530 and is plotted in Fig. 2.2.

531 Eq. 2.6 breaks up nicely into two regimes,

$$\frac{|E_{rms}|}{\sqrt{\Delta\nu}} = \begin{cases} \sqrt{\eta \frac{8\pi kT\nu^2}{c^2}} & \text{Rayleigh-Jeans regime } (h\nu \ll kT) \\ \sqrt{\eta \frac{8\pi h\nu^3}{c^2} e^{-h\nu/kT}} & \text{Wien approximation } (h\nu \gg kT) \end{cases} \quad \left[\frac{V}{m \cdot \sqrt{Hz}} \right]. \quad (2.7)$$

532 At frequencies and temperatures where the experiment is operated (< 300 MHz and
 533 300 K), $h\nu/kT \lesssim 5 \times 10^{-5}$ suggesting the Rayleigh-Jeans approximation is valid. At 300 K,

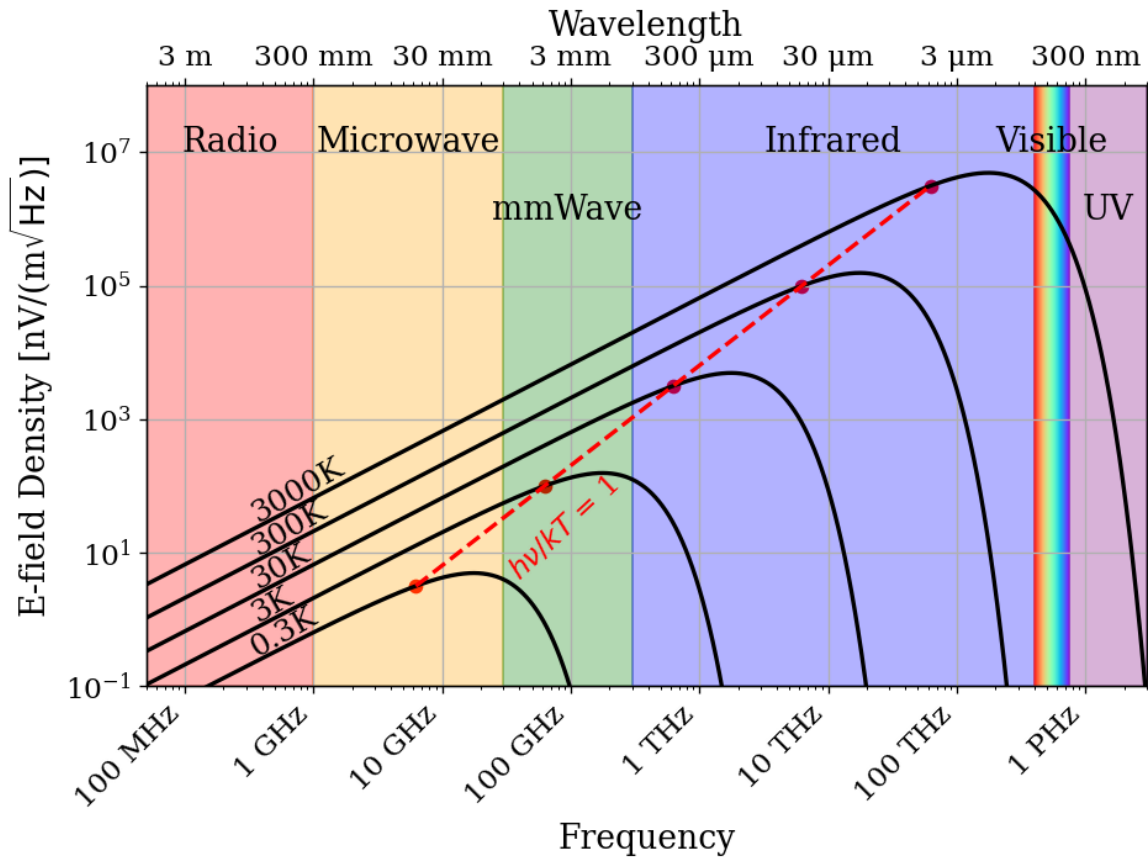


Figure 2.2: Blackbody electric field spectral density from radio to UV frequencies. A variety of temperatures are shown in black. The dashed red curve and red points indicate where along the black curves $h\nu = kT$, i.e. where Eq. 2.7 breaks up between the Rayleigh-Jeans regime to the Wien approximation. Note that these points are only a function of ν and T ; their vertical placement is chosen to lie on their respective curve but has no physical significance. The dark radio experiment is firmly in the Rayleigh-Jeans regime.

534 this yields electric field spectral densities of 1 and 6 nV/(m $\sqrt{\text{Hz}}$) at 50 and 300 MHz respec-

535 tively.

536 It is interesting to note, however, that for cryogenic experiments operating at a few GHz

537 and in the sub K range (A common technique; see for example [17–19]), $h\nu/kT \approx 1$ and

538 the full form of Eq. 2.6 must be used. This is shown at frequencies and temperatures to the

539 right of the red dashed line in Fig. 2.2.

540 **2.1.1.2 Antenna Noise**

541 An antenna's effective aperture, A_e [m^2], represents the effective area that it has to collect
542 power density or irradiance [W/m^2] from an incident Poynting vector,

$$P_A = |\mathbf{S}|A_e, \quad (2.8)$$

543 Where $|\mathbf{S}|$ is the magnitude of the incident Poynting vector and P_r is the power received at
544 the antenna which is available at its terminals.

545 A_e is a directional quantity which varies with the antenna's directivity $D(\Omega)$, where Ω
546 represents solid angle around the antenna. It varies with frequency ν , though it is generally
547 discussed in terms of wavelength λ . Three matching parameters are introduced to describe
548 how much actual power the antenna is able to deliver to a transmission line; p the polarization
549 match of the wave to the antenna, m the impedance match of the antenna to the transmission
550 line and η_a the efficiency of the antenna which represents how much power is absorbed
551 compared to that lost to Joule heating of the antenna. p , m and η_a are all real, dimensionless
552 and vary between 0 and 1.

$$A_e \equiv \frac{\lambda^2}{4\pi} D(\Omega) p m \eta_a. \quad (2.9)$$

553 This definition follows [20], though some authors do not include p in the definition [21,
554 22].

555 A simple derivation of the direction-averaged effective aperture based on thermodynamics
 556 will provide intuition. An isotropic antenna placed in a cavity at temperature T will be
 557 illuminated by randomly polarized, isotropic radiation of the form given by the Rayleigh-
 558 Jeans limit of Eq. 2.4, $|\mathbf{S}| = 8\pi kT\Delta\nu\nu^2/c^2$. The power received by the antenna can be found
 559 by Eq. 2.8,

$$\begin{aligned}
 P_A &= \langle A_e \rangle \frac{1}{2} |\mathbf{S}| \\
 &= \langle A_e \rangle \frac{4\pi kT\nu^2}{c^2} \Delta\nu,
 \end{aligned} \tag{2.10}$$

560 Where the factor of 1/2 is introduced to account for the random polarization and the $\langle \rangle$
 561 indicate an average aperture over all angles around the antenna. If a resistor is placed in
 562 a second cavity, also at temperature T, it will deliver its Johnson-Nyquist noise power [23,
 563 24]

$$P_R = kT\Delta\nu \tag{2.11}$$

564 into a matched transmission line. This is shown in Fig. 2.3. The second law of thermo-
 565 dynamics makes a very powerful statement here; the net power flow between antenna and
 566 terminator must equal 0 if the two temperatures are indeed equivalent. This means $P_R = P_A$
 567 or Eq. 2.10 = Eq. 2.12,

$$\langle A_e \rangle \frac{4\pi kT\nu^2}{c^2} \Delta\nu = kT\Delta\nu \tag{2.12}$$

568 or,

$$\begin{aligned} \langle A_e \rangle &= \frac{c^2}{4\pi\nu^2} \quad [\text{m}^2] \\ &= \frac{\lambda^2}{4\pi} \end{aligned} \quad (2.13)$$

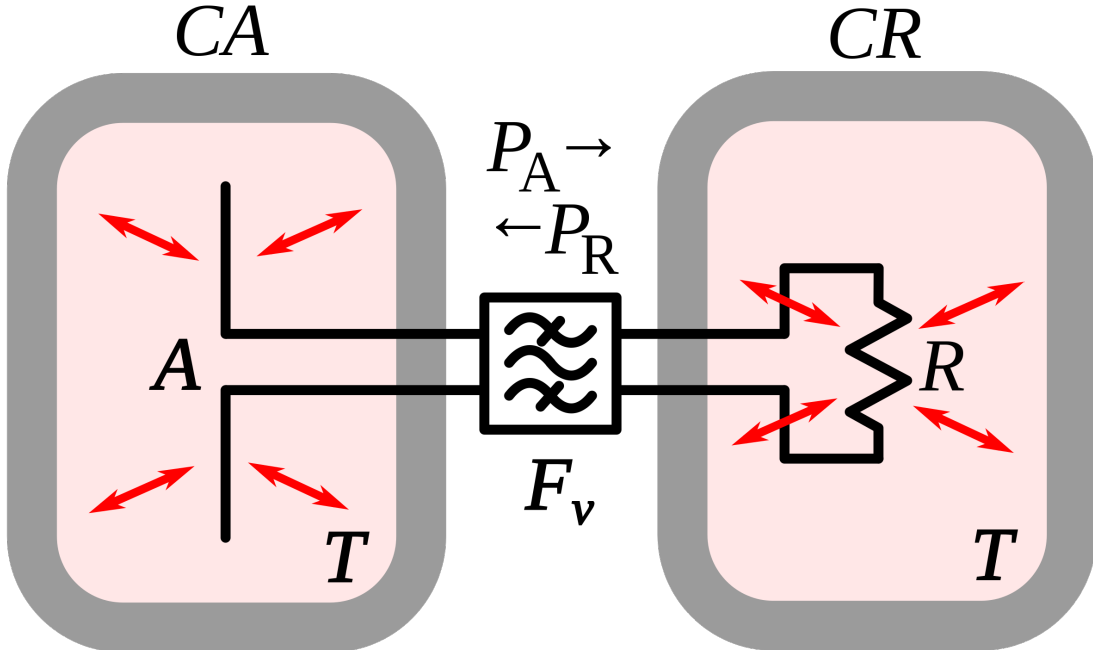


Figure 2.3: An antenna and matched resistor in cavities which are in thermal equilibrium. They are connected by a narrow filter permitting a narrow frequency band $\Delta\nu$. Image from Wikipedia, and is similar to the thought experiment proposed by Dicke [25].

569 This allows us to conclude that the power spectral density S_{ant} received by an antenna
 570 surrounded by an isotropic temperature is simply $kT\Delta\nu$ in the Rayleigh-Jeans limit of room
 571 temperatures and standard electronic frequencies. This result is independant of frequency,
 572 which can be understood by the reciprocal frequency dependence of the blackbody radiation
 573 (Eq. 2.4) and the average effective aperature (Eq. 2.13). The result is an antenna power
 574 which is equivalent to the well known result for a resistor at 290 K,

$$S_{\text{ant}} = 3.9 \times 10^{-22} [\text{W}/\text{Hz}] = -174 [\text{dBm}/\text{Hz}]. \quad (2.14)$$

575 Note that S_{ant} indicates power spectral density and should not be confused with \mathbf{S} which
 576 indicates a Poynting vector.

577 **2.1.1.3 Dicke radiometer equation**

578 Equation 2.14 gave the mean of a power spectrum which is inherently noisy. We will now
 579 show the origin of this spectrum.

580 An enclosure who's electrically-lossy walls contain free charge carriers at finite temper-
 581 ature will radiate incoherently by the fluctuation dissipation theorem. This theorem is
 582 the underlying principal of phenomena such as Brownian motion [26] and Johnson-Nyquist
 583 noise [23, 24], but was not generally proven until 1951 by Callen and Wellton [27]. The
 584 random thermal fluctuation of the charge carriers will radiate a black-body spectrum. Ob-
 585 serving the electric field in the time domain, one can imagine the radiation arriving at a
 586 detector at a wide variety of random frequencies and phases. This is incoherent noise in that
 587 at each time domain sample is independent of the one proceeding it ². The detector will
 588 produce a voltage which can be modeled as Gaussian with zero mean and standard deviation
 589 $\sigma = \sqrt{S_{\text{ant}} \Delta \nu_{\text{RF}} |Z|}$ where Z is the system impedance (here 50Ω). This is shown for a room
 590 temperature antenna (or equivalently a room temperature resistor, see Fig. 2.3) in Fig. 2.4.

²The hidden assumption here is that blackbody radiation is totally incoherent. It actually has a coherence time $\tau_c \approx 2 \times 10^{-14} \text{ s}$ at 300 K [28]. For this statement to hold, the sample time $\tau_s \gg \tau_c$. For run 1A, $\tau_s = 1/800 \text{ MHz} = 1.25^{-9} \text{ s}$, 5 orders of magnitude more than τ_c

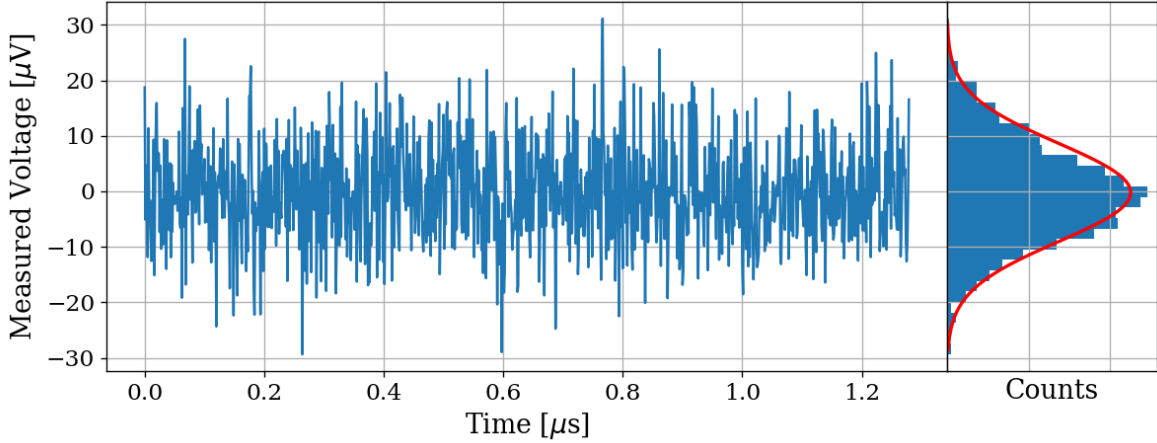


Figure 2.4: Simulated antenna noise voltage at room temperature in the time domain. Sample rate $\nu_s = 800\text{MHz}$ and number of samples $N = 2^{10} = 1024$. Bin width $\Delta\nu_{\text{RF}} = \nu_s/N \approx 800\text{ kHz}$. Data are binned and plotted as a histogram to the right. Best fit Gaussian is shown on the histogram in red with $\mu = -0.199\text{ }\mu\text{V}$ and $\sigma = 8.86\text{ }\mu\text{V}$. Counts have been normalized such that the bins add up to unity.

591 The next step in converting this time domain voltage signal to a frequency domain
 592 power spectral density (PSD). The first step is taking a discrete Fourier transform. This is
 593 usually implemented with an algorithm known as a fast Fourier transform (FFT), so that
 594 $\tilde{V} = \text{FFT}(V)$. In order to convert to a power spectrum, a non-trivial normalization prefactor
 595 must be included;

$$S = \frac{2}{N^2 |Z|} |\Re(\tilde{V})[:N//2]|^2, \quad (2.15)$$

596 where N is the number of samples, Z is the system impedance, and [:N//2] is python notation
 597 for the second half of the samples contained in the \tilde{V} array. Performing this operation on
 598 the data in Fig. 2.4 yealds the data in Fig. 2.5

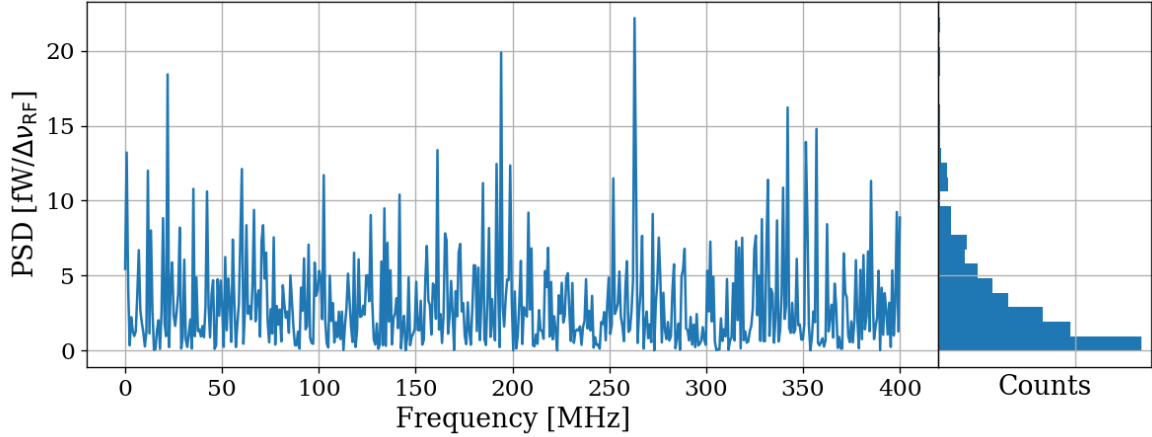


Figure 2.5: Simulated antenna noise power spectral density (PSD) at room temperature in the frequency domain. Sample rate $\nu_s = 800\text{MHz}$ and number of samples $N = 2^{10} = 1024$. Bin width $\Delta\nu_{\text{RF}} = \nu_s/N \approx 800\text{ kHz}$. Data are binned and plotted as a histogram to the right. Counts have been normalized such that the bins add up to unity.

599 The peculiar PDF of the histogram shown in Fig. 2.5 is known as a χ^2 distribution with
 600 1 degree of freedom and comes about because power is a positive-definite quantity and the
 601 standard deviation of the PSD is greater than it's mean.

602 However, by averaging many of the these power spectra together the central limit theorem
 603 dictates that we can expect the resulting PDF to be Gaussian. The transition from χ^2 to
 604 Gaussian distributed spectra is shown in Fig. 2.6.

605 Finally, this averaged power spectrum can be modeled with the Dicke radiometer equa-
 606 tion. The measured power (assuming only thermal noise) is given by

$$P_{\text{ant}} = kT\Delta\nu \left(1 \pm \frac{1}{\sqrt{\Delta\nu\tau}} \right) \quad [\text{W}]. \quad (2.16)$$

607 Here τ is the total acquisition time and so $\Delta\nu\tau$ is equivalent to the number of spectra

608 that are averaged together. This can be nondimensionalized and written

$$\frac{P_{\text{ant}}}{kT\Delta\nu_{\text{RF}}} = 1 \pm \frac{1}{\sqrt{N}} \quad [\text{None}], \quad (2.17)$$

609 which will become important during data analysis which is the topic of Sec. 4.2.

610 For the remainder of this thesis, unless otherwise stated, it will be assumed enough
611 spectra have been averaged together that a PSD is Gaussian and scales with the square root
612 of total acquisition time according to Eq. 2.16.

613 Thus far the analysis has focused only on thermal noise, however there are other sources
614 of noise and interfering signals which must be considered, not to mention the actual dark
615 photon signal.

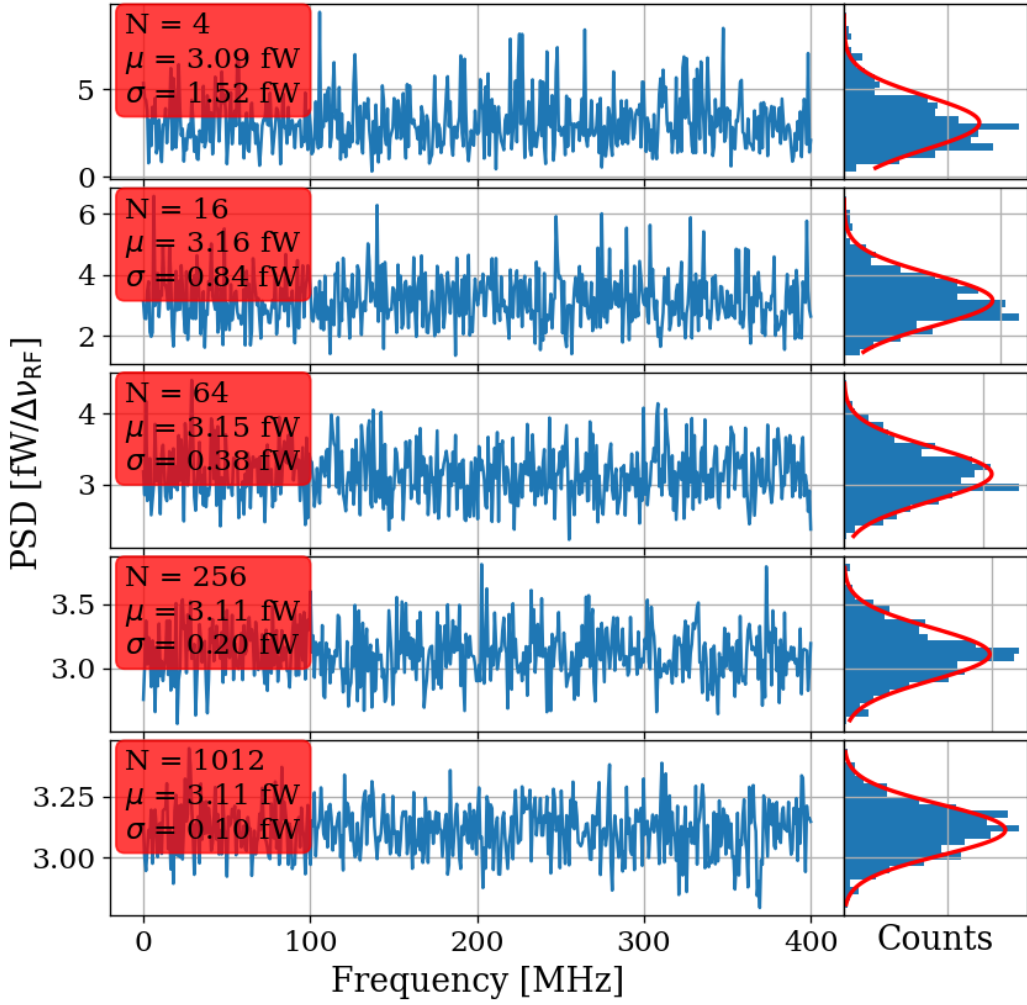


Figure 2.6: Effect of averaging on simulated antenna noise power spectral density (PSD) at room temperature in the frequency domain. Subplots show different number of averaged power spectra from $N = 4$ to 1024. Each subplot shows a factor of 4 times more averaging than the previous one. The Dicke radiometer equation predicts the standard deviation σ will scale like $N^{-1/2}$, once a large number of averages have been taken such that $\sigma \ll \mu$. Sample rate $\nu_s = 800\text{MHz}$ and number of samples $N = 2^{10} = 1024$. Bin width $\Delta\nu_{\text{RF}} = \nu_s/N \approx 800 \text{ kHz}$. Data are binned and plotted as a histogram to the right with a best fit Gaussian shown in red. Counts have been normalized such that the bins add up to unity. Note that the Y-axis scale changes between sub plots to show the improvement of the Gaussian fit. The standard deviation is indeed decreasing between plots.

616 **2.1.2 Dark Photon Signal**

617 The electric field of a kinetically mixed dark photon in free space $\mathbf{E}_{\text{ant}}^{\text{free space}}$ was shown in
 618 Eq. 1.7. In a cavity, the E-field will be enhanced by the quality factor Q of the cavity. This
 619 Q must be measured or simulated, but for this toy analysis we will assume it to be known
 620 ³. The E-field inside the cavity then is

$$\mathbf{E}_{\text{ant}} = \mathbf{E}_{\text{ant}}^{\text{free space}} \sqrt{Q}, \quad (2.18)$$

621 since Q is proportional to power, i.e. \mathbf{E}^2 . This E-field will then need to be converted from
 622 a wave in the cavity to a wave in a 50Ω transmission line by an antenna. Similar to the
 623 thermal noise of the previous section, this electric field will be converted via the effective
 624 aperture of the antenna. Similar to Q , aperture will be assumed to be known.

625 The total received power from a coherent signal inside the room then is

$$P = \frac{\mathbf{E}_{\text{ant}}^{\text{free space}^2}}{\eta} Q < A_e >, \quad (2.19)$$

626 where η is the impedance of free space.

627 The observed spread of the frequencies of the dark photon are in important effect which
 628 determine system design. In the following paragraphs of this section, several sections of
 629 Gramolin et al. [30] are summarized. Also note that the original calculation for the predicted
 630 line shape this appears to be Michael Turner in 1990 [31].

631 A simple model of the dark photon line assumes it is monochromatic, i.e. it's line shape
 632 is a delta function in frequency domain,

$$\nu_{\text{obs}} = \delta(\nu - \nu_{\text{DP}}). \quad (2.20)$$

³Typical values are in the ball park of 100. Some experiments have ultra-high Q cavities $\approx 10^{10}$ [29]

633 This is consistent with it's production add reference: misalignment mechanism/ch 1.

634 However, when observed in a frame other than its rest frame, the frequency of a (single)

635 dark photon will shift by an amount proportional to it's kinetic energy

$$\nu_{\text{obs}} = \left(1 + \frac{v_n^2}{2c^2}\right) \nu_{\text{DP}}, \quad (2.21)$$

636 where ν_{obs} is the observed frequency of the n th dark photon, v_n is its velocity, c is the speed

637 of light, and ν_{DP} is its rest frequency. The end result will be a signal that has some spread

638 in frequency, $\nu_{\text{DP}}/(\Delta\nu) \equiv Q_{\text{DP}} \approx 10^6$, with a line shape given by 2.24.

639 By summing over an infinity of dark photons of random phases and velocities (sampled

640 from the relative velocity of the dark matter halo), each with a frequency given by Eq. 2.21,

641 one can construct a power spectral density (PSD) of the dark photon signal as measured on

642 earth, S [W/Hz].

643 When performing a measurement, one records the voltage V emerging from a detector

644 for a period of time greater than the coherence of the dark photon $\tau_{\text{FFT}} \gg \tau_c$. The Fourier

645 transform of $V(t)$ is denoted $\tilde{V}(\nu)$

646 The signal will have a total power

$$P_0 = \frac{1}{\tau_{\text{FFT}}} \int_0^{\tau_{\text{FFT}}} \frac{V(t)^2}{|Z|} dt = \int_0^{1/\tau_{\text{FFT}}} S(\nu)^2 d\nu, \quad (2.22)$$

647 which is a statement of Parseval's theorem.

648 The normalized line shape is defined by dividing by P_0 ; $\lambda(\nu) \equiv S(\nu)/P_0$. This has the

649 property of being normalized to unity,

$$\int_0^\infty \lambda(\nu) d\nu = 1. \quad (2.23)$$

650 Finally, the result for this normalized line shape is

$$\lambda(\nu) = \frac{2 c^2}{\sqrt{\pi} v_0 v_{\text{lab}} \nu_{\text{DP}}} \exp \left(-\frac{\beta^2 v_0^2}{4 v_{\text{lab}}^2} - \frac{v_{\text{lab}}^2}{v_0^2} \right) \sinh \beta \quad \left[\frac{1}{\text{Hz}} \right], \quad (2.24)$$

651 where $|v_0| \approx 220$ km/s is the circular rotation speed of the Galaxy at the radius of the sun

652 (approximately 8 kpc), $v_{\text{lab}} \approx 233$ km/s is the relative velocity of the Sun to the rest frame

653 of the Galaxy and

$$\beta \equiv \frac{2 c v_{\text{lab}}}{v_0^2} \sqrt{\frac{2 (\nu - \nu_{\text{DP}})}{\nu_{\text{DP}}}}.$$

654 Equation 2.24 is used to generate Fig. 4.14. Note the quality factor $Q_{\text{DP}} \approx 10^6$ as

655 mentioned above.

656 2.1.3 Radio Frequency Interference

657 Radio Frequency Interference (RFI) includes any coherent interfering signals which can be

658 detected by the experiment. While noise is better described as a power spectral *density*

659 [W/Hz] or electric field *density* [V/(m $\sqrt{\text{Hz}}$)], RFI is made up of more narrow lines and is

660 discussed in terms of a power [W] or electric field [V/m]. In this experiment, RFI is mitigated

661 through the shielding effectiveness (SE) of the cavity. SE measurements and more details

662 about local RFI are discussed further in Sec. 2.5.1 and Sec. 3.2, and a plot of the local RFI

663 spectrum is shown in Fig. 3.15.

664 The peak RFI spike is at 186 MHz and approximately 100 $\mu\text{V}/\text{m}$, an energy density

665 of roughly 10^{-11} W/m². This will be reduced by the SE of the room (roughly 120 dB at

666 200MHz, see Fig. 3.12), but just like a coherent dark photon, it will be enhanced by the

667 Q/effective aperture. This will be right on the edge of detection, but in the actual data run
 668 it was not detected.

669 **2.1.4 Amplifier Chain Noise⁴**

670 Any amplifier will have some noise which it adds to an incoming signal which will degrade
 671 the signal to noise ratio (SNR) of the measurement ⁵. A low noise amplifier (LNA) is an
 672 amplifier which has been specifically designed to minimize the noise contribution. This
 673 process is shown schematically in Fig. 2.7.

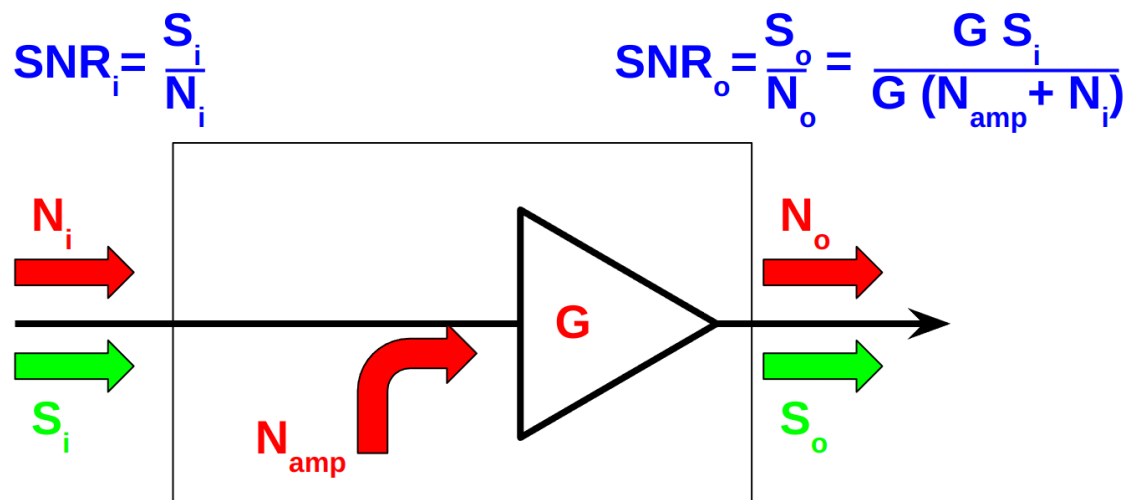


Figure 2.7: Schematic of LNA (with power gain G) adding input referred noise N_{amp} . Since N_{amp} is referred to the input, it can be directly added to the input noise which is itself input-referred. The ideal, noisless, amplifier is represented by the triangle, while the physical amplifier including noise is contained in the rectangle.

⁴Code for this section can be found at: <https://github.com/josephmlev/darkRadio/tree/master/thesis/ch2/CH2.ipynb>

⁵A great lecture on the subject by Prof. Greg Durgin can be found at [32]

674 The performance of an LNA is generally evaluated by its noise factor (F). F is defined
 675 to be the ratio the SNR at the input of an LNA to that at its output.

$$\begin{aligned}
 F &\equiv \frac{\text{SNR}_i}{\text{SNR}_o} \\
 &= \frac{S/N}{[S G]/[(N + N_{\text{amp}})G]} \\
 &= \frac{1}{1/[1 + N_{\text{amp}}/N]} \\
 &= 1 + \frac{N_{\text{amp}}}{N},
 \end{aligned} \tag{2.25}$$

676 where S and N are the signal and noise [W] presented to the LNA respectively, N_{amp} is
 677 the input-referred noise added by the LNA and G is the power gain. By factoring out the
 678 implicit $k \Delta\nu$ from $N = kT\Delta\nu$, we find

$$F = 1 + \frac{T_e}{T_0}, \tag{2.26}$$

679 where T_e is the noise temperature of a device and T_0 the temperature of the system being
 680 measured by the LNA.

681 Note that following the same derivation as Eq. 2.25, it is simple to show that the noise
 682 figure of an attenuator at temperature T with loss L is given by

$$F_{\text{att}} = 1 + \frac{(L - 1)T}{T_0}, \tag{2.27}$$

683 where T_0 is the reference temperature defined above. If $T = T_0$, Eq. 2.27 simplifies to
 684 $F_{\text{att}} = L$

685 In order to standardize device specifications for across system applications, it is common
 686 to choose a reference temperature T_0 of 290K. If not specified, it is generally safe to assume
 687 this has been done.

688 Noise factor is simply defined from noise figure,

$$\text{NF} \equiv 10\log_{10}(F). \quad (2.28)$$

689 When working with LNAs, all three measurements (T_e , F and NF) are frequently used
 690 and one must use Eqs. 2.26 and 2.28 to convert between them.

691 One important generalization is that of a cascaded series of amplifiers, shown schemati-
 692 cally in Fig. 2.8.

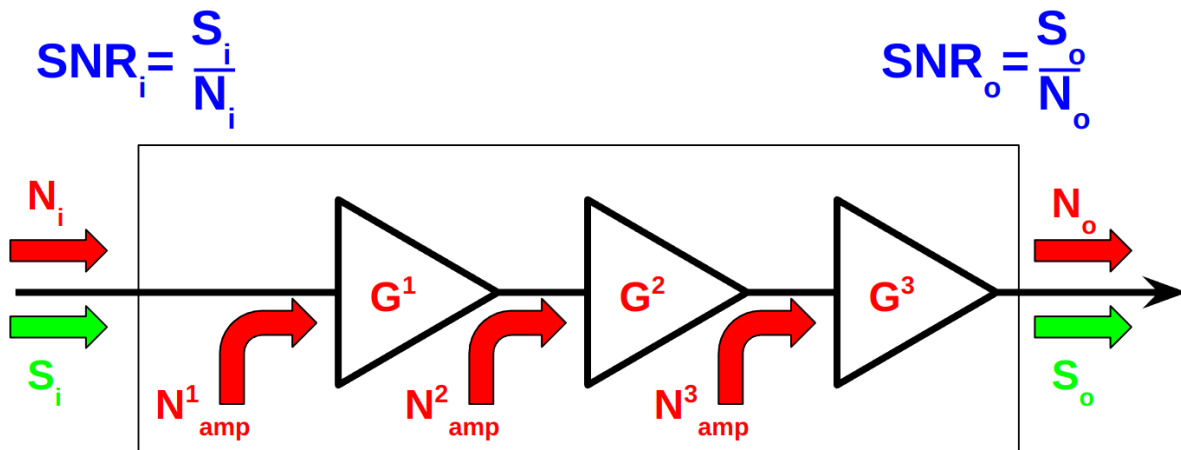


Figure 2.8: Schematic of cascade of $n = 3$ amplifiers and their added noise N_{amp}^n . Each amplifier has a gain of G^n . The SNR at the output is derived in Eq. 2.29. Note that superscripts in the figure and caption refer to index of each component and are not exponents.

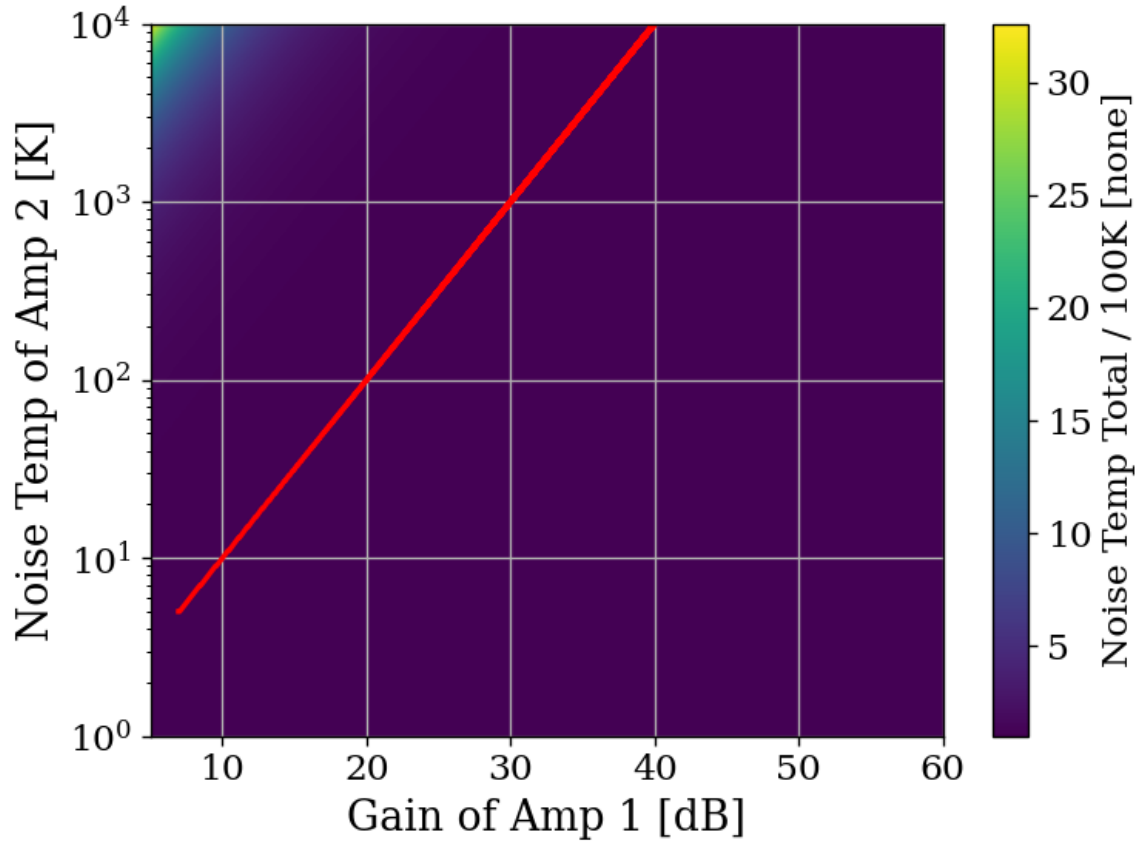


Figure 2.9: Cascaded noise temperature for system with $n = 2$ amplifiers, normalized to noise temperature of amplifier 1 (the so called LNA) = 100 K. Shown schematically (for $n = 3$) in Fig. 2.8. First amplifier's noise temperature and gain (40 dB and 100 K respectively) roughly equivalent to the LNA used in phase 1A of the experiment[33]. Red curve shows where the system's noise temperature is 1% higher than LNA noise temperature. This shows that for a 40 dB, 100 K LNA, in order to change the system noise temperature by 1 K, a second stage amplifier with a noise temperature of 10^4 would be required. Secondary amplifiers with noise temperatures closer to 500 K are realistic and inexpensive. Note that red curve should continue, but is cut off as a plotting artifact.

693 Here the total noise figure of n amplifiers can be shown to be

$$F_{\text{total}} = F_1 + \frac{F_2 - 1}{G_1} + \frac{F_3 - 1}{G_1 G_2} + \cdots + \frac{F_n - 1}{G_1 G_2 \cdots G_{n-1}}, \quad (2.29)$$

694 following the same derivation as Eq. 2.25. Since the noise temperature of a system depends

695 on the noise temperature a given amplifier divided by he gain which precedes it, a front-end
696 LNA with modest gain ensures the total noise figure of the the system is equal to it's noise
697 figure to very good approximation. This is shown in Fig. 2.9. We will use this approximation
698 and assert

$$\text{Amp Chain Noise} = \text{LNA Noise}, \quad (2.30)$$

699 Where LNA here is taken to mean the first gain stage in the amplifier chain
700 Noise figures are typically frequency dependant, though they vary slowly over frequency
701 and can be approximated as constant over narrow frequency bands. Noise figures are typically
702 given on the data sheet of the LNA [33], but can also be measured. Measurement of LNA
703 noise is covered in Sec. 3.1.1 and is shown in Fig. 3.5 (which is in good agreement with the
704 LNA's data sheet [33]).

705 The power contributed by the LNA's noise is simply given by

$$P_{\text{LNA}} = kT_e\Delta\nu \quad (2.31)$$

706 This is again the mean of a fluctuating power, just as 2.16.

707 2.1.5 ADC effects

708 “ADC effects” is a catch all term which refers to power introduced by an analog-to-digital
709 converter. It contains are a three components, listed in order of importance;

$$\text{ADC Effects} = \text{Spurious Signals} + \text{ADC Noise Floor} \quad (2.32)$$

710 Equation 2.29 shows that gain G introduced before a noisy element in the RF chain, will
711 reduce the relative contribution of that noise by a factor of G . The same idea applies to
712 ADC effects, though one must be careful with the language used to describe this; spurious
713 signals are not noise, and the experiment's output *is* mostly noise.

714 **2.1.5.1 Spurious signals**

715 Spurious signals (also known as spurs) are coherent signals which are introduced into the
716 signal path at the ADC⁶. They are likely caused by candidates caused by RFI due to various
717 clocks in the PC in close proximity to the ADC. The coherence of spurs means they will pop
718 up above the noise with more averaging. Spurs don't degrade the SNR of the experiment in
719 the same way a noisy amplifier chain would; instead, they produce false positive candidates
720 which must be excluded, similar to RFI discussed in Sec. 2.1.3. Similar to ADC noise,
721 they can be measured easily by terminating the input of the ADC and scanning. They are
722 investigated in Sec. 3.3.2 and shown in Fig. 3.16, where they are shown to be nearly negligible,
723 having been mitigated by the gain of the system. There is a single spur detected after a few
724 days (see Sec. 4.2.5), but for this simple analysis we will assume spurs are negligible.

725 **2.1.5.2 ADC noise**

726 ADC noise can simply be measured by terminating the input and taking a scan. This is is
727 the same procedure as with spurs, and can be seen in Fig. 3.16. The result is that ADC

⁶Note that these spurs described here are not the same as the spurs that are described by the ADC specification *spur free dynamic range* (SFDR). SFDR is measured in dBc, i.e. *relative* to a carrier. Since our "carrier" is broadband noise, each bin produces some spurs which are -66 dBc [34] relative to itself. The aggregate of these spurs are also broadband, and averages down with the experiment's noise. The SFDR spurs are negligible for an experiment which looks at a noise-like background.

728 noise is $\approx -130\text{dBm}/47.7\text{Hz}$; a factor of 10^5 lower than the thermal noise of the experiment
 729 $\approx -81\text{dBm}/47.7\text{Hz}$, both output-referred⁷, which agrees with the ADC's data sheet [34].
 730 Since ADC noise follows the same scaling as the experiment's thermal noise (Eq. 2.16), this
 731 factor of 10^5 is independent of averaging, and ADC noise is totally negligible.

732 2.2 Toy Analysis⁸

733 With each of the terms of Eq. 2.1 defined in the previous section, we will now perform and
 734 view several simulations of a simplified dark photon signal on a simplified background. This
 735 section should provide intuition about the process of detecting a weak, narrow signal on a
 736 background PSD of thermal noise. It is assumed the noise has been averaged a sufficient
 737 number of times such that it's PDF is Gaussian (discussed in Sec. 2.1.1.3). Furthermore,
 738 following the discussion of Sec. 2.1, Eq. 2.1 can be simplified by setting RFI and ADC
 739 Effects to zero and combining Thermal Noise (300 K) with Amp Chain Noise (100 K) into a
 740 single term which represents the total of the noise in the whole system, $S_{\text{sys}} = P_{\text{sys}}/\Delta\nu_{\text{RF}} =$
 741 $k(T_{\text{ant}} + T_{\text{LNA}})$. With these simplifications, the input-referred measured power of Eq. 2.1
 742 reduces to

$$P_i = P_{\text{DP}} + kT_{\text{sys}}\Delta\nu_{\text{RF}} \left[1 \pm \frac{1}{\sqrt{N}} \right], \quad (2.33)$$

743 where $T_{\text{sys}} \equiv 400$ K, realistic for the experiment that is being simulated. Also note that this
 744 equation assumes the dark photon's line shape is much more narrow than $\Delta\nu_{\text{RF}}$ such that the

⁷Technically it doesn't matter where they are referred since they are taken in ratio. As long as they are referred to the same point!

⁸Code for this section can be found at: <https://github.com/josephmlev/darkRadio/tree/master/thesis/ch2/toyAnalysis.ipynb>

745 measured input-referred dark photon power is independent of $\Delta\nu_{\text{RF}}$. In the simulations the
746 line shape will be modeled as a delta function as in Eq. 2.20. The signal will be introduced
747 simply by adding some power in a single bin to a Gaussian background in frequency domain.
748 Performing an FFT on a perfect (discretized) sine wave can cause it's power to be split among
749 adjacent bins depending on the ratio of the sample rate to the sine wave's frequency. This
750 can be minimized by windowing the time-domain data as is discussed in Ch. 2 Sec. 2
751 of Ben Godfrey's thesis [35]. This effect is avoided by working in the frequency domain and
752 adding power to a single bin which is the method used here. A reminder that throughout
753 this thesis, code is available at github and is linked in the footnote of each section title.

754 With a simple simulation framework in place, we can now begin to generate signal-
755 containing-spectra. Figure 2.10 qualitatively shows the 400 K system noise (input-referred
756 antenna plus LNA) averaging down, leaving a small signal visible. Further subsections in
757 this section will quantify this.

758 With a basic conceptual framework in place, it is now simpler to quantify signal detection
759 and the uncertainty on how many averages are required to detect a signal, and have that
760 detection be significant in that it isn't a random fluctuation (false positive).

761 **2.2.1 Signal significance**

762 The problem of the extraction of signal from noise is fundamentally a statistical one since
763 in general both the signal and noise are random variables. A method for computing a
764 *significance threshold* (ST) must be established, such that any bin containing more power

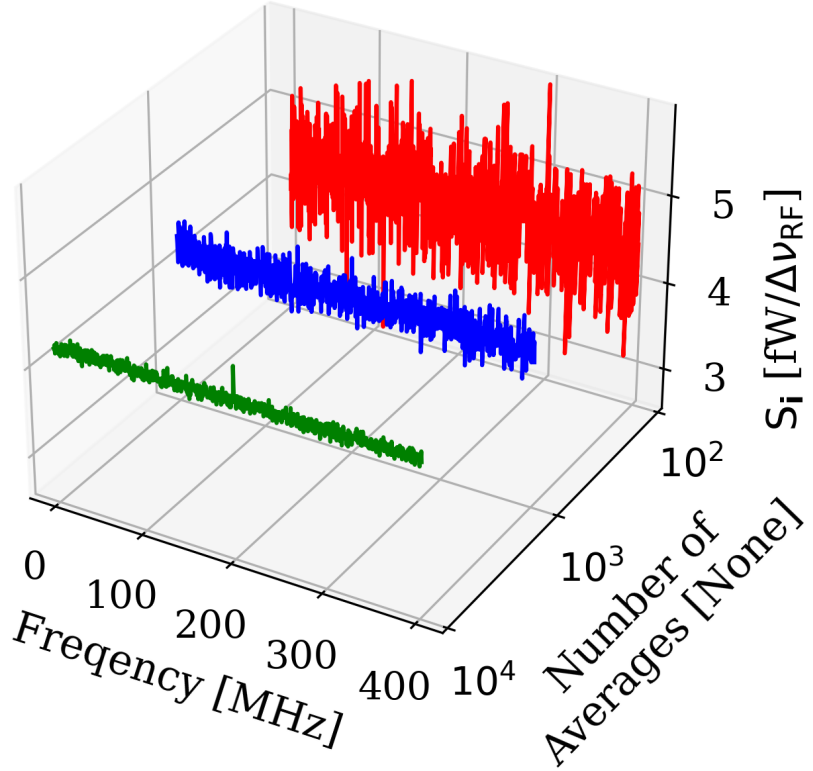


Figure 2.10: Input-referred power spectral density from simplified simulation illustrating noise averaging down to reveal a persistent, software-injected, dark photon proxy signal. The red, blue and green spectra represent 100, 1,000 and 10,000 averages respectively. The power of the signal P_{DP} is set to 0.4 fW and it only occupies a single bin. The mean of the noise is $\approx 4.3 \text{ fW}/\Delta\nu_{RF}$ where $\Delta\nu_{RF} \approx 0.78 \text{ MHz}$. The standard deviation ranges between $0.41 \text{ fW}/\Delta\nu_{RF}$ and $0.041 \text{ fW}/\Delta\nu_{RF}$ for 100 and 10,000 averages respectively. Note that this factor of 10 reduction in noise is predicted by the Dicke radiometer equation Eq. 2.16 for a factor of 100 times more averaging, as is shown in the red and green curves. Noise represents a 300 K antenna into a 100 K LNA for a total system temperature of 400 K. Signal is in a single bin at 200 MHz with a delta function line shape, defined in Eq. 2.20.

765 than this threshold is X % significant. In this way, it is possible have some known confidence

766 a given signal was not just a random fluctuation.

767 The probability that all N bins are less than z standard deviations $z\sigma$ for a standard

768 Gaussian distribution is given by

$$P(\max < z\sigma) = \left\{ \frac{1}{2} [1 + \operatorname{erf}(z/\sqrt{2})] \right\}^N, \quad (2.34)$$

769 where P is the probability, $\operatorname{erf}(z)$ is the standard error function and z is real. Setting
770 this equal to $100\% - X$ (where X is the *significance* or the desired probability a fluctua-
771 tion crosses the $z\sigma$ threshold assuming no signal), and inverting $\operatorname{erf}(z)$ yields a significance
772 threshold (ST). A convenient significance which was used in [36] is $X = 5\%$ corresponding to
773 a 5% probability that an observed fluctuation above this ST is due to chance rather than a
774 significant effect (i.e. a signal). A 5% ST for $2^{10}/2 = 512$ frequency bins⁹ works out to 3.9σ .

775 It should be noted that it is common in physics to discuss “ 5σ significance”. This means
776 that a given experiment has a $1 - \operatorname{erf}(5/\sqrt{2})$ probability (about 1 in 3×10^6) of a false positive.

777 The analysis of these normal spectra involves testing many independent frequency bins to see
778 if any one of them exceeds some threshold. It is helpful to view these bins as “independent
779 experiments”, each involving a random draw from the same parent Gaussian distribution.

780 In this context, we discuss global significance (all of the bins) in contrast to local significance
781 (a single bin). Setting a global 5% significance threshold is equivalent to setting a local
782 threshold of 3.9σ given 512 bins.

783 One concept which can assist in choosing the significance is known as the *cost* of a
784 decision. If an experiment requires a facility which charges by the hour and where the
785 schedule is set years in advance, a false positive is quite expensive since it will lead to

⁹Note that a real FFT produces half the number of frequency bins as an output compared to the time domain sample it received, hence the factor of 2 established in Fig. 2.4

786 publicity and ultimately humiliation. A follow up experiment will have to take out more
787 expensive time to verify the results, and until that happens theorists will spend their time
788 rewriting physics to explain the result of a random fluctuation. In this case, the global
789 significance should be quite low to avoid these high cost outcomes, hence the 5σ discussed
790 in the previous paragraph.

791 In the case of the dark radio experiment, a false positive is quite inexpensive. If a signal
792 is detected, just repeat the experiment. For run 1A, this is 9 days of averaging which is
793 mostly passive and is little more than an annoyance. If a signal is detected at the same
794 frequency, things become interesting. This concept of cost is discussed formally in Appendix
795 1 of Extraction of Signals From Noise by Wainstein and Zubakov [37].

796 For this reason, a significance of 5 % (i.e. 5 % chance of a false positive) is acceptable
797 for this experiment, where it is certainly not acceptable at the LHC.

798 **2.2.1.1 Computing an exclusion limit**

799 comment: 9/21/24: I'm not happy with this and the following subsection and still likely
800 have to add a few things to it.

801 With the significance threshold (ST) defined in for a spectra containing a signal in the
802 previous subsection, we turn briefly to the concept of an exclusion limit. In the actual
803 experiment, no signals were detected. In this case, the null result must be translated into
804 an exclusion limit, as in Fig. 4.21. While this section on toy analysis looks at small signals
805 riding on noise spectra, it can be easy to loose site of the fact that no signal was observed.

806 It is tempting to draw a line above the spectrum, claim no signals were observed above

807 it, and cite that as the exclusion limit. This is the red dashed line in Fig. 2.11. However,
 808 this line is riding on the thermal background, and is actually significantly higher than the
 809 true exclusion limit which is shown in dashed green. The mean μ must be subtracted off
 810 of this upper (red) line to compute the exclusion limit. In Fig. 2.12, the exclusion limit is
 811 pushed down with additional averaging, resulting in a detection of a small signal shown as
 812 an orange dot. The exclusion limit from the actual run 1A data run is shown in Fig. 4.8.

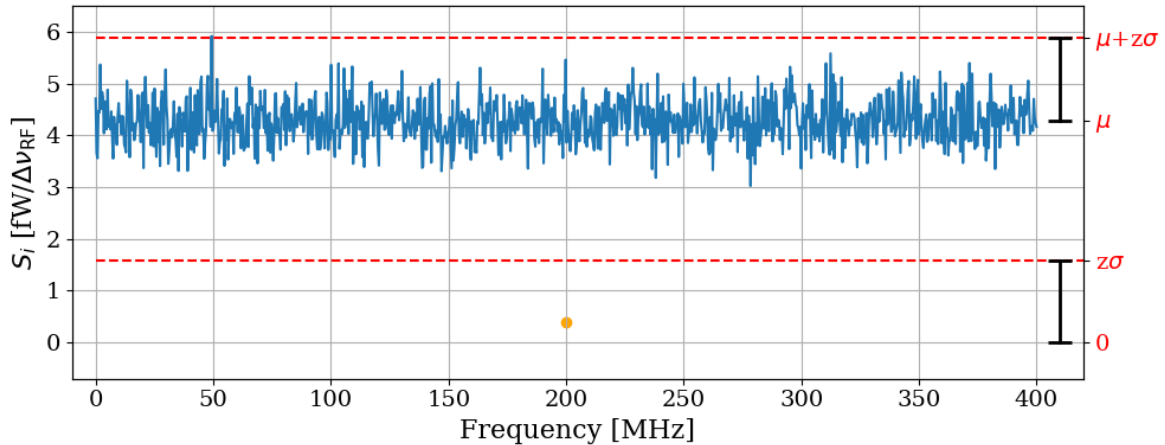


Figure 2.11: Simulated, input-referred noise spectrum containing small signal at 200MHz. The signal power = 0.4 fW, system temperature = 400 K and $N_{avg} = 100$; the same as is shown in the red spectrum of Fig. 2.10. The 0.4 fW signal is shown as an orange point. This power is added to the random background, so the measured power in the bin at 200 MHz is a Gaussian random variable given by Eq. 2.33; the mean is shifted up by the power contained in the signal. The dashed red line shows $\mu + z\sigma$, where z was derived in section 2.2.1. The detection threshold (dashed green line) is the red line minus the mean, $(\mu + z\sigma) - \mu = z\sigma$. This shows that the detection threshold is set by fluctuations of the measured power spectrum, and not its mean. Note the detection at approximately 50 MHz; this a random fluctuation and is expected to occur in 5 out of 100 simulations of these spectra since the significance used to calculate the ST was set at 5%. **comment: make detection thresh 'lime'**

813 With the derivation of the significance threshold complete, the next subsection will focus

814 on predicting the amount of time.

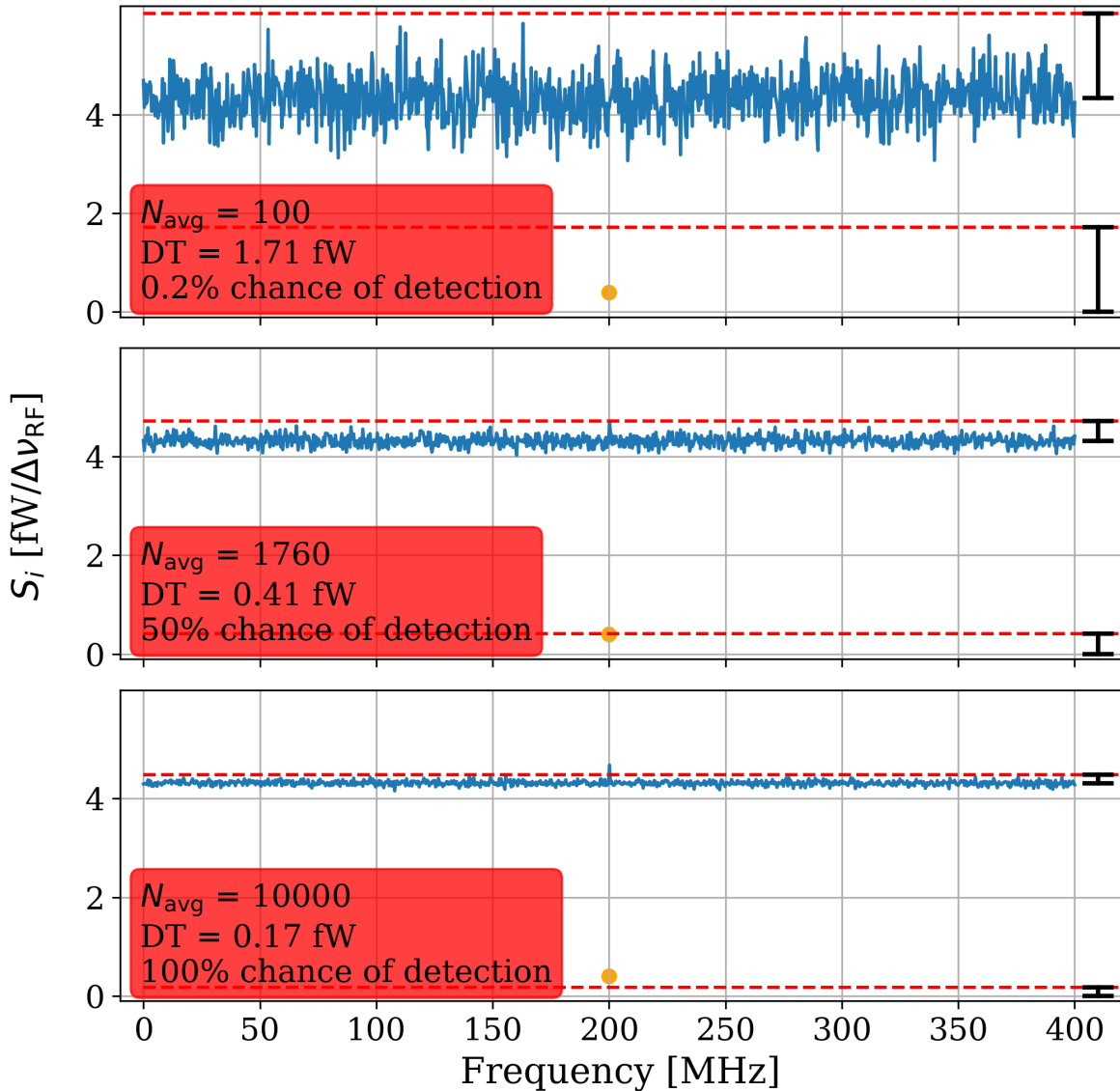


Figure 2.12: Simulated, input-referred noise spectrum containing small signal at 200MHz. The signal power = 0.4 fW, system temperature = 400 K and $N_{\text{avg}} = 100, 1,760$ and 10,000; the first and last are shown as the red and green spectra respectively in Fig. 2.10. The 0.4 fW signal is shown as an orange point. the chance of detection is computed via a simple Montie Carlo where 100,000 similar spectra containing noise and signal are generated, and the number of times the measured power at 200 MHz is greater than the red line is counted. The full set of statistics from this Montie Carlo is shown in Table 2.1. **comment: make detection thresh 'lime'**

815 **2.2.2 Predicted time to detection**

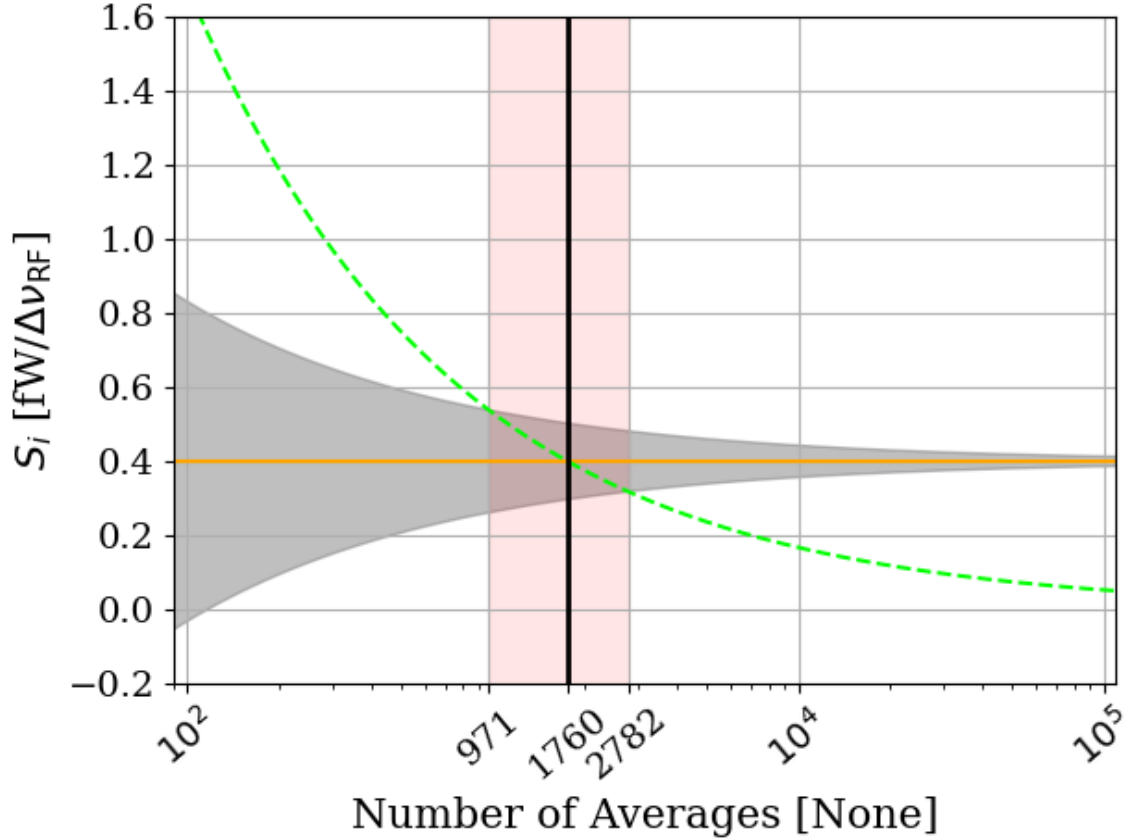


Figure 2.13: Predicted time to detection for the toy analysis spectra shown throughout this section. This is a companion to Fig. 2.12 and shows all numbers of averages between the three subplots shown in that figure, though only at a single frequency bin. Orange line represents the known, injected signal, shown as orange points in Fig. 2.12. Gray shaded region shows the standard deviation of the noise σ , which is equivalent to the uncertainty on the measured power. It is given by Eq. 2.16, and scales with the square root of time. Dashed green curve is the exclusion limit defined in Sec. 2.2.1.1. It is also shown as a dashed green line in Fig. 2.12. Finally, red shaded region shows intersection of exclusion limit (dashed green) with measurement uncertainty (shaded gray) which gives the $\pm 1\sigma$ uncertainty on the number of averages required to detect the signal. The detection statistics from a simple Monte Carlo simulation at a few points from this plot are shown in Tab. 2.1. This figure is a recreation of Fig. 3 in [4].

Number of Averages	True Pos. [%]	False Neg. [%]	False Pos. [%]	True Neg. [%]
100	0.2	99.8	5.7	94.3
971	16.3	83.7	5.5	94.5
1,760	49.8	50.2	5.7	94.3
2,782	83.8	16.2	5.7	94.3
10,000	100.0	0.0	5.6	94.4

Table 2.1: Statistics of simple Monte Carlo simulation for probability of signal detection in the toy analysis. Number of averages chosen based on Fig. 2.13. 100 and 10,000 averages show extreme cases, 1760 is a 50% chance of detection, and the two remaining values show the $\pm 1\sigma$ uncertainty band (shaded red region in Fig. 2.13).

816 2.3 Thermal Noise in A Cavity: Thermal WigglesTM

817 This section is concerned with the topic of thermal noise in a cavity, a fundamental situation
 818 for the Dark E-Field Radio Experiment. Historically, this was a challenging concept since
 819 the theory predicts the experiment should report a flat noise spectrum and it doesn't. The
 820 theory outline in Sec. 2.1.1.2 will be expanded upon, the data which seems not to conform to
 821 this theory will be presented, and finally the reasons for this disagreement will be presented.

822 2.3.1 Theory of thermal radiation in a cavity

823 In his 1946 paper The Measurement of Thermal Radiation at Microwave Frequencies [25],
 824 Robert Dickie presents a thought experiment to derive the aperture of a matched antenna
 825 from thermodynamic arguments. This was previously discussed in Sec. 2.1.1.2.

826 To recap the argument; if an antenna (in a black cavity) and load are matched to a
 827 transmission line and in thermal equilibrium (the situation presented in Fig. 2.3), the net
 828 power flow in the line must be zero by the second law of thermodynamics. If there was a

829 power flow, one of the environments would warm up, resulting in spontaneous pumping of
830 heat. An interesting way to model this situation is by treating the antenna as an aperture
831 into the cavity, as pointed out in [38].

832 The logic of this is clearly flushed out by Reif in Fundamentals of Statistical and Thermal
833 Physics [39] through four examples which deal with the radiation field $f_\alpha(\kappa, r)$ (wave number
834 κ at position r with polarization α) within cavities connected by an aperture (see Fig. 2.14)

835 **1. Independence of Position:** The radiation field inside an enclosure is homogeneous,
836 meaning $f_\alpha(\kappa, r) = f_\alpha(\kappa)$, independent of position r . If the radiation field depended on
837 position, two identical bodies at temperature T placed at different points in the enclo-
838 sure would absorb different amounts of radiation, leading to a temperature difference,
839 which would violate the equilibrium condition.

840 **2. Independence of Direction:** The radiation field is isotropic, meaning it depends
841 only on $|\kappa|$ and not the direction of $\vec{\kappa}$. If $f_\alpha(\kappa)$ depended on the direction of $\vec{\kappa}$, then
842 bodies placed in the enclosure would absorb different amounts of energy based on
843 orientation. This would contradict thermal equilibrium.

844 **3. Independence of Polarization:** The radiation field is unpolarized, meaning $f(\kappa)$ is
845 independent of the polarization index α . If it depended on polarization, bodies sur-
846 rounded by polarization filters transmitting different directions would absorb different
847 amounts of radiation, leading to temperature differences, which would again violate
848 equilibrium.

849 **4. Independence of Enclosure Shape and Contents:** The function $f(\kappa)$ is inde-
 850 pendent of the shape, volume, and material of the enclosure, as well as the bodies
 851 contained within. The argument is that if $f_\alpha^{(1)}(\kappa)$ and $f_\alpha^{(2)}(\kappa)$ were different for two
 852 enclosures at the same temperature T , then connecting them would result in unequal
 853 radiation transfer, leading to a violation of equilibrium. Therefore, $f(\kappa)$ must be the
 854 same across different enclosures.

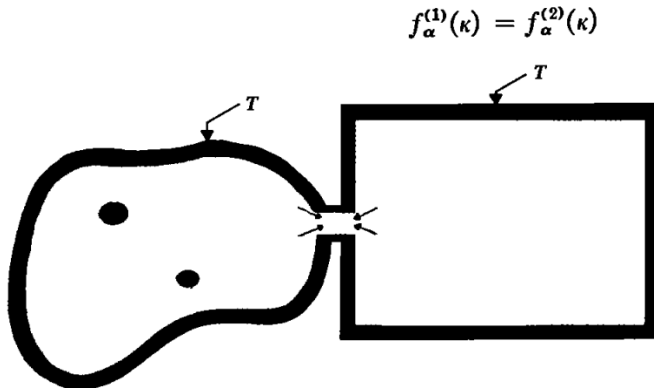
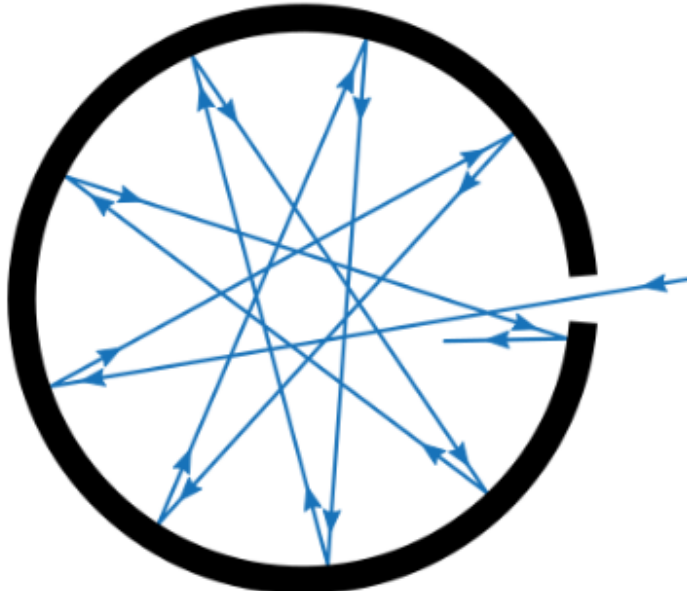


Figure 2.14: Two cavities in thermal equilibrium of arbitrary shape, material and physical contents contain equivalent radiation fields $f_\alpha(\kappa, r)$. Figure from Reif [39].

855 To further flush out argument four, picture a photon entering a metallic cavity (emissivity
 856 < 1) through a small hole as in Fig. 2.15. At each bounce, the photon has a probability of
 857 absorption given by the emissivity (a photon hitting a perfect black body has a 100% chance
 858 of being absorbed). As long as the geometry of the cavity allows many bounces of a photon
 859 entering before it finds its way out, even a highly reflective cavity will behave like a black
 860 body since an entering photon will likely be absorbed (and a new photon will be emitted
 861 with a wavelength that was drawn from the blackbody spectrum given by the temperature

862 of the walls).



,

Figure 2.15: A cavity with a small hole behaves like a black body as long as the probability of absorption $\ll 1$. The probability of absorption at each reflection is given by the emissivity, so the total probability of *reflection* is the emissivity raised to the power of the average number of bounces. Figure from Wikipedia.

863 The result is rather surprising conclusion; a cavity with a small aperture will behave as a

864 black body, and the spectrum emanating from a black bodies can not exhibit modal structure.

865 Therefore **a well matched antenna in a cavity will not measure modal structure**

866 **of the cavity.** This seems to defy intuition. Cavities are resonators, and resonators...

867 resonate?

868 The reason for the seeming discrepancy is that this intuition only holds in the the case

869 where we pump energy in, a situation which is nearly ubiquitous in engineering contexts.

870 However, pumping in energy breaks our fist assumption of equilibrium between the two

871 “cavities” (in this case, one of the “cavities” is a signal generator which, from the antenna’s
872 point of view, appears quite hot). A resonant cavity has the resonance it does because
873 photons are being pumped in faster than they can be absorbed by the walls and remitted
874 with a thermal distribution. In this driven case, the photons interfere in such a way as to
875 give modal structure. Turn the amplitude of the source down to $\approx kT$ and the modes should
876 vanish. This case, among others, will be investigated in the following subsections.

877 **2.3.2 Inspection of thermal noise spectra**¹⁰

878 The theory outlined above predicts the (input-referred) spectrum of an antenna in a cavity
879 should not vary with frequency if there is thermal equilibrium between the cavity and the
880 receiver system. A real measurement will take place after an amplifier (in other words, will
881 be output-referred), and will vary due to the gain and noise figure of the amplifier. A simple
882 way to correct for this is to compare the spectrum from an antenna and a terminator since
883 both will have identical gain and amplifier noise contributions. Since we are more focused on
884 the qualitative *shape* of the spectrum and not absolute input referred power, this method is
885 acceptable. A comparison of antenna and terminator data from an identical amplifier chain
886 is shown in Fig. 2.16.

¹⁰Code for this section can be found at: https://github.com/josephmlev/darkRadio/tree/master/daqAnalysisAndExperiments/run1p4/thermalNoiseVsH/thermalWiggles_writeup.ipynb

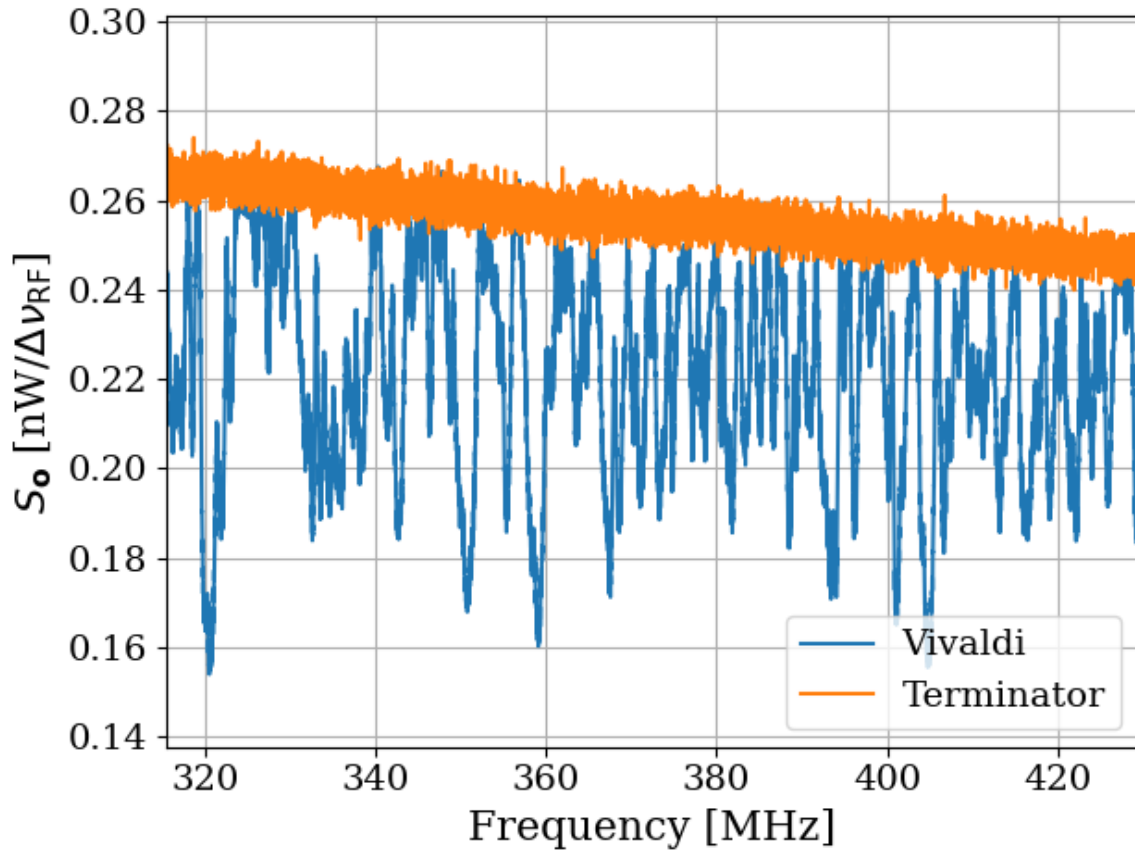


Figure 2.16: Output-referred vivaldi antenna and terminator spectra as measured through an amplifier chain ($G \sim 68$ dB, noise temperature ~ 120 K). Both spectra represent about 1 second of data, with $\Delta\nu_{\text{RF}} = 9.5$ kHz. Vivaldi antenna is in single position throughout all averaging, in contrast to the technique where it moves, outlined in later chapters.

887 2.3.3 A simple resonator: shorted coax cable

888 A coax cable which is shorted on one end and matched to a measurement device on the other
 889 is a simple resonator. The short provides a boundary condition demanding the voltage goes
 890 to 0 while the measurement device, being matched, absorbs the wave. A “closed-open”

891 resonator of length L will resonate with frequency

$$\nu = \frac{c\alpha(2n - 1)}{4L}, \quad (2.35)$$

892 for integer $n > 0$, where $\alpha \leq 1$ is the velocity factor and c is the speed of light. For a
893 185 cm cable with velocity factor = 69.5%, this works out to a first mode at 28.2 MHz and
894 following modes every 56.4 MHz. A schematic of the set up is shown in figure 2.17, and the
895 output power spectrum is shown in ratio to a terminator Fig. 2.18. Also shown in Fig. 2.18
896 is an open termination at the end of the cable in place of the short. Fitting the peaks¹¹
897 reveals the average spacing between peaks is 55.2 ± 2.4 MHz, in good agreement with the
898 prediction of 56.4 MHz of Eq. 2.35.

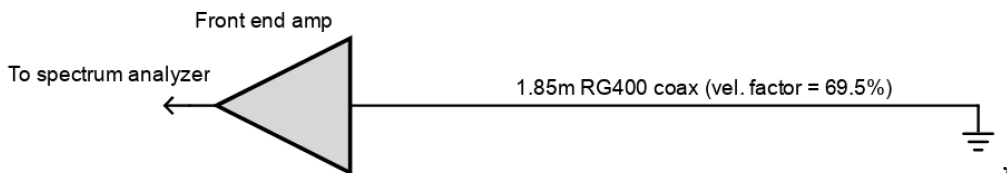


Figure 2.17: A coax cable with a short on the end and a matched measurement device on the other behaves like a “closed-open” resonator.

899 By the fluctuation dissipation theorem, the loss of the cable will dissipate some thermal
900 noise into the system, which can excite the cable. As discussed in the Sec 2.3.1, if the res-
901 onator (cable) is in thermal equilibrium with the measurement device, a flat power spectrum
902 is expected. The deviation from this expectation is surprising because the data seem to be
903 in contradiction with thermodynamics. Now, a cable is not a particularly good resonator

¹¹Code for this section can be found at: https://github.com/josephmlev/darkRadio/tree/master/daqAnalysisAndExperiments/run1p4/thermalNoiseVsH/thermalWiggles_writeup.ipynb

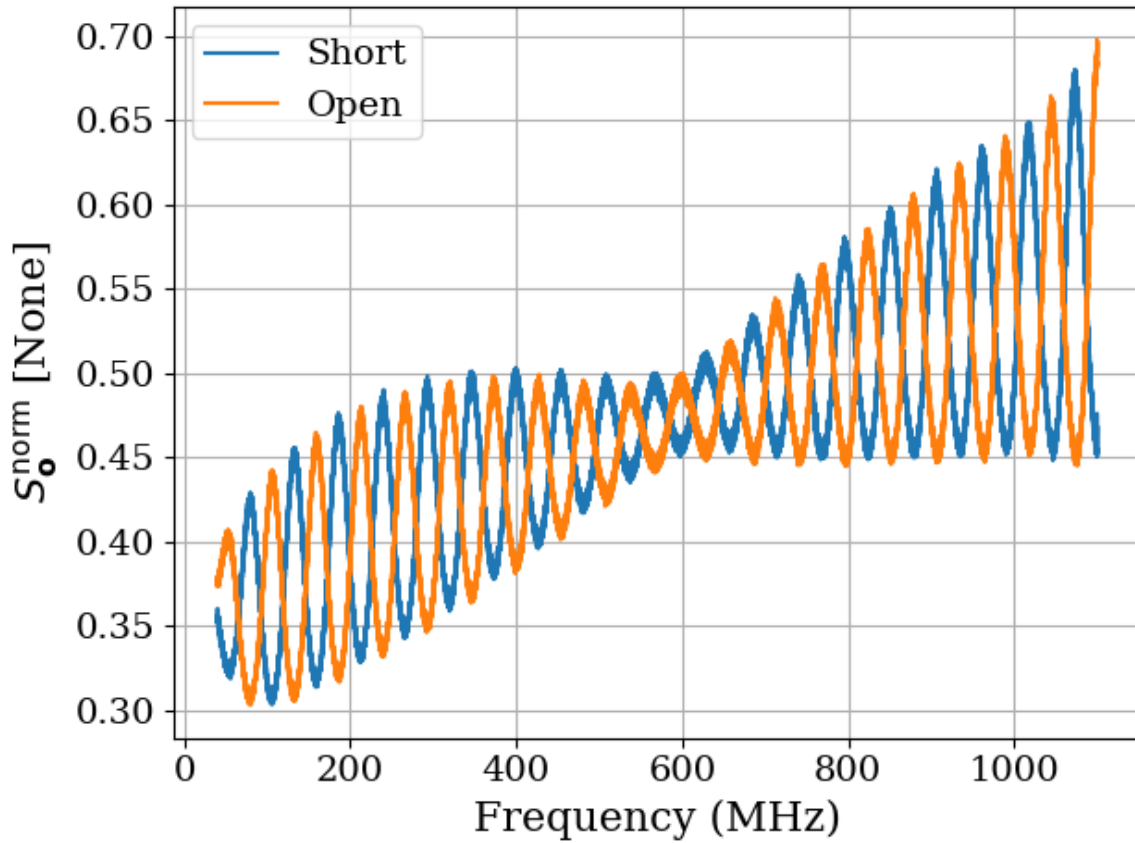


Figure 2.18: Power spectrum of short (blue) and open (orange) terminations at the end of 1.85 m of RG400 coax cable (velocity factor = 69.5%). Schematic of set-up shown in Fig. 2.17. Power is normalized to a terminator through the same amplifier chain. For example, when $S_o^{\text{norm}} = 0.5$, the power measured in this set up is half of the power measured by a terminator through the same amplifier chain. The average spacing between peaks is 55.2 ± 2.4 MHz, in good agreement with the prediction of 56.4 MHz of Eq. 2.35.

904 ($Q \lesssim 10$), so the effects are rather small here, but the simplicity of the system makes it one

905 that is worth exploring.

906 One assumption which is critical to the above logic is that of equilibrium. The amplifier is

907 a likely culprit for breaking this equilibrium, and so a test which can remove the amplifier's

908 ability to interact with the resonator is worth perusing. Fortunately, such a test is quite

909 simple to implement using a circulator.

910 **2.3.3.1 RF circulators**¹²

911 A circulator is a three port device which only allows power to flow between specified ports.

912 A schematic symbol is shown in Fig. 2.19

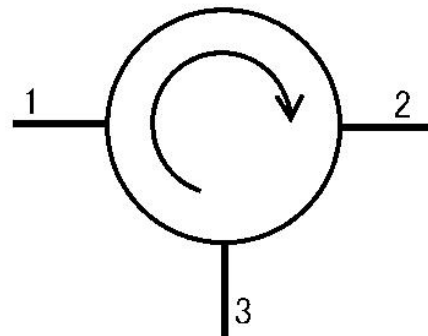


Figure 2.19: Schematic symbol of a circulator. Power can only flow from port 1 to 2, 2 to 3 and 3 to 1. Image from Wikipedia.

913 The S-parameters of an ideal circulator are given by the matrix

$$S = \begin{pmatrix} 0 & 0 & 1 \\ 1 & 0 & 0 \\ 0 & 1 & 0 \end{pmatrix}. \quad (2.36)$$

914 In other words, $S_{12} = 0$ so power can not flow from port 2 to port 1, while $S_{21} = 1$ so
915 power can flow from from 1 to 2. Also of note, the diagonal elements $S_{ii} = 0$, meaning ports
916 do not reflect power.

¹²Code for this section can be found at: https://github.com/josephmlev/darkRadio/tree/master/thesis/ch2/circulatorData/SParameter_circulator/calc3portSPParam.ipynb

917 A Teledyne C-0S03A-3M RF circulator has an approximate bandwidth from 490-510 MHz
918 and was available inexpensively on ebay, so it is used for testing. A photo of it is shown in
919 Fig. 2.20, and its S-paramater data are shown in Fig. 2.21.



Figure 2.20: Photo of Teledyne C-0S03A-3M RF circulator.

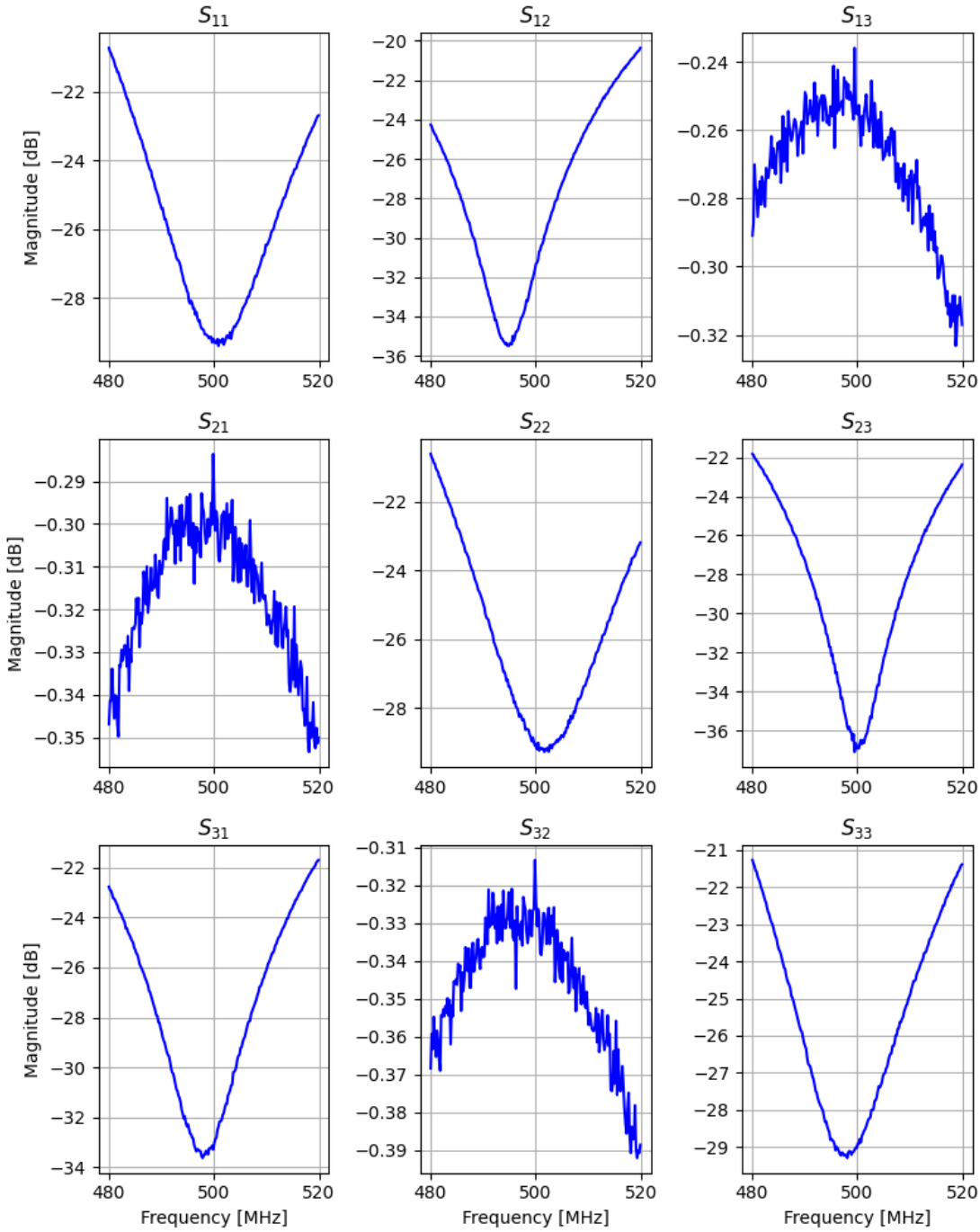


Figure 2.21: 3-port, frequency dependant S-parameter data for Teledyne C-0S03A-3M circulator. Data taken with 2-port VNA with the circulator's unused port terminated. Circulator is rated for use between 490 and 510M MHz. These data show good agreement with Eq. 2.36. Note that magnitude is in dB so these data are proportional to power, i.e. the square of linear S-parameters which are proportional to voltage.

920 2.3.4 A simpler resonator: shorted coax cable and circulator

921 In light the wiggles observed in Fig. 2.18, a similar measurement was made which isolates
922 the coax resonator from any effects of the amplifier. The schematic of this set up is shown in
923 Fig. 2.22, and the spectrum is shown in Fig. 2.23. This is an interesting measurement because
924 any net power flow from the amplifier will be seen by the terminator, but since the terminator
925 presents a good impedance match, this power flow will be absorbed by the terminator. This
926 net power flow has the potential to cause a temperature change in the terminator, however
927 it is in a thermally-conductive metal can exposed to the air which serves as a heat bath and
928 holds it very close to room temperature. The coax resonator will just see the Johnson noise
929 of the room temperature terminator, in equilibrium with its own Johnson noise caused by
930 its loss. The overall effect is a resonator which is in thermal equilibrium, yet is able to be
931 measured by an extremely sensitive spectrum analyzer.

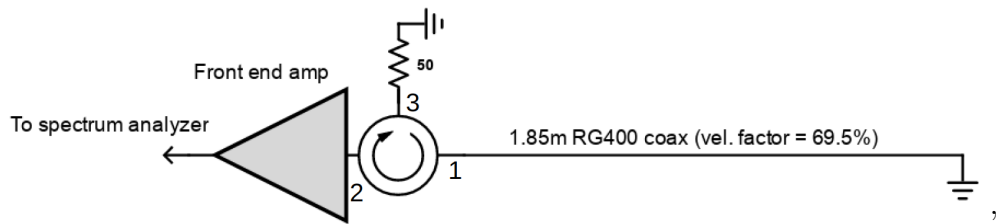


Figure 2.22: A coax cable with a short on one end and a circulator isolating the system from the amplifier.

932 The result of introducing the circulator (and a matched load on port 3) is the removal of
933 the wiggles that were seen without the circulator (Fig. 2.23).

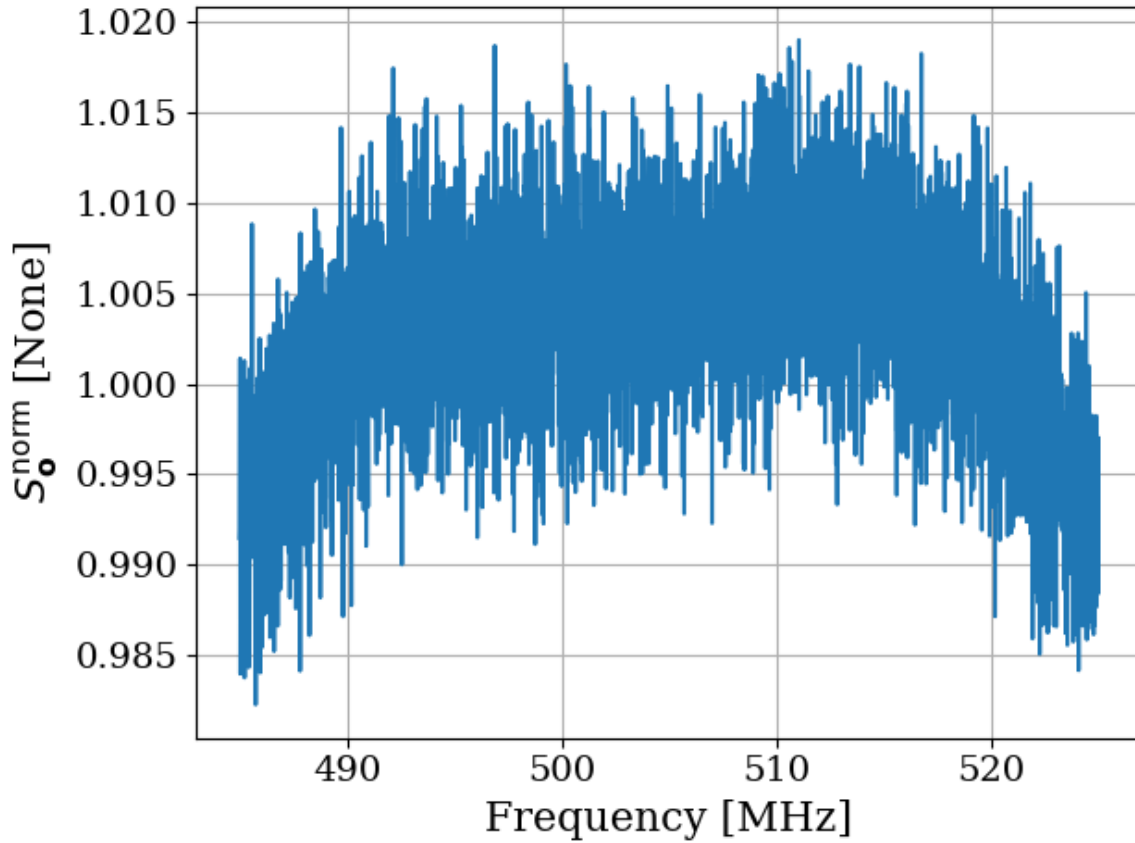


Figure 2.23: Power spectrum of 185 cm coax resonator as measured through circulator. Short termination at end of cable as depicted in Fig. 2.22. Wiggles in the spectrum are much smaller compared to Fig. 2.18, at least in the 490-510 MHz band where circulator is effective. Also note spectrum is normalized to a terminator through the same amp chain and very close to 1. The normalized spectrum without the circulator shown in Fig. 2.18 was significantly lower, around 0.5.

⁹³⁴ 2.3.5 A more complex resonator: antenna in room

⁹³⁵ Similar to the coax resonator shown in Fig. 2.17, the antenna data presented in Fig. 2.16
⁹³⁶ are of a resonator (antenna-room system) which is being measured by an amplifier. The
⁹³⁷ experiment in the previous section suggests that the amplifier seems to have an effect on
⁹³⁸ the delicate thermal equilibrium which can be mitigated by including a circulator. The

939 experimental set-up for the antenna in the room is shown in Fig. 2.24, and the data from
940 this set up is shown in Fig. 2.25.

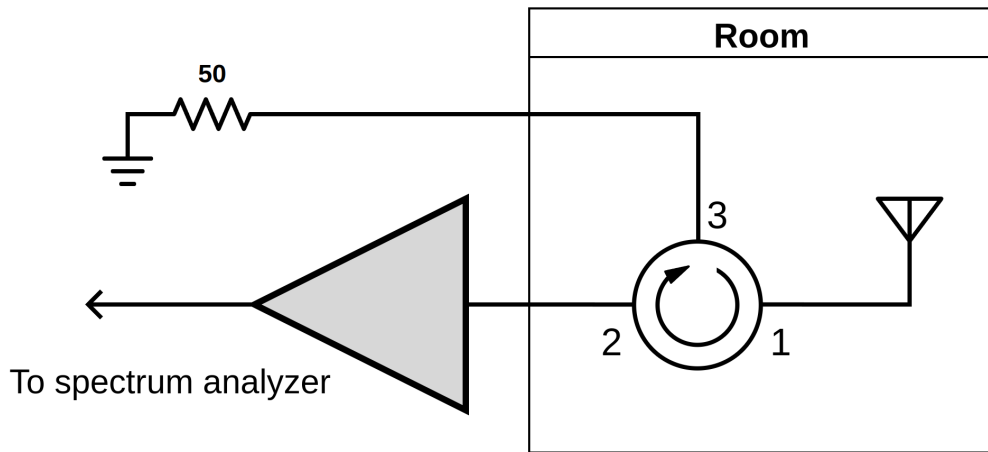


Figure 2.24: Schematic of experimental set-up using circulator to isolate antenna from amplifier effects.

941 A nice test case would be to measure the thermal noise of an extremely high Q cavity
942 after carefully ensuring the radiation which is allowed to enter has a black body spectrum of
943 the same temperature of the cavity. This is nicely demonstrated in a few places, notably by
944 Cervantes et. al with a cavity of $Q = 10^{10}$ (!!!) [29]. When care is taken to create equilibrium
945 here the resulting spectrum is flat on and off resonance (Fig. 2), and when this equilibrium
946 condition is broken, the cavity resonance is visible (Fig. 10).

947 2.3.6 Effective temperature of amplifier

948 At this point, the seemingly obvious explanation is that the amplifier, being warm, is sourcing
949 more power than it's absorbing. To test this theory, two amplifiers can be placed input-to-
950 input as shown in Fig. ???. The noise power emerging *out* of the amp-under-test's input will

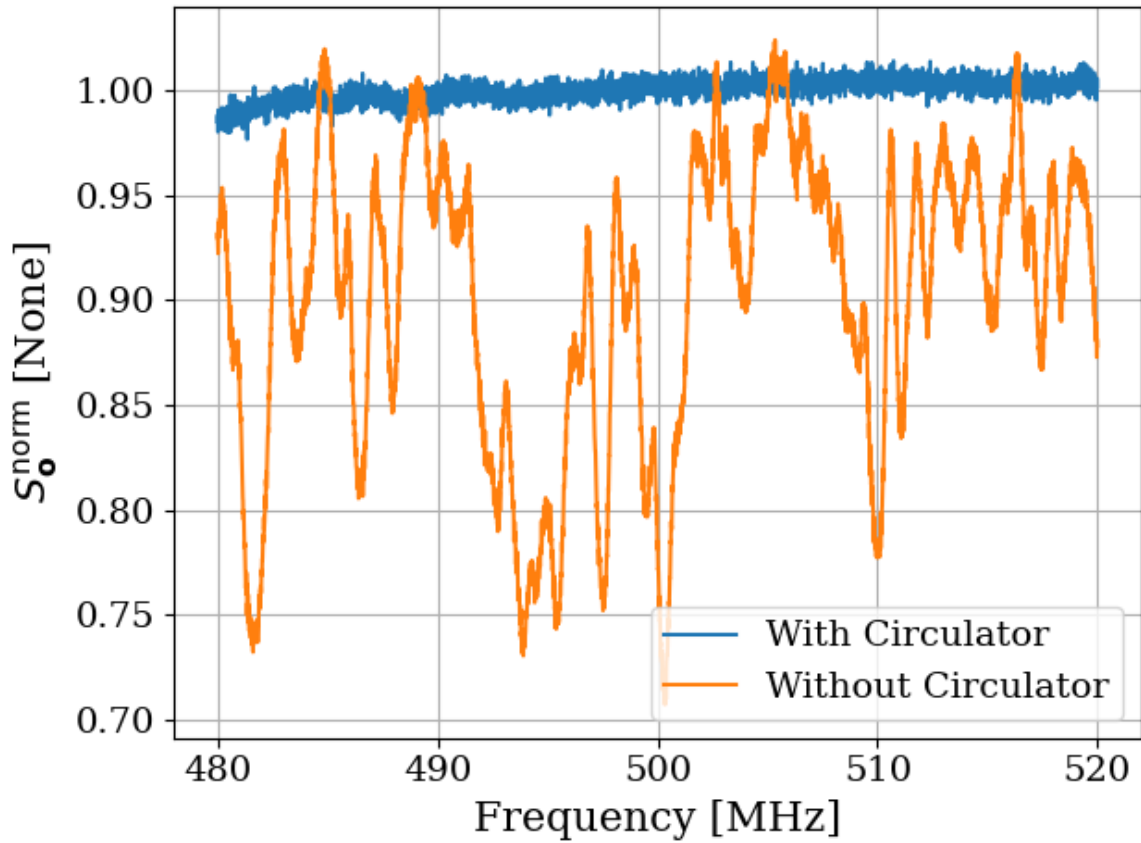


Figure 2.25: Normalized power spectrum for vivaldi antenna in room with circulator (blue). The normalized spectrum of the same antenna in the same position is shown with the circulator removed in orange for reference. This orange spectrum is the same as that shown in Fig. 2.16, but here it has been normalized to a terminator measured through the same amplifier chain. The terminaor is also shown in Fig. 2.16.

951 be measured by the front end amplifier. This amplifier has a noise temperature ~ 100 K, so
 952 it should be sensitive to very small variations in power.

953 The data from the set-up is shown in Fig. 2.27. Also shown in this figure are the spectra
 954 of the amp-under-test replaced by both short and open terminations for reference.

955 An interesting number to keep in mind is the noise floor of this detector and what it
 956 looks like in the dimensionless units shown. This is set by the noise temperature of the front

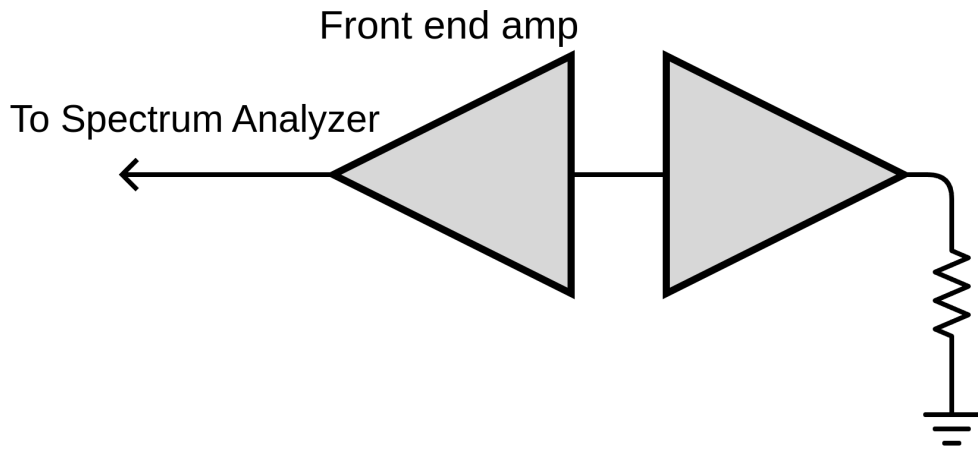


Figure 2.26: Schematic of set-up to measure the noise emerging *out* of an amplifiers input.

957 end amp, $\sim 100\text{ K}$. If the load-under-test were at 0 K , the power measured $S_{0\text{K}}^{\text{meas}}$ would be
 958 only that of the front end amp. Taken in ratio to a 300 K matched terminator measured by
 959 the same amp chain,

$$\frac{S_{0\text{K}}^{\text{meas}}}{S_{300\text{K}}^{\text{meas}}} = \frac{0 + 100\text{ K}}{300 + 100\text{ K}} \quad (2.37)$$

$$\approx 0.25 \quad (2.38)$$

960 Thus, anything with an apparent noise temperature $\ll 100\text{ K}$ will appear with a dimensionless power spectral density of ~ 0.25 in Fig. 2.27.
 961

962 This phenomena actually has been discussed in the literature[16]. ¹³, which I will provide
 963 a brief summary of.

964 In this case, two amplifiers are placed back to back at either side of a transmission line.

¹³I am very grateful to Greg Wright for pointing this out.

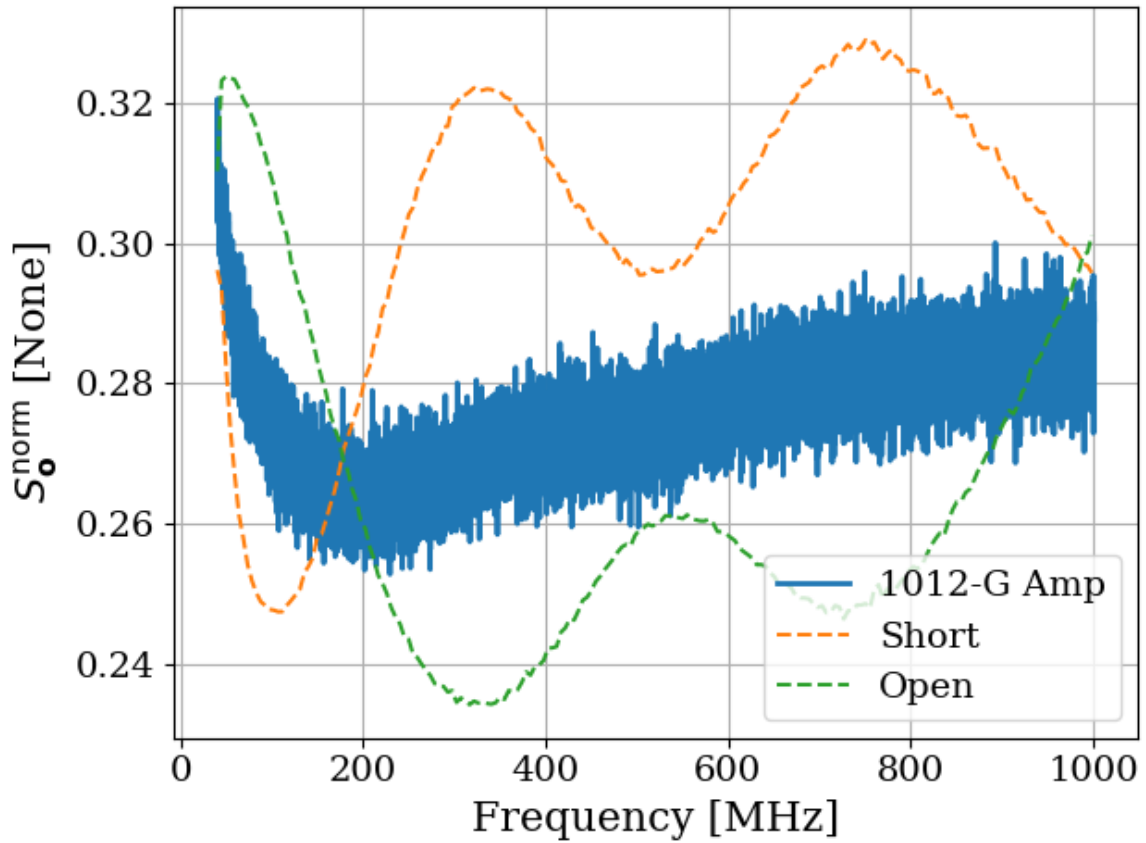


Figure 2.27: Power spectrum of noise emerging *out* of the input of an amplifier’s (Pasterнак PE15A-1012-G) input, see Fig. 2.26. Normalized to a matched 50Ω terminator. Also shown as dashed curves are the spectra of a short and open termination. These spectra have a median fit applied to reduce visual clutter.

965 When a particle interacts with the transmission line, a pulse is detected at each of the
 966 amplifiers, and the difference in time provides a means to work out the position the particle
 967 came in along the line. It is advantageous in this case to minimize the noise emanating out
 968 of the inputs of these amplifiers. By tuning the reactance of the input of these amplifiers,
 969 they can absorb a net power, putting them at an “effective temperature” lower than their
 970 physical temperature.

971 In the case of off-the-shelf Pasternack RF amplifiers, this was likely not an intentional
972 effect. However, the data presented here seem to agree with the idea that the amplifiers have
973 an effective temperature $\ll 100\text{ K}$.

974 In the next subsection, I will demonstrate that by changing the temperature of the
975 matched load outside the shielded room (shown in Fig. 2.24), the amplitude of the thermal
976 wiggles can be controlled.

977 **2.3.7 Intentional breaking of thermal equilibrium**

978 At this point, it has been demonstrated that an amplifier absorbs more thermal noise than
979 it emits. This causes the spectrum of a resonator which is measured with such an amp
980 to exhibit wiggles, which disappear with a circulator is used to isolate the system from the
981 amplifier. An interesting question naturally arises; what happens when the the thermal
982 equilibrium is disturbed by varying the temperature of the 50Ω terminator on port 3 of the
983 circulator (Fig. 2.24)? Since the terminator is outside the room, it is simple to conduct a
984 highly controlled experiment where the terminator's temperature is varied without entering
985 the room and moving conductors.

986 - show slide 24, 25 26

987 **2.3.8 Relation of antenna S_{11} to thermal noise without a 988 circulator**

989 - slide 30

990 **2.4 Reverberation Chambers and Statistical**

991 **Uniformity**

992 Generally it is convenient to think of electromagnetic cavities as containing a single mode
993 which can be modeled by applying Maxwell's equations with the appropriate boundary con-
994 ditions. The differential equations which must be solved are rather clean and have analytic
995 solutions which vary sinusoidally in both space and time.

996 **2.5 System Design**

997 This section outlines the subsystems which make up the experiment. While specifics and
998 basic calculations are provided as they apply to design choices of subsystems, testing and
999 characterisation of the system as a whole is left to Ch. 3. A simplified schematic of the
1000 entire experiment is shown in Fig. 2.28 and a photo of the lab is shown in Fig. 2.29.

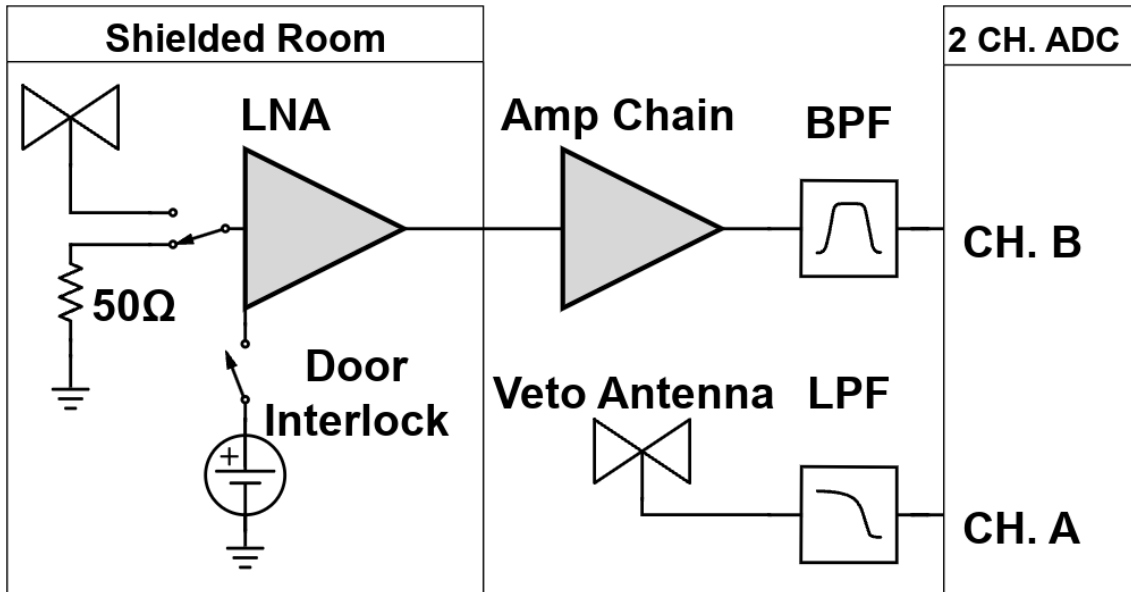


Figure 2.28: Schematic of the RF receiver system. An RF coax switch allows the PC to control the source (antenna or terminator). The amplifier chain is shown with more detail in Fig. 2.33. The switch is controlled by optical fiber to maintain isolation of the room. The LNA (Pasternack PE15A1012) has a nominal gain and noise temperature of 40dB and 100K (measurements shown in Sec. 3.1.1). It is interlocked (Fig. 2.34) to the door to protect amp B and the ADC from large signals when the door is open. The secondary amplifier is a Mini-Circuits (MC) ZKL-1R5+ and has a nominal gain of 38dB. Not pictured after this amplifier is a fixed 4dB of attenuation. The band pass filter (BPF) defines the experiment's bandwidth, $-3 \text{ dB} \approx 40 - 320 \text{ MHz}$ and is discussed in Sec. 2.5.4. The veto antenna is outside of the room and interference is not reduced by the $\approx 100 \text{ dB}$ SE of the room, so no gain is required. The low pass filter (LPF) on the veto is for anti-aliasing.



Figure 2.29: Photo of dark radio lab. Shielded room contains the main antenna as well as the LNA and power supply (not visible). Veto antenna can be seen hanging outside of shielded room. Photo taken looking south.

1001 **2.5.1 Shielded room**

1002 The shielding room [40] serves two purposes. The first is straightforward; to shield the
1003 antenna, keeping radio frequency interference (RFI) *out*. The second purpose is a bit more
1004 subtle; to keep any converted dark photons *in*. This second point is addressed further as an
1005 aspect of system calibration in Ch. 4, but roughly can be described by the loaded quality
1006 factor [41–43] of the antenna/room system. Namely, a more resonant system will be more
1007 sensitive to coherent signals. This subsection will focus on the first point, keeping RFI out.

1008 Shielding effectiveness SE is a measurement of a shielding enclosure's ability to attenuate
1009 electromagnetic waves from entering,

$$\text{SE} \equiv 10 \log_{10} \left(\frac{P_{\text{open}}}{P_{\text{closed}}} \right) = P_{\text{open}, \text{dB}} - P_{\text{closed}, \text{dB}} \quad (2.39)$$

1010 where $P_{\text{open}}/P_{\text{closed}}$ are powers received with the door open/closed. The ratio of powers
1011 allows all the specifics of antenna matching to cancel allowing for a very simple differential
1012 measurement. The results of this are described in Sec. 3.2.

1013 Another important measurement are the dimensions, shown in table 2.2. I carefully
1014 measured the room with a laser range finder which I checked against a tape and gives good
1015 agreement to 1 mm¹⁴. The room is out of square by a few mm, especially height measured
1016 in the south-west corner compared to the height measured everywhere else. This is the most
1017 extreme deviation, and is about 5 mm.

¹⁴After a year I dropped it and it now gives crazy readings which jump around by 10s of cm. Be careful!

Direction	Coordinate	Nominal Length [ft]	Measured Length [m]
West-East	x	10	3.070
Vertical	y	8	2.457
North-South	z	12	3.684

Table 2.2: Direction, coordinate, and length measurements of shielded room in lab 314. Note that Fig. 2.29 is looking south, so x is right-left and z is into the page. Note that these are the mean values of several measurements. The room was found to be about 5mm out of square, so these should be interpreted as ± 5 mm.

2.5.2 Antenna

The antenna plays an important role in the experiment as the matching device between electromagnetic waves in the cavity and the 50Ω receiver system. For a broadband search such as the 50-300 MHz run (a 6:1 bandwidth), a broadband antenna must be used. The chosen antenna must provide a good impedance match and high efficiency since an inefficient antenna would convert a substantial amount of the converted dark photon's power into heat within the antenna's structure. The antenna is connected to the RF switch via a low loss (0.45dB at 300 MHz) 21 ft. LMR400 cable. This contributes about 31.6 K to the ≈ 400 K antenna noise, see Eq. 2.27. Note that the final limit on epsilon scales with the square root of system temperature, so this is only a few percent degradation in the final limit after a 9 day run.

For the 50-300 MHz run, a ≈ 131 cm biconical antenna (bicon) was chosen. The selected model is manufactured by COMPOWER, model AB-900A [44]. In a phone call with the manufacturer as well as testing of the isolated balun, it was determined that the balun used in the antenna was 1:1. This allows for simple simulation of a free-space aperture which

1033 agrees remarkably well with manufacturer data, Fig. 2.30. In COMSOL [45], the lumped
1034 port option allows for a balanced drive of an antenna. A match to a 50Ω transmission line
1035 through a 1:1 balun is simply modeled as a lumped port, a very simple object in COMSOL
1036 featured in nearly all of the antenna tutorials¹⁵. Additionally, there is good agreement
1037 between simulated and measured antenna impedance, see Fig. 2.31.

¹⁵See for example the dipole antenna tutorial, available at <https://www.comsol.com/model/dipole-antenna-8715>

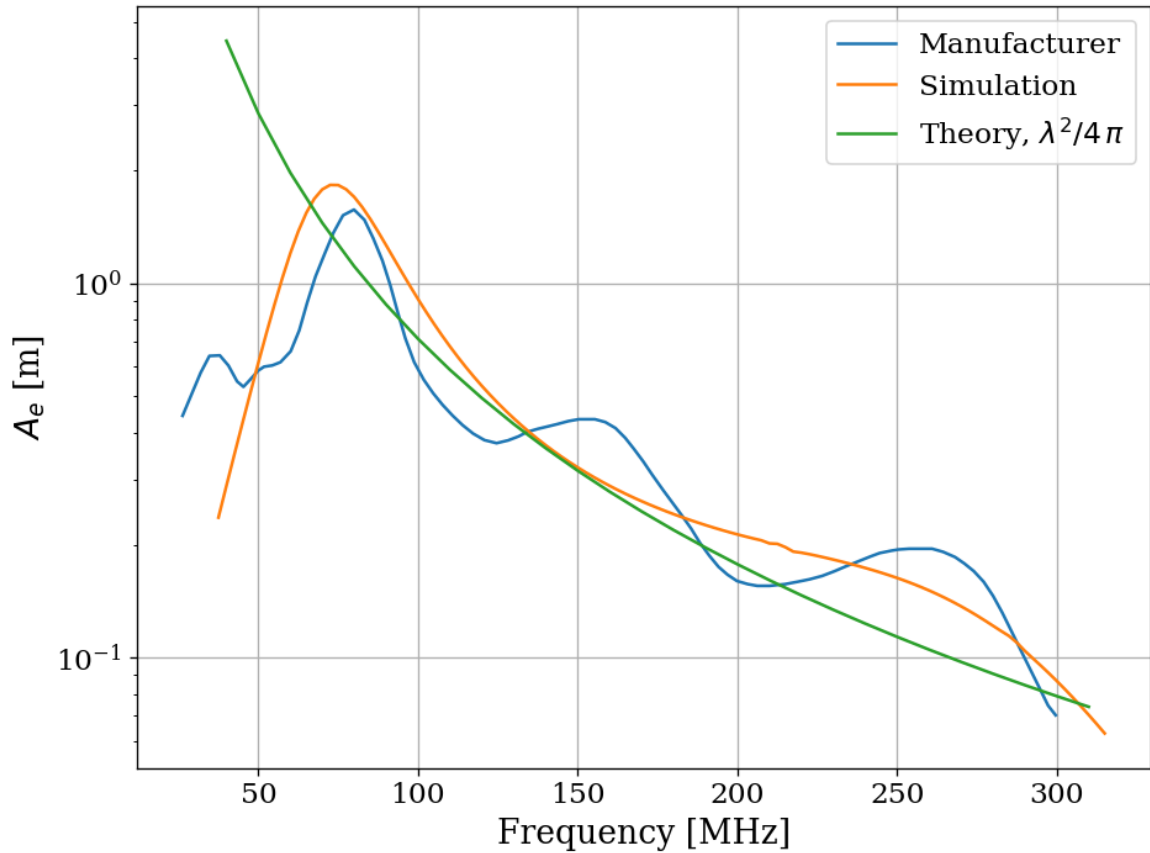


Figure 2.30: AB-900A biconical antenna effective aperture, simulated, measured and theoretical in free space. Simulation performed in COMSOL [45]. The measurement was provided by manufacture [44] as an antenna factor and was converted to aperture. Wiggles observed in manufacturer’s measured data are the result of testing over a ground plane and are a known discrepancy between simulations and measurements of “free space” antenna factor. See for example [46] **comment: aperture units wrong, reprint plot**

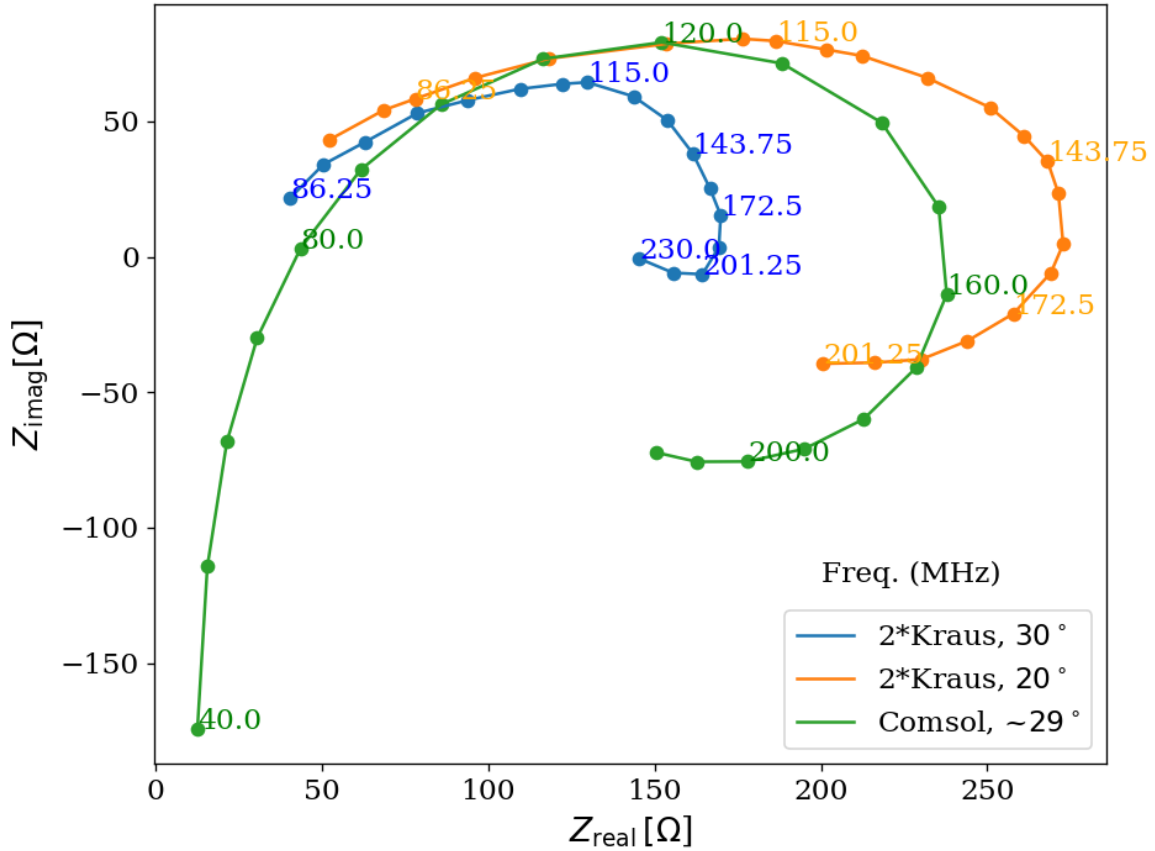


Figure 2.31: Simulated AB-900A biconical antenna free space complex input impedance shown in blue. Simulation was performed in COMSOL. Measurement from Kraus' Antennas, second edition, Fig 8-13 [47]. Measured data is for a monoconical antenna and must be multiplied by 2 to compare to a biconical antenna as discussed in Kraus. Numbers along curve indicate frequency in MHz.

1038 **2.5.3 Terminator and fiber-optic switch control**

1039 Experience has shown that it is advantageous to have a stable noise reference at the begin-
1040 ning of the signal chain to monitor system performance. One may think the antenna can
1041 provide this following Sec. 2.1.1.2, but in practice, the antenna is not that stable, Sec. 2.3.
1042 Furthermore, while RFI was not significant in the actual run, it very well could have been,
1043 introducing some uncontrolled, coherent power into the spectrum which would have had an
1044 unknown origin. A terminator will give a very constant noise power density $S_{\text{term}} = kT$
1045 regardless of RFI and antenna position. For this reason one is included. It is at the same
1046 temperature as the walls, and is a nice passive solution. The RF switch shown in Fig. 2.28
1047 is actuated periodically during the run to measure the terminator's noise power through the
1048 same amplifier chain as the antenna. The terminator is connected to the switch via a 21
1049 foot cable (LMR 400) which is identical to that of the antenna. The switch is controlled via
1050 a fiber-optic link in order to reduce RFI. The fiber optic is an extremely important feature
1051 which was overlooked for several years at the beginning of the experiment leading to lots of
1052 RFI.

1053 **2.5.4 Signal conditioning**

1054 As discussed in Sec. 2.1.5, the ADC has internal signals which are mitigated by introducing
1055 gain before the ADC. The amount of gain must be carefully chosen, since too much will cause
1056 the ADC to clip. Additionally, high frequencies must be limited before digitizing to prevent
1057 aliasing. To accomplish this, several RF components must be selected to condition the analog

1058 signal: an LNA, a secondary amplifier, band pass filter and several attenuators.

1059 **2.5.4.1 Low noise amplifier**

1060 The important concepts of the LNA have been introduced in Sec. 2.1.4. The key takeaway
1061 is that low noise gain helps to mitigate signal-to-noise degradation that occurs later in the
1062 signal path. Relevant specifications for the Pasternack PE15A1012 [33] are summarized in
1063 table 2.3.

Specification	Value	Uncertainty (50-300MHz)	Units
Frequency Range	50-1,000	-	MHz
Gain	40	± 1	dB
Noise Temperature	110	± 10	K
Input Return Loss	< -15	-	dB
Output Return Loss	< -15	-	dB
Price	500	-	USD
Voltage	9-15		V
Current	100	10	mA

Table 2.3: Specifications for the Pasternack PE15A1012-E. The voltage is regulated internally, so the exact voltage supplied is not critical, though there is a slight gain dependence on voltage since a higher voltage causes the amp to run warmer, see Fig 3.9.

1064 We have several identical amplifier which are labeled with letters. At the time of writing,
1065 amplifiers A-D are out of commission. Amplifier E was used for run 1.4.

1066 **2.5.4.2 Secondary amplifier**

1067 As discussed in 2.1.4, the noise temperature of a secondary amplifier has negligible impact
1068 on the total system noise temperature. For this reason a cheaper secondary amplifier is
1069 used. The specifications for the Mini-Circuits ZKL-1R5+ [48] are outlined in Table 2.4.

1070 This amplifier has no internal regulator, so gain and noise temperature depend strongly on
1071 the bias voltage. Voltage was set to 9.05 V for run 1.4 using an external regulator (built
1072 around a TI LM317 [49]).

Specification	Value	Uncertainty (50-300MHz)	Units
Frequency Range	50-1,000	-	MHz
Gain	40.5	.3	dB
Noise Temperature	275	15	K
Input VSWR	<1.14	-	dB
Output VSWR	<1.37	-	dB
Price	235	-	USD
Voltage	9-15	-	V

Table 2.4: Specifications for the Mini-Circuits ZKL-1R5+ as measured with 9.05 V bias.
There is no internal regulator, so the voltage is set using an external regulator (built
around a TI LM317 [49]).

1073 2.5.4.3 Band pass filter

1074 The band pass filter has two purposes. The first purpose is to minimize the bandwidth
1075 entering the ADC. This allows for introducing as much gain as possible without wasting
1076 power amplifying frequencies where the antenna doesn't offer a good match. This will be
1077 computed below in Sec. 2.5.4.4. The second purpose is to prevent aliasing¹⁶. Aliasing occurs
1078 when the analog signal contains frequency components at frequencies greater than half the
1079 sample rate, in otherwords when the signal and ADC don't obey a condition called the
1080 Nyquist criterion, $\nu_s/2 \geq \nu$, where ν_s is the sample frequency and ν is the frequency of the
1081 analog signal.

¹⁶Aliasing is rather complex topic which is greatly simplified here. Wikipedia's aliasing page is an excellent reference. For a more rigorous treatment, see Ch. 7 Sec. 3 of the second edition of Signals and Systems by Oppenheim et. al [50]

1082 When this criterion is not met, higher frequencies are mapped back down to a lower
1083 frequency, described by the aliasing formula:

$$\nu_{\text{alias}} = |\nu_{\text{signal}} - n \times \nu_s|, \quad (2.40)$$

1084 where ν_{alias} is the aliased frequency, ν_{signal} is the original signal frequency, ν_s is the
1085 sampling rate, and n is an integer which specifies the Nyquist zone. In the simple case
1086 with bandpass filters that roll off well within the first Nyquist zone, only $n = 1$ must be
1087 considered.

1088 As an example, a $\nu_{\text{signal}} = 500$ MHz signal sampled at $\nu_s = 800$ MHz (the run 1.4 sample
1089 rate), it would alias to $\nu_{\text{alias}} = 300$ MHz. This also means that 1,300 MHz (residing in the
1090 second Nyquist zone) would alias down to 300 MHz, but again this and higher frequencies
1091 won't be considered. This means that by choosing only to analyze frequencies less than 300
1092 MHz, only frequencies greater than 500 MHz will alias into this analysis span.

1093 The Mini-Circuits ZX75LP-288-S+ low pass filter[51] serves as the anti-aliasing filter in
1094 run 1.4. It has an insertion loss of 68 dB at 500 MHz, while being flat to within 2dB from
1095 50 to 300 MHz. Additionally, the Mini-Circuits SHP-50+ [52] is used as the high pass filter.
1096 When connected in series, these two filters constitute the band pass filter shown in Fig. 2.28.

1097 2.5.4.4 Putting together a signal conditioning chain

1098 The total gain required can be estimated by setting the output referred power of bandlimited,
1099 400 K noise source times the gain equal to the maximum power the ADC can handle,

1100 $V_{\text{RMS}}^2/Z = 0.63 \text{ mW}$ for $Z = 50 \Omega$. Assuming a perfect filter from 50-300MHz (a 250 MHz
1101 bandwidth), the gain required is

$$G = \frac{0.63 \text{ mW}}{k 400\text{K} 250 \text{ MHz}} = 4.5 \times 10^8 = 87\text{dB}. \quad (2.41)$$

1102 Noise is a Gaussian random process however. This much gain ensures 1σ of the time
1103 domain samples are below clipping. Since many samples are collected ($2^{24} \approx 1.6 \times 10^7$ in
1104 run 1.4), and each has a probability of about 16% of clipping, many samples will clip with
1105 87 dB of gain. However, it gives a good estimation for what to expect.

1106 The band pass filter is not a brick wall from 50 - 300 MHz as was assumed in 2.41. The
1107 effective bandwidth of a filter is defined here as the integral of the square magnitude of it's
1108 through gain,

$$B_{\text{eff}} \equiv \int_{-\infty}^{\infty} d\nu 10^{S_{21}/10}. \quad (2.42)$$

1109 Where S_{21} is measured in dB and we are interested in integrating a quantity that is
1110 proportional to linear power, so it is divided by 10 rather than 20. The linear S parameters
1111 of components connected in series multiply, but since dB are logarithmic, this is equivalent
1112 to adding their S-parameters (in dB). Also note that $S_{21} \equiv \text{IL}$, the insertion loss. Insertion
1113 loss is frequently given on data sheets.

1114 With all this in mind, we can compute $B_{\text{eff}} = 237.06 \text{ Hz}$ for the actual filters (Mini-
1115 Circuits SLP-50+ high pass filter and Mini-Circutis ZX75LP-288-S+ low pass filter) from
1116 their data sheets. Curves of S_{21} for the real band pass filter and an ideal brick wall filter are

1117 shown in Fig. 2.32. Note that it is actually slightly less than the ideal 250 MHz bandwidth
1118 since there is some loss in band.

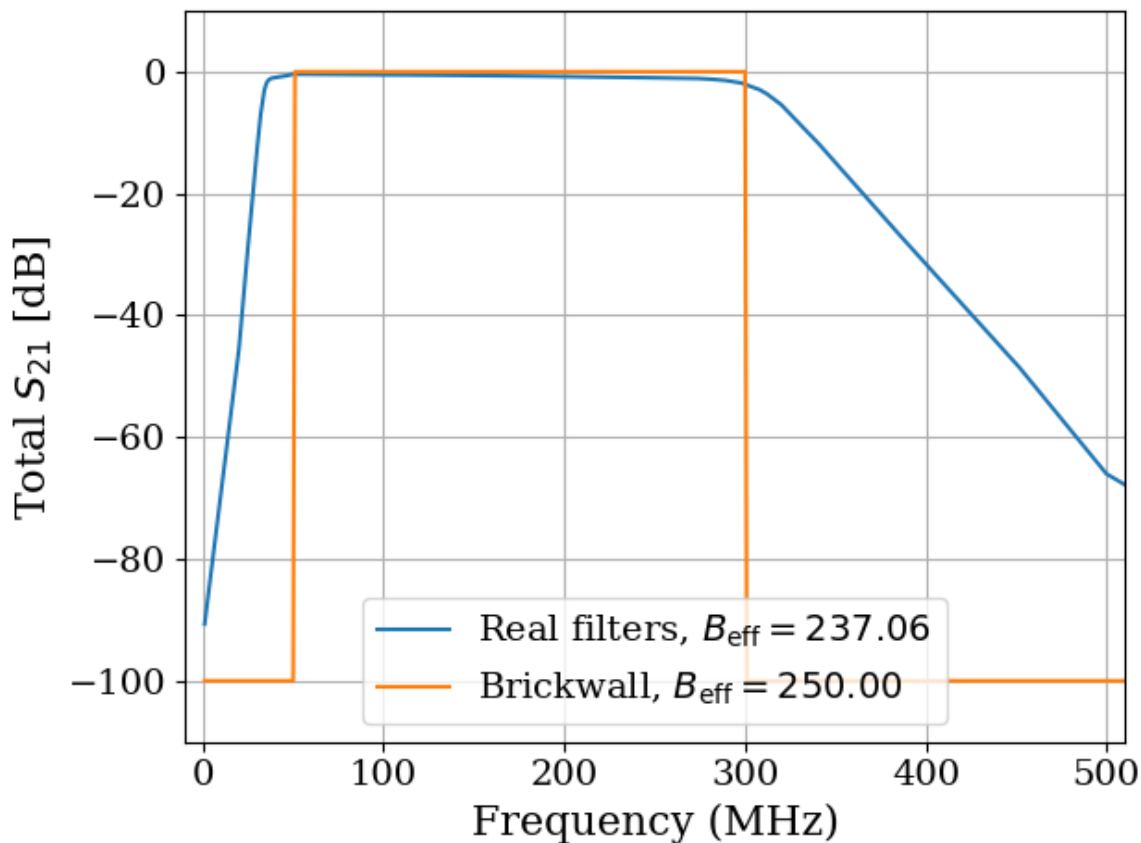


Figure 2.32: Through gain (S_{21}) of bandpass filter. Shown in dB, however B_{eff} is computed with linear S_{21} as in Eq. 2.42. Ideal brickwall filter shown for reference.
comment: Add Hz in legend

1119 Setting the gain is ultimately done by trial and error; taking a scan, adding some atten-
1120 uation if it clips, taking a scan, etc. Experience and preliminary simulations have shown
1121 that a few dB of clipping for an noise-dominated signal actually doesn't matter much, but
1122 this was not fully explored. If future runs are to scan for longer, they may have a significant
1123 contamination from ADC spurs (see Sec. 2.1.5.1), so additional gain driving into clipping

¹¹²⁴ may be fruitfully explored. Every dB of gain added allows for $10^{1dB/5} \approx 44\%$ more averaging
¹¹²⁵ before ADC effects are at the same relative level ¹⁷, so a little extra gain goes a long way.

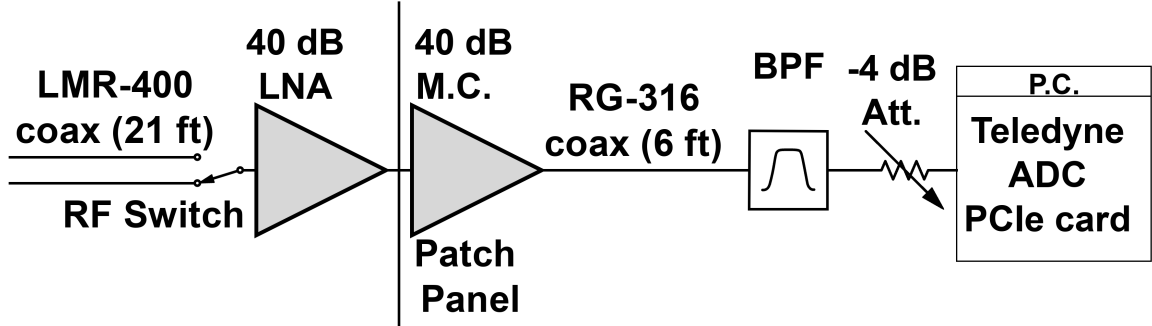


Figure 2.33: Schematic of Run 1A amplifier chain. Antenna (Sec. 2.5.2) and terminator (Sec. 2.5.3) are not part of the amplifier chain, and therefore not shown, but would be at far left of schematic. All RF connectors are SMA, except the connection between the bicon antenna and its cable which is N type (though that cable has SMA on the switch-side). RF switch is Teledyne CR-33S8D-T. 40 dB LNA is Pasternack PE15A1012-E (Table 2.3). Patch panel uses an SMA bulkhead connector labeled “A” (far left-hand side when standing outside the shielding room, as shown in Fig. 2.29). 40 dB Mini-Circuits (M.C.) is Mini-Circuits ZKL-1R5+ (Table 2.4). Band pass filter (BPF) is made up of Mini-Circuits SLP-50+ high pass filter and Mini-Circutis ZX75LP-288-S+ low pass filter. Note that filters and attenuator are directly connected to the SMA port of the Teledyne ADC (Sec. 2.5.7) to mitigate RFI received in the RG-316 cable run.

¹¹²⁶ 2.5.5 Veto antenna

¹¹²⁷ The veto antenna is an identical Compower AB900 bicon antenna [53] as is used in the
¹¹²⁸ shielded room. It is connected to channel A of the ADC, with no amplification. However,
¹¹²⁹ it has a Mini-Circuits ZX75LP-288-S+ low pass filter [51] to prevent aliasing. This is the
¹¹³⁰ same model low pass filter which is used for the main channel. The antenna is hung a few

¹⁷Calculations in dB like this are handy once they are understood, but can seemingly come out of nowhere. This can be worked out by a careful reading of section 2.2, using properties of logarithms and definition of the dB.

1131 feet in front of the door from some pipes on the ceiling. The proximity to these pipes likely
1132 give the antenna a strange response, but it's purpose is simply to look for large RFI signals,
1133 so this isn't that important.

1134 **2.5.6 12 V power system**

1135 The LNA and switch are active component which require power to operate. The experiment
1136 is incredibly sensitive to RFI, so while there is 120 VAC in the room, it is simpler to provide
1137 the power from a 12 V battery than use a AC/DC regulator. Originally a 12 V lithium-ion
1138 (LiFePO₄) battery was used. Lithium-ion batteries contain several cells and a controller
1139 to regulate charge/discharge between the cells. In order to remove the possibility of this
1140 controller emitting RFI in the room (which would create candidates that would be extremely
1141 difficult to veto), the lithium-ion was replaced with a 12 V lead acid golf cart battery ¹⁸.

1142 The LNA is interlocked to the door such that power is cut when the door is opened. This
1143 prevents the large radio signals being amplified once they enter the room and protects the
1144 ADC. The circuit that controls this is shown in Fig. 2.34. Note that it takes a few seconds
1145 for the slow turn on circuit to discharge, so the door should be opened slowly

¹⁸This was done between run 1.2 and 1.3 due to interference resulting in many candidate detections. Most of these were likely external RFI which were eliminated by cleaning the door (discussed in Sec. 3.2. Two variables were changed (cleaning of the door and replacement of the battery) so it's unclear if a lead acid is necessary. It works however, and if it aint broke don't fix it.

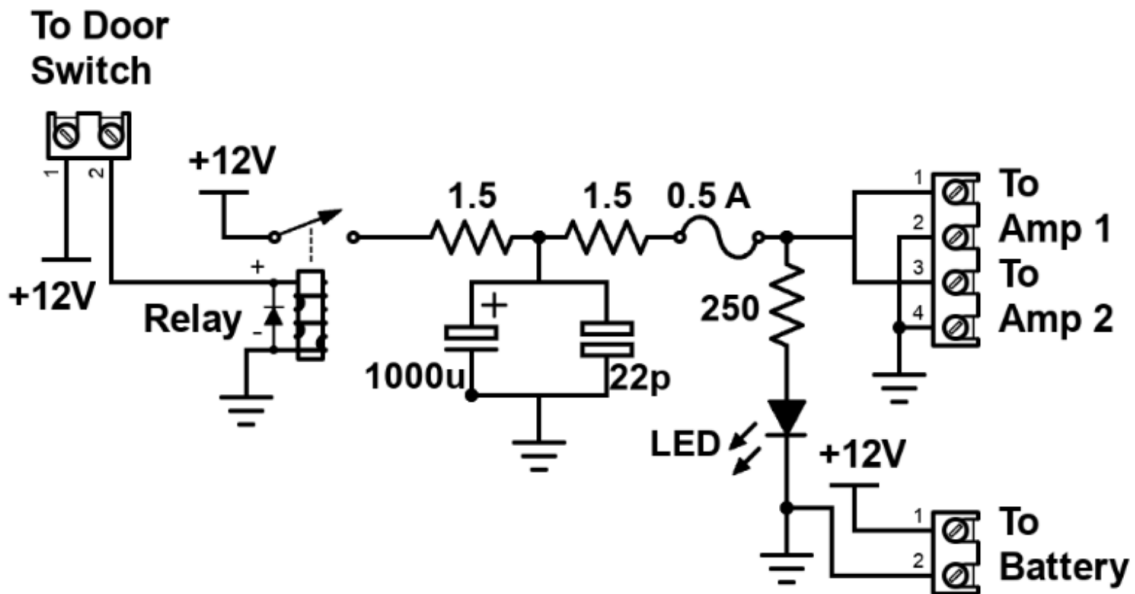


Figure 2.34: Schematic of Interlock board. No voltage regulation is provided because it is designed to work with amplifiers containing internal regulation (Pasternack PE15A1012 [33]). Not shown is a simple “slow turn on circuit” consisting of a 0.68 F capacitor and a 8Ω , 10 W resistor (time constant = 5.4 seconds) which was installed to protect the amplifier from transient voltages when the door is closed. This circuit can be seen in Fig. 2.35. Experience has shown the liberal use of fuses to be prudent when working with car batteries in a metal room.

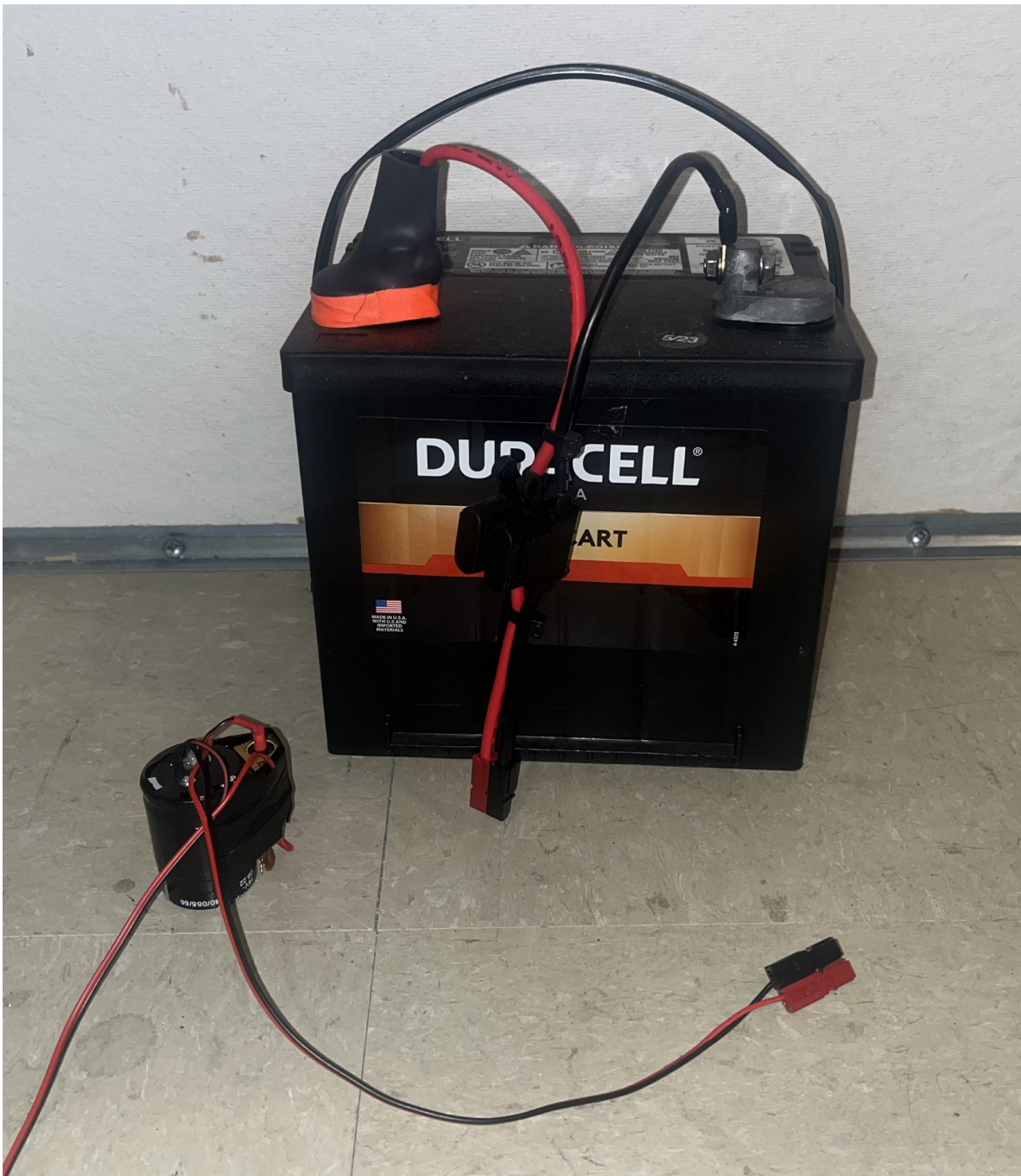


Figure 2.35: Photo of 12V lead-acid battery and slow turn on circuit. Both connect directly to the interlock board shown in Fig. 2.34. Slow turn on circuit is connected between interlock board and amplifier. Battery includes a 2A fast fuse installed in commercial Anderson power pole assembly.

1146 **2.5.7 GPU-Based Real-Time Spectrum Analyzer**¹⁹

1147 The use of commercial Spectrum Analyzers (SAs) which feature so-called real time spectrum
1148 analyzer (RTSA) mode come with several restrictions which limit the efficiency with which
1149 they are able to perform wide-band scans with narrow frequency resolution, as pointed
1150 out the dark radio pilot run [4]. The number of frequency bins output by a real discrete
1151 Fourier transform (DFT) is equal to half of the number of time domain samples, while the
1152 bandwidth is given by half of the sample rate. Furthermore, the ability to acquire data in real
1153 time requires a DFT algorithm (generally implemented as a fast Fourier transform, FFT)
1154 and computational resources which can operate on time domain data at least as fast as it is
1155 acquired. In practice, real-time DFTs with high frequency resolution and wide bandwidth
1156 require modest memory, transfer rates and processing resources. Commercial “real time
1157 spectrum analyzers” tend to cheat a bit to reduce hardware requirements. Frequency mixers
1158 reduce required sample rate (and therefore span), limits on FFT lengths reduce either span
1159 or resolution, and limits on rate of scans make it so that these SAs aren’t real-time (at least
1160 in the sense that we require them to be).

1161 For this reason, I have constructed a custom SA based on the Teledyne ADQ32 PCIE
1162 digitizer[34], which is wide-bandwidth (up to 1.25 GHz frequency span), high resolution
1163 (2^{24} point FFT), and nearly 100% real-time (see Fig. 3.17). I have been unable to find a
1164 commercial SA with comparable capabilities. Specifications are shown in table 2.5.

¹⁹Code for this section can be found at: <https://github.com/josephmlev/darkRadio/tree/master/daqAnalysisAndExperiments/teledyne>

Bit depth	12 bits
Sample rate	800MHz
DFT input length	2^{24} samples
FFT compute time	2 ms
Channel count	2
Efficiency	99.765%

Table 2.5: Specifications for the custom, real time spectrum analyzer used for run 1A.

1165 After passing through and amplifier and filter chain outlined in Sec. 2.5.4, both the main
 1166 and veto antenna's RF signals are digitized by the ADQ32's two independent ADCs. This
 1167 raw, digitized time series is sampled at the digitizer's clock rate. Since the discrete Fourier
 1168 transform (DFT) of a perfect sinusoid sampled by an unstable clock will have a finite spectral
 1169 width, clock stability must be better than the expected spectral width of candidate signals,
 1170 which in our case is set by the expected $Q_{DP} \approx 10^6$. To achieve the required stability,
 1171 we synchronize the sample clock (Valon 5009 RF synthesizer) of our ADC to a 10 MHz
 1172 rubidium frequency standard (Stanford Research Systems FS725) which is further steered
 1173 by the one pulse-per-second (pps) signal from a GPS receiver. Clock performance is discussed
 1174 in Sec. 3.3.3.

1175 This system utilizes a GPU direct write in order to minimize CPU-GPU copies tends to
 1176 be significantly slower than the FFT itself. This GPU direct write is implemented by the digi-
 1177 tizer's C++ API which is called from python. This happens in the `teledyneTemplate/drDaq.py`
 1178 script (within the directory linked as a footnote at the beginning of this subsection). The
 1179 GPU is a Nvidia A5000. The process is shown graphically in Fig. 2.36

1180 First, several buffers are allocated in GPU memory. A record is acquired (2^{24} time domain

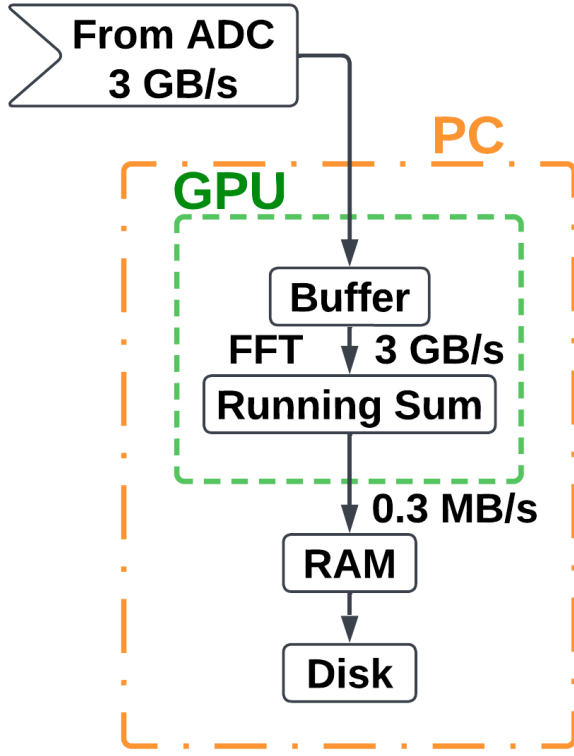


Figure 2.36: Real time DAQ data stream. Approximately 10^4 time series records (about 3 minutes of real time data) are written from the ADC directly to GPU buffers. FFTs are performed on these records resulting in a pre-averaged spectrum which can be saved to disk. This set up is duplicated for channels A and B, though the data rates indicate the sum of both channels.

1181 samples for run 1.4). This record is written to a pre-allocated, time-domain buffer in the
 1182 GPU's memory. Next, an FFT is performed using Pytorch which I found to be the fastest
 1183 algorithm, at least on a Nvidia GPU. 8,600 FFTs are performed and added to a cumulative
 1184 sum on the GPU (representing about 3 minutes of real time data). Dividing by the number of
 1185 FFTs provides an averaged spectrum that is saved for offline processing. This *pre-averaging*
 1186 reduces the raw $\approx 1.5 \text{ GB/s}/\text{channel}$ data stream to $\approx 0.15 \text{ MB/s}/\text{channel}$, which greatly
 1187 reduces storage requirements. However, this comes at the cost of temporal resolution of

1188 transient candidates. Since we are interested in constant (or at least very slowly varying)
1189 signals, this is not a problem, but in other radio astronomy applications, this step should be
1190 avoided. Pre-averaging is set using the NOF_BUFFERS_TO_RECEIVE variable, see Appendix A .

¹¹⁹¹ **Chapter 3**

¹¹⁹² **System Characterization and Data**

¹¹⁹³ **Acquisition System**

¹¹⁹⁴

“When you can measure what you are speaking about and express it in numbers you know something about it; but when you cannot measure it, when you cannot express it in numbers your knowledge is of meagre and unsatisfactory kind; it may be the beginning of knowledge but you have scarcely progressed in your thoughts to the stage of science whatever the matter may be.”

Lord Kelvin

1195 This chapter covers the characterization of the system as a whole, including the shielding
1196 room (Introduced in Sec. 2.5.1), amplifier chain (Sec. 2.5.4) and real time spectrum analyzer
1197 system (RTSA, Sec. 2.5.7). This section provides data and information about how they
1198 were collected from tests that were performed, but that distract from the narratives of the
1199 preceding and following chapters. This chapter can be skimmed and referenced with further
1200 care during the reading of Ch. 4.

1201 **3.1 Measurement of Amplifier Chain Performance**

1202 The amplifier chain conditions the analog signal (described in Sec. 2.5.4). The following data
1203 show some measurements that are useful in confirming the system is operating as expected.
1204 Before, during and after a new data run, similar data should be collected and inspected so
1205 that any degradation of performance can be monitored. At the very least, one should take
1206 note of the power spectrum from a room temperature terminator (Fig. 3.11) and monitor it
1207 for any changes. The heads-up display (Fig. A.1) makes this very easy.

1208 **3.1.1 Y-factor method¹**

1209 The Y-factor method [54] [55] is a common technique for measuring the gain and noise
1210 temperature of an amplifier chain (details in Sec. 2.1.4). A matched terminator is placed at
1211 the end of a transmission line, which is connected to the input of an amp chain under test.

¹Code for this section can be found at: <https://github.com/josephmlev/darkRadio/tree/master/daqAnalysisAndExperiments/run1p4/yFactorTest/yFactorTest.ipynb>

1212 The output of the amp chain is measured with the terminator at two different temperatures ².

1213 These temperatures must be known, and the larger the difference the better the measurement

1214 because it's easier to extrapolate the slope and intercept from these data (see Fig. 3.1).

1215 There are a few different ways to handle the algebra, but the simplest is to fit a line of

1216 the form

$$T_{\text{out}}(\nu) = G T_{\text{term}} + B, \quad (3.1)$$

1217 where all terms are dependent on frequency. The x-intercept (and therefore the negative

1218 amplifier temperature) than is simply G/B . This is shown as a cartoon for a single frequency

1219 in Fig. 3.1.

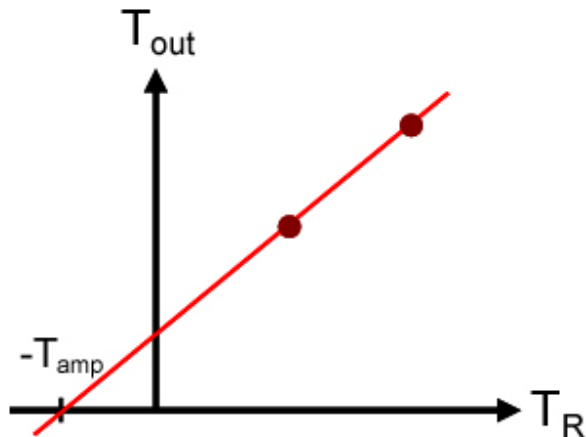


Figure 3.1: Cartoon showing Y-factor data. The (negative of) amplifier temperature is read off of the x-intercept. The gain is given by the slope. Figure from Wikipedia [56].

1220 To make this measurement, I wanted to use liquid nitrogen for the cold temperature

²Alternatively, a calibrated noise source can be used to simulate a very hot terminator, usually thousands of degrees Kelvin.

1221 (77 K) and a calibrated noise source for the hot temperature (\sim 12,000 K). The test was
1222 conducted using the noise source and used a 30 dB attenuator right before the ADC which
1223 was calibrated out later. However, while the test was set up to use this noise source, it gave
1224 unreliable results. I was able to confirm it became uncalibrated using a spectrum analyzer
1225 so I didn't use that data point. Additionally, I made the measurements with a much wider
1226 bandpass filter (0-1 GHz) compared to the span of this Run 1.4 (0-0.3 GHz) so that the same
1227 data would also give the gain and noise temperature up to 1 GHz (though this is not shown
1228 in this thesis). Both the 30 dB attenuator and the 0-1 GHz bandpass filter will be calibrated
1229 out. As a check this is done correctly, the gain is measured again using a tracking generator
1230 with the actual set up, avoiding corrections. This is shown in Fig 3.8. The two gain curves
1231 agree quite well.

1232 The test setup is nearly identical to the Run 1A amp chain (see Fig. 2.33). The differences
1233 are the 30 dB attenuator and band pass filter (discussed above) and the short, semi-rigid,
1234 cryogenic-capable cable between the terminator and LMR 400 cable. The cryogenic set up
1235 is shown in Fig. 3.2. The raw data (including only liquid nitrogen and room temperature)
1236 are shown in Fig. 3.3.

1237 The spectra of Fig. 3.3 contain hot and cold measurements at 2^{18} frequency points. At
1238 each point, a fit is performed according to Eq. 3.1. To demonstrate, this is shown for a single
1239 frequency (625 MHz) in Fig. 3.4.

1240 Finally, fitting the raw spectra shown in Fig. 3.3 with Eq. 3.1 at each of the frequency
1241 points, the frequency-dependent gain and noise temperature of the amp chain is extracted.
1242 These are shown (after correcting for the 30 dB attenuator) in Figs. 3.5 and 3.6.

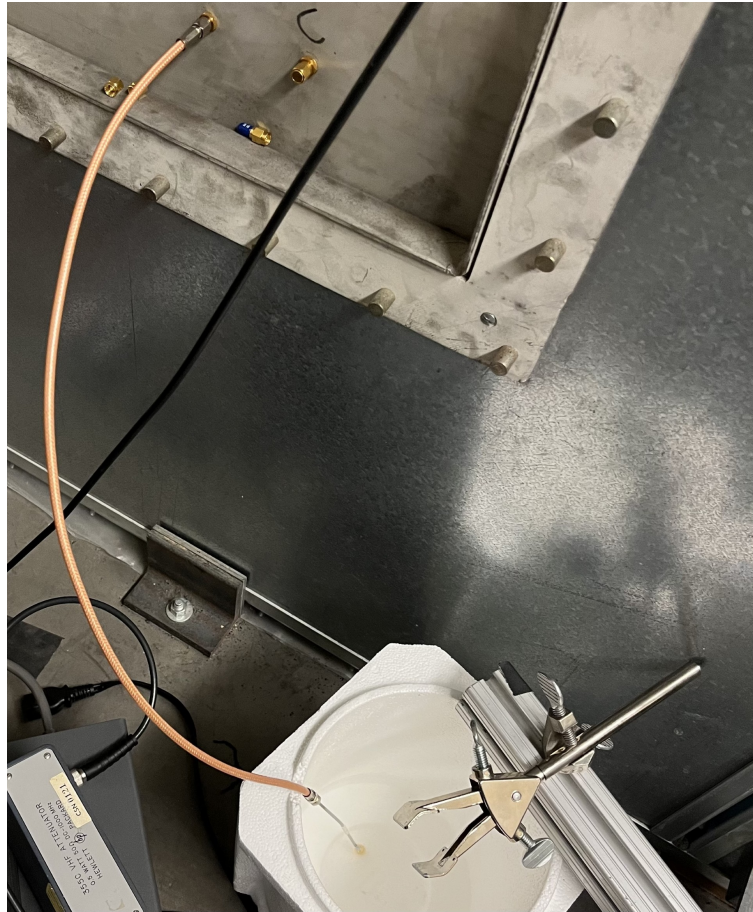


Figure 3.2: Cryogenic hardware setup for the Y-factor measurement. Also note that the terminator is a standard Pasternack 50Ω (with the blue rubber case removed) and the cable is semi-rigid and rated for cryogenic temperatures. This test load (semi-rigid cable plus terminator) were measured to have $S_{11} < -35\text{ dB}$ at both room temperature and at 77 K (by submerging in liquid nitrogen), confirming performance at cryogenic temperatures.

1243 As a final check, I took the Run 1.4 terminator data and corrected it for the gain and
1244 noise figure found using the Y-factor method of this section, expecting to recover the famous
1245 -174 dBm/Hz as predicted by Johnson's formula for a terminator at room temperature. The
1246 agreement is quite good and as shown in Fig. 3.7.

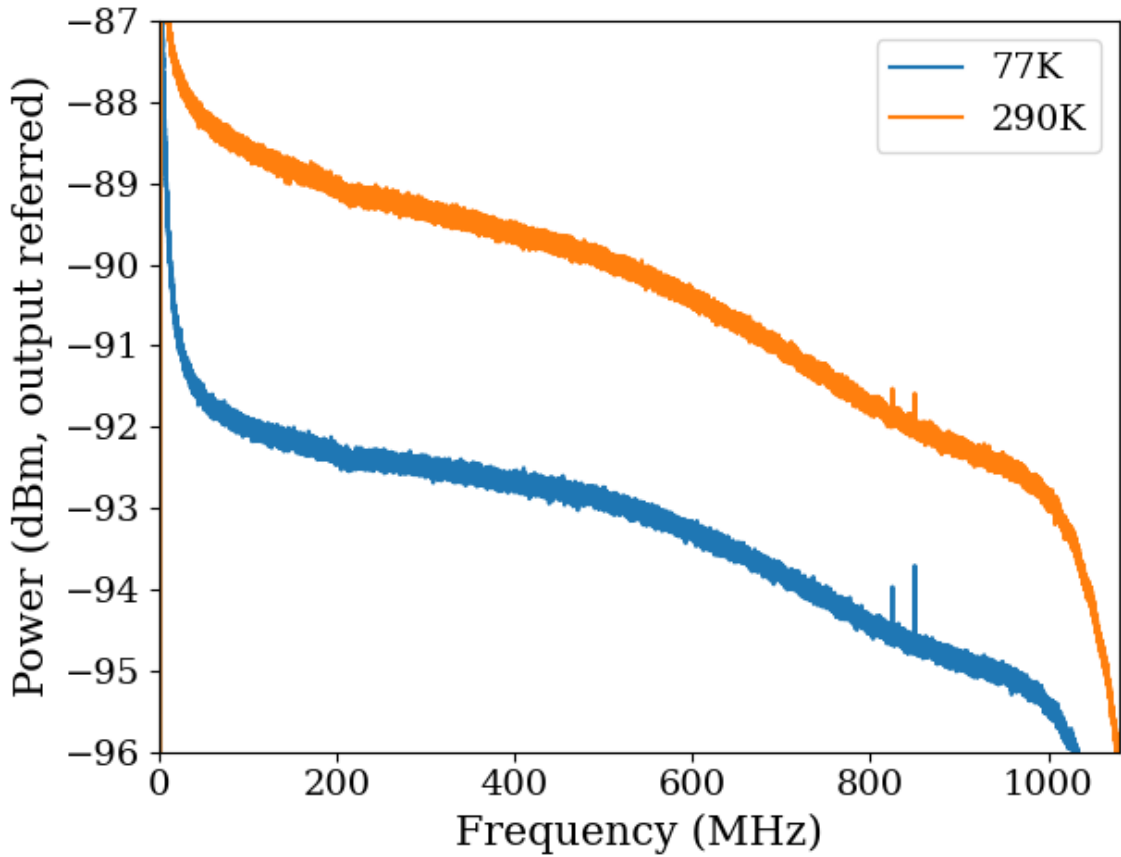


Figure 3.3: Raw output power spectra used to compute the gain and noise temperature for the Run 1.4 amp chain using the Y-factor method. $\Delta\nu_{\text{RF}} \approx 9.5 \text{ kHz}$, and 10,000 averages were taken. These data are only used to characterize the system between 50 and 300 MHz, so the low frequency ADC effects and RFI around 800 MHz do not affect the calculation. Note that the amp chain under test has a 30 dB attenuator directly before the ADC which is discussed in the text. This had an impact on the measured gain, and it is corrected for in the following analysis. It has negligible impact on the noise figure however, as shown in Eq. 2.29.

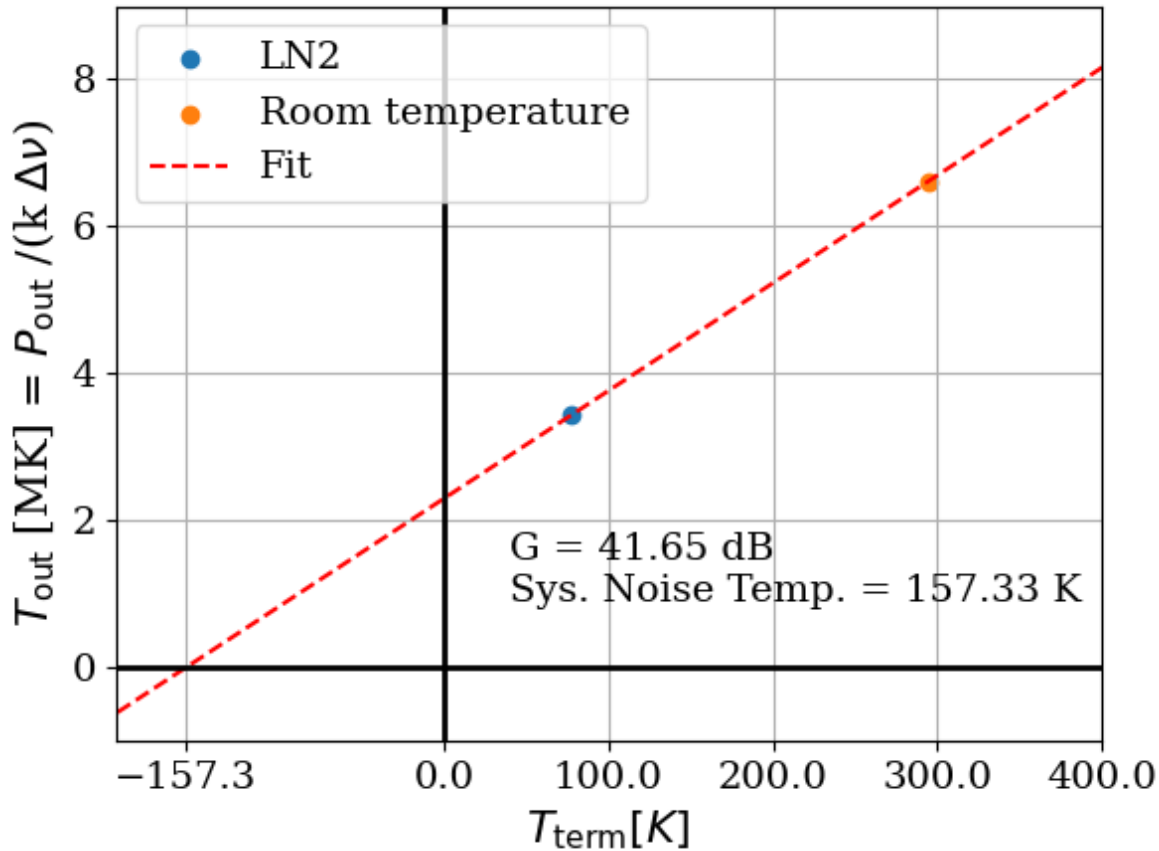


Figure 3.4: Y-factor data from Run 1.4 amp chain at a single frequency (625 MHz). Note that T_{out} is in MK or millions of degrees Kelvin. This is expected since there is approximately 41 dB of gain on an input temperature of a few hundred Kelvin. Reminder, there is a 30 dB attenuator which has not yet been corrected for.

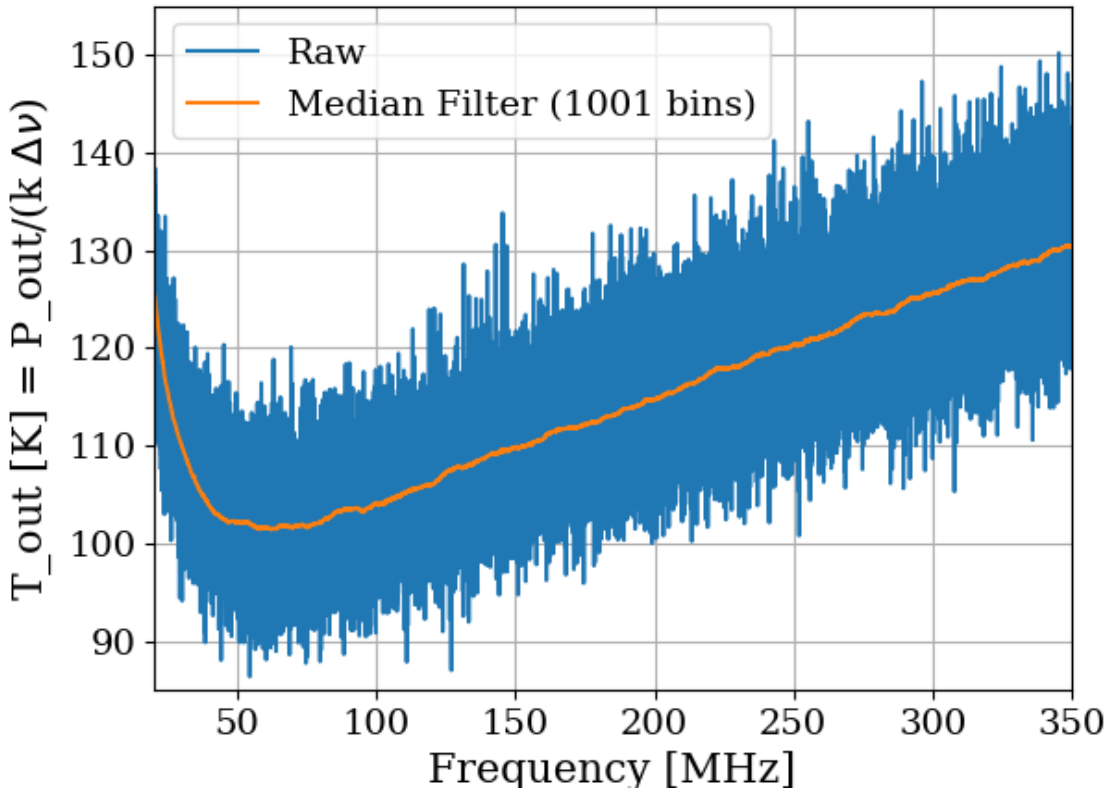


Figure 3.5: Frequency dependent noise temperature of the Run 1.4 amplifier chain, measured using the Y-factor method. Low frequency behavior is consistent with the data sheet of the LNA [33]. The increase at high frequency due to attenuation of the cable before the LNA. Future runs may wish to place the LNA directly on the antenna to minimize this issue, though other complications will be introduced. Median filter is simple rolling median to smooth out noisy measurement.

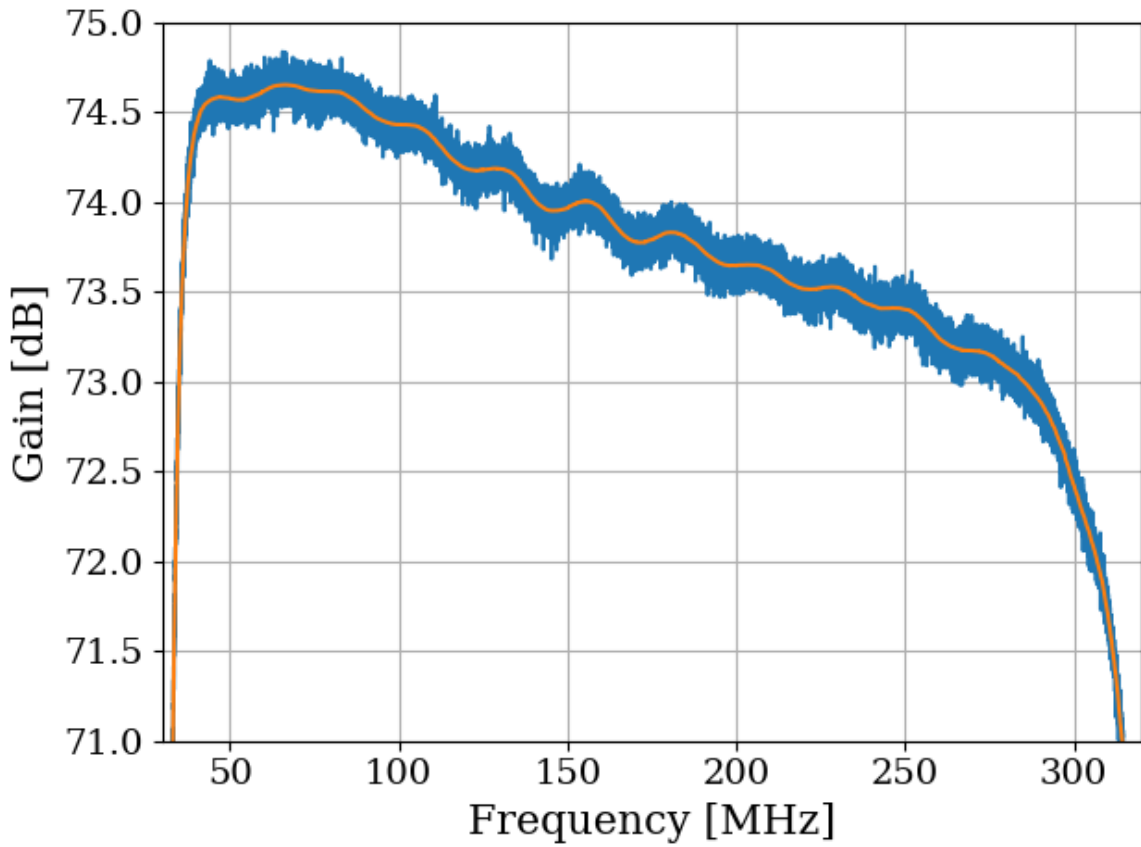


Figure 3.6: Frequency dependant gain of the Run 1.4 amplifier chain, measured using the Y-factor method. The 30 dB attenuator and band pass filter have been corrected for in this plot. The slow decrease of gain with frequency is consistent with the data sheets for the LNA [33] and secondary amplifier [48]. Roll-off at high and low frequencies is due to the bandpass filter (see 2.5.4.3). Bumpy behavior is due to the small impedance mismatch of the terminator to the 50Ω system.

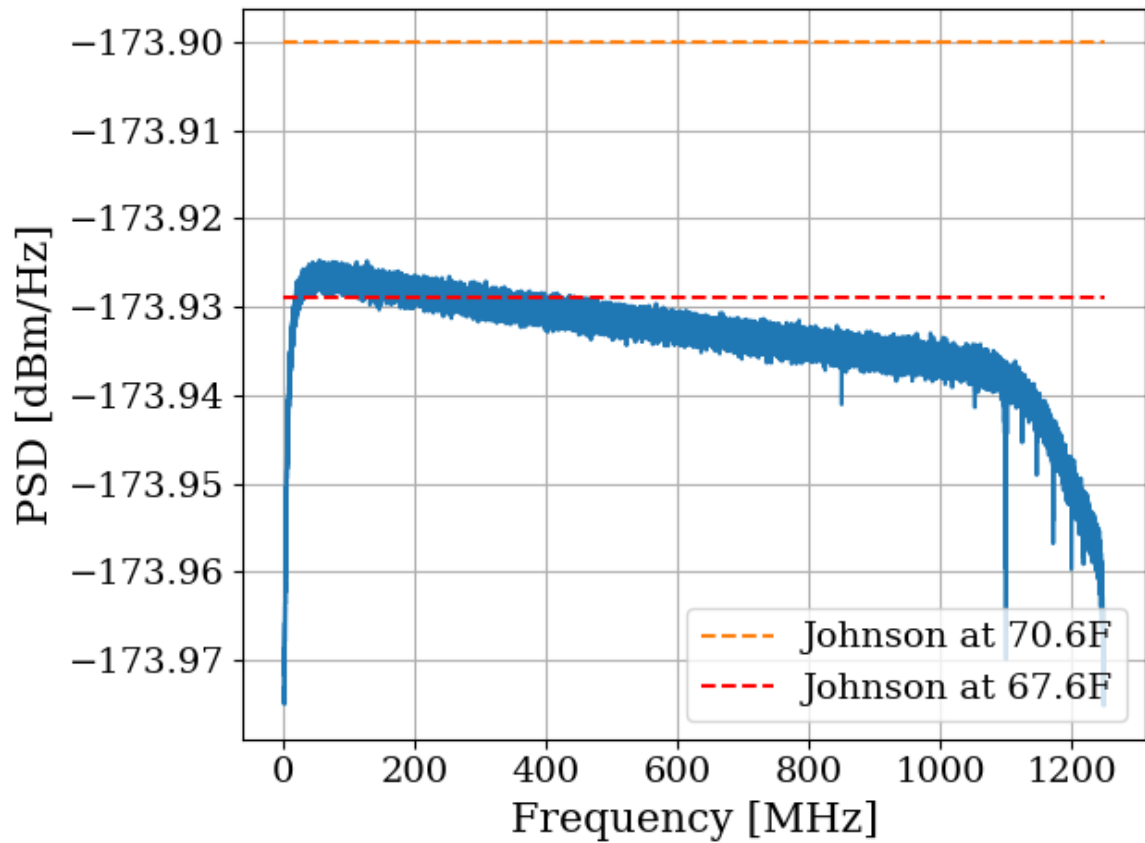


Figure 3.7: Run 1.4 terminator, input-referred power spectral density. Excellent agreement with the predicted value from the formula for Johnson noise at room temperature. Two reference temperatures are given with the dashed lines.

1247 3.1.2 Confirming gain with tracking generator measurement

1248 As a sanity check for the Y-factor method, the system gain was measured again using the
1249 tracking generator on the Rigol RSA-5065-TG [57], with good agreement. This measurement
1250 was useful since there were some corrections involved in the Y-factor measurement (the 30 dB
1251 attenuator and band pass filter).

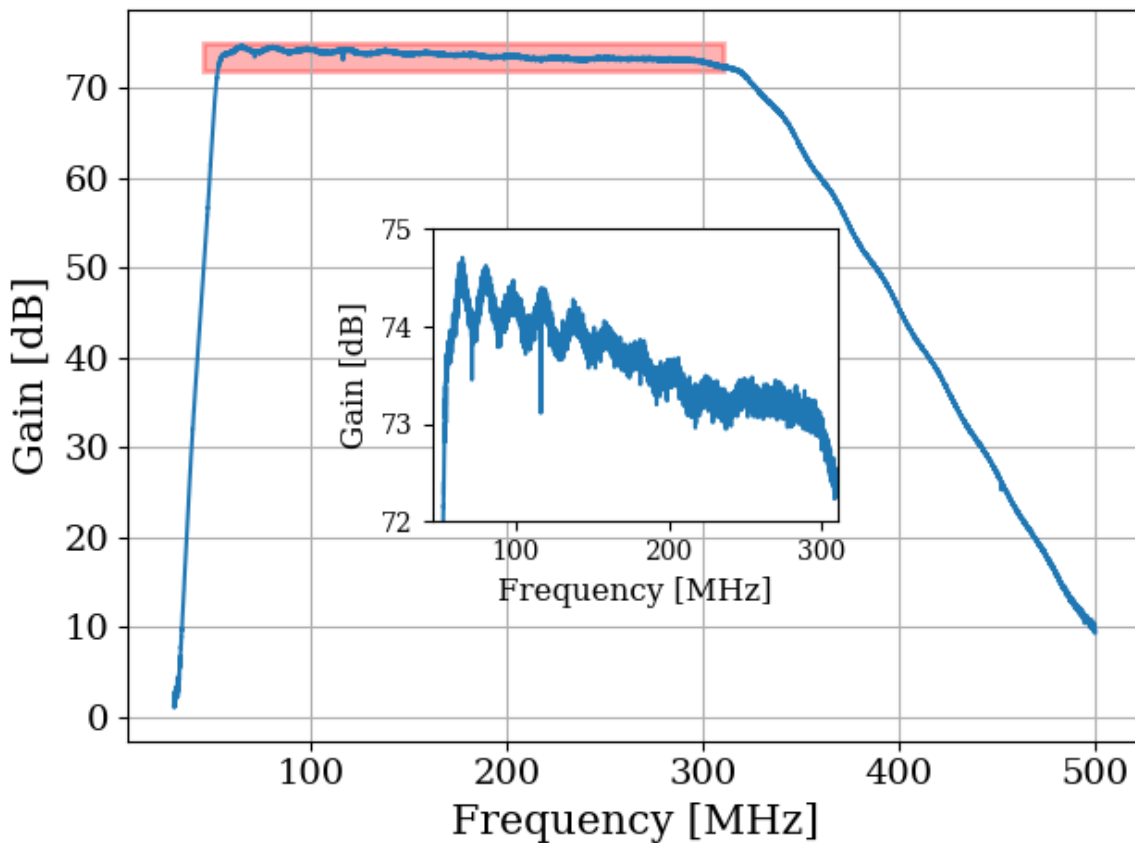


Figure 3.8: Gain vs. frequency of Run 1.4 amplifier chain, including LNA, secondary amplifier, bandpass filter and attenuators. Inset shows zoom of region enclosed in red box. Measured using tracking generator on Rigol RSA-5065-TG [57]. Wiggles visible in inset are a known artifact due to an impedance mismatch between the Rigol's tracking generator and the system under test. Gain was confirmed by comparing to Y-factor method (Sec. 3.1.1)

1252 **3.1.3 System stability over a run period** ³

1253 The system's gain will vary slightly over the course of a run. An obvious culprit is the
1254 battery voltage decreasing with time ⁴. At first glance, one may conclude that since the
1255 LNA is equipped with an internal voltage regulator, it is insensitive to the battery voltage
1256 as long as it is above some minimum value. However, at higher voltage, the regulator must
1257 dissipate more power which will make the LNA warmer and may have an effect on the gain
1258 of the LNA. Tests of gain vs. LNA voltage show that this is a minor issue. This is shown in
1259 Fig. 3.9.

1260 Knowing the gain vs voltage is only useful if it is understood how the battery voltage
1261 will behave over the course of the run. These data are shown in Fig. 3.10.

1262 As a final check of system performance during the run, Fig. 3.11 shows the output-referred
1263 power (averaged from 50-300 MHz) over the course of the 9-day Run 1.4. The gain varies by
1264 about 0.7%, an insignificant amount given the other uncertainties involved (especially that
1265 of simulation and calibration, Sec. 4.3).

³Code for this section can be found at: [https://github.com/josephmlev/darkRadio/tree/master/daqAnalysisAndExperiments/run1p4/run1p4_timeDependence.ipynb](https://github.com/josephmlev/darkRadio/tree/master/daqAnalysisAndExperiments/run1p4/run1p4_analysis/run1p4_timeDependence.ipynb)
https://github.com/josephmlev/darkRadio/tree/master/daqAnalysisAndExperiments/run1p4/gainAndNF/gainAndNF_analysis.ipynb

⁴only the LNA is powered by battery. The secondary amplifier is outside of the room and powered with a voltage regulator.

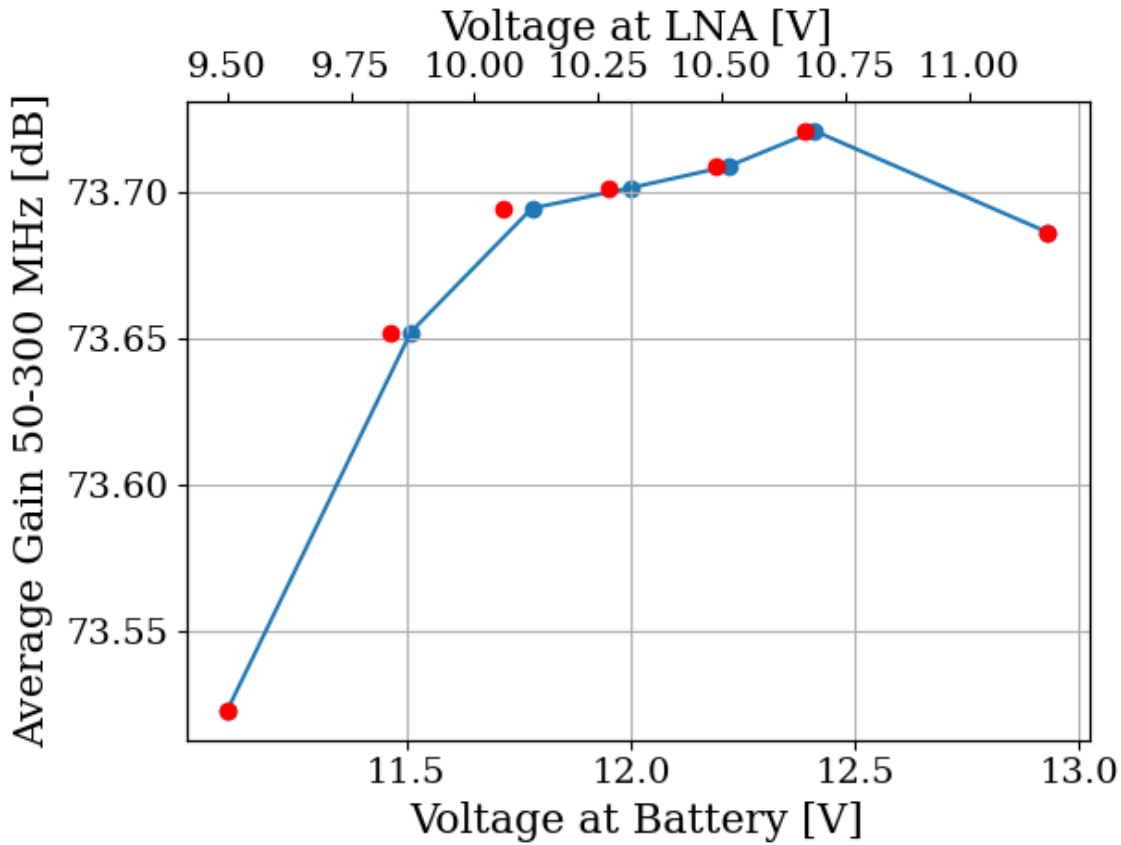


Figure 3.9: Gain vs. LNA voltage of Run 1.4 amplifier chain, including LNA, secondary amplifier, bandpass filter and attenuators. Measured using tracking generator on Rigol RSA 5065TG [57]. Gain is frequency dependent; its average value between 50 and 300 MHz is shown here. Voltage at amplifier was measured directly at terminals, after significant voltage drop due to interlock and slow turn on circuits (described in Sec. 2.5.6). Gain is in good agreement with the previous two subsections, 3.1.1 and 3.1.2. The operating voltage range specified on LNA data sheet [33] is 10-15 V. The voltage at the LNA (red) does not exactly line up with voltage at battery (blue), so there is a slight offset. x-axes scale have been set so that the maximum and minimum voltages line up.

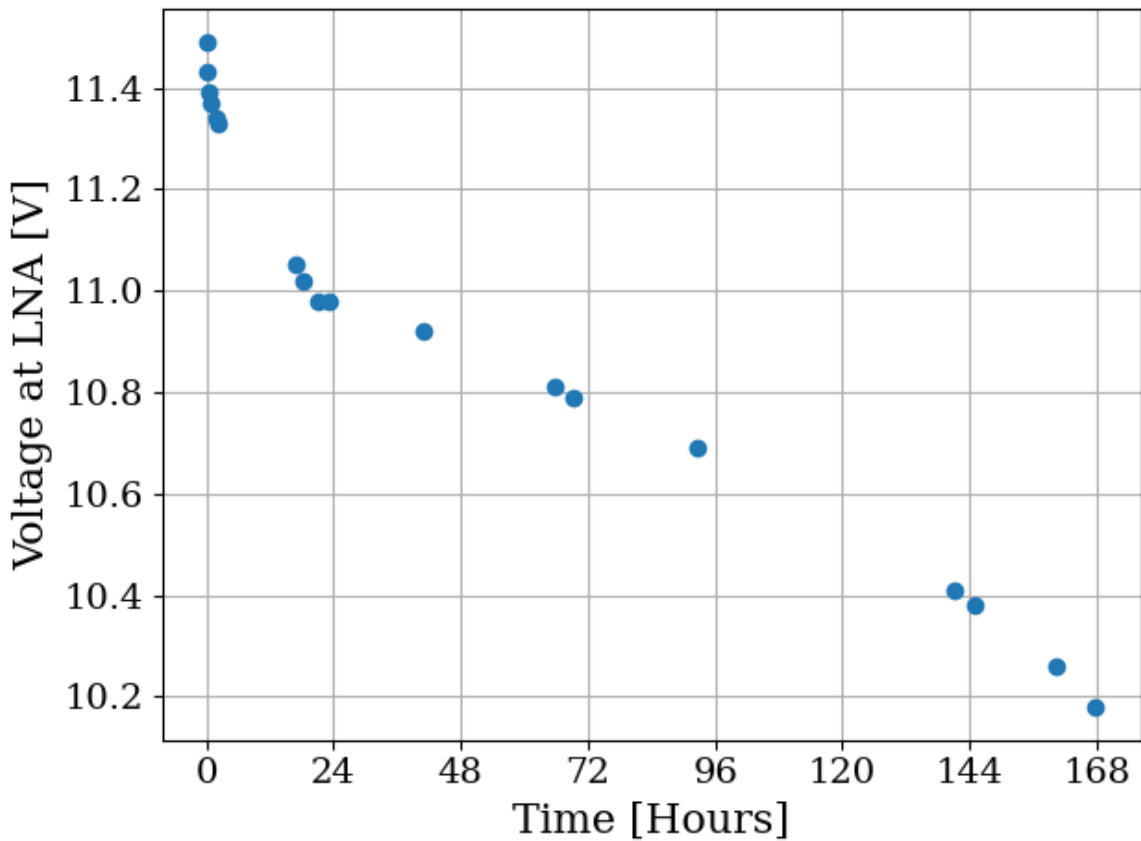


Figure 3.10: Voltage at LNA vs. time. Data were acquired 7/15/2024 through 7/22/2024 using battery number 2 immediately after being charged. The system was set up as it was for Run 1.4, including the switching cycle (on for 3 minutes, off for 45 minutes). The battery supplies 177 mA when the switch is off, and 370 mA when the switch is on. There is an additional data point (not shown) around 196 hours where the voltage has dropped to 6.2 V, well below the minimum required voltage. The battery had approximately 20 charge/recharge cycles at the time of this test and was about 14 months old. A repeat of this test may be required to use the battery for longer periods between charges.

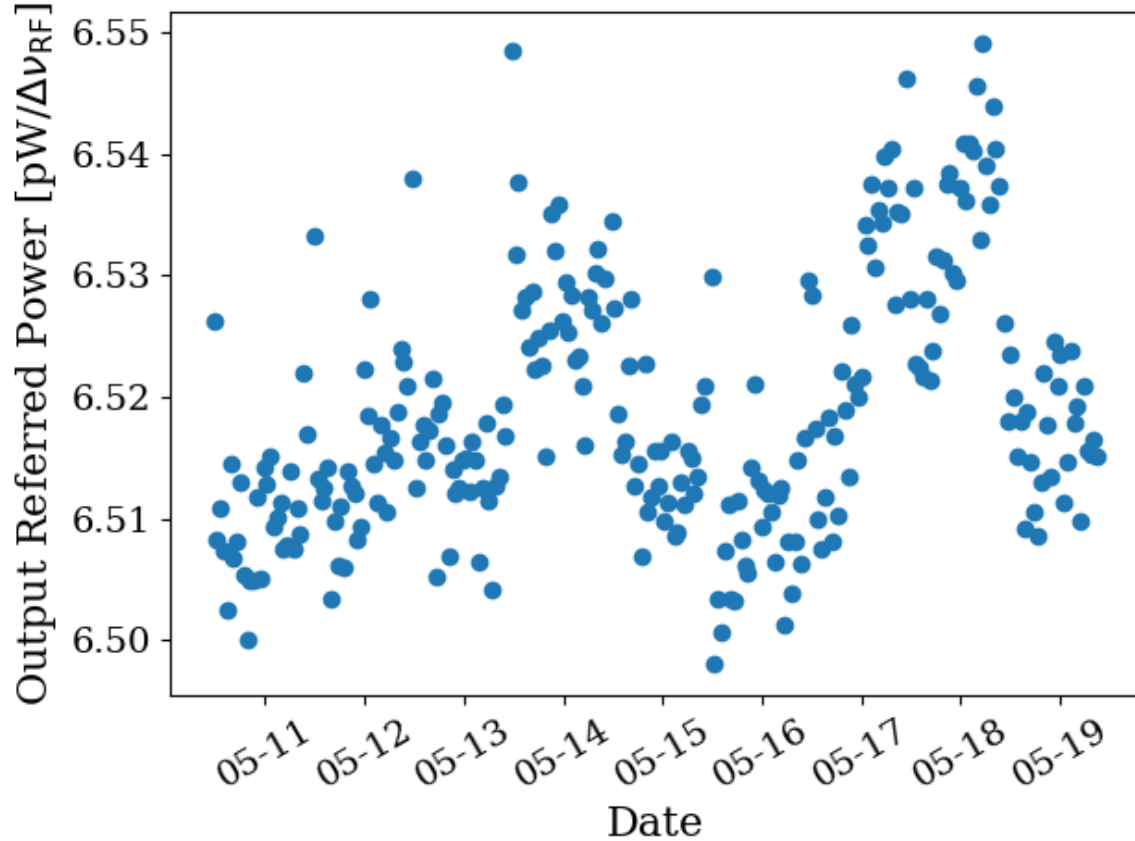


Figure 3.11: Frequency-averaged power vs. time of the terminator from Run 1.4 (schematic shown in Fig. 2.28). Each data point represents the mean power between 50 and 300 MHz of the terminator. In Run 1.4, a \sim 3 minute long scan of the terminator took place after \sim 45 minutes of antenna scans. Dates shown are all May 2023 (month-day format, year suppressed) and x-axis ticks are shown at midnight.

1266 **3.2 Measurement of shielding effectiveness and radio**
1267 **frequency interference**

1268 Shielding effectiveness (SE) and radio frequency interference (RFI) were introduced in Secs.
1269 2.1.3 and 2.5.1. Their measurement is introduced here.

1270 Similar to the warning given in the previous section, SE should be measured before
1271 starting a data run or after entering a new frequency range/modifying anything on the
1272 patch panel. In addition, it is best practice to clean the door before beginning a run (the
1273 procedure is described in the text of this section).

1274 Due to reciprocity between antennas, measuring the shielded room's ability to keep radi-
1275 ation *out* is equivalent to measuring how well the room can keep it *in*. The latter method is
1276 simpler and was performed. The IEEE standard prescribing a very detailed SE measurement
1277 procedure [58] was used as a rough guideline, but the simple results presented here should
1278 be viewed as an estimate. While simplified, the results do tend to agree with predictions of
1279 when RFI should become detectable, based on comparisons to the veto antenna spectrum ⁵.

1280 The SE was measured by placing a Rigol DSG830 signal generator inside the room,
1281 powered by the filtered 120 VAC Edison outlets inside the room, shown in Fig. 3.12. An
1282 antenna was connected to the signal generator. Outside of the room, an identical antenna
1283 was connected to a Rigol RSA-5065-TG spectrum analyzer [57]. The spectrum is scanned to
1284 find a frequency without local interference which would confuse the results. The spectrum

⁵Or at least they did agree before cleaning the door. With the excellent isolation values, no RFI was detected in Run 1.4.

1285 analyzer was set to attenuate its input to prevent clipping⁶, and the signal generator was set
1286 to output a sine wave at maximum power. The power measured on the spectrum analyzer
1287 is P_{open} in Eq. 2.39. The door was closed, attenuation removed and P_{closed} was measured.
1288 In some cases the SE was so high a signal was buried below the noise floor of the spectrum
1289 analyzer. These data are shown in red in Figs. 3.13 3.14 and should be interpreted as an
1290 upper limit on isolation, since the true value is lower (better).

1291 SE can drop off to less than 80 dB if the RF gasket around the door is not clean. Previous
1292 day-long test runs detected several hundred signals which originated from RFI emitted from
1293 the PC and several local radio stations. Cleaning was performed by scrubbing the copper
1294 gasket and steel mating surface with red Scotch-Brite using denatured alcohol as a lubricant
1295 ⁷. After two passes of polishing were complete, a layer of DeoxIT D100L liquid was added.
1296 Maintenance cleanings were performed using only DeoxIT D5 spray. These signals were not
1297 detected after the gasket was cleaned, which is consistent with calculations of Sec. 2.1.3

1298 The primary RFI in the 50-300 MHz span are from local radio broadcasts. The electric
1299 field of the strongest signals is $\sim 100 \mu\text{V}/\text{m}$ when measured in the lab. There are also many
1300 lower level peaks which span the entire frequency range, though are more pronounced in a
1301 few frequency bands (60-75 MHz, 130-140 MHz, and 270-290 MHz). These peaks come from
1302 the PC which is an integral part of the spectrum analyzer system, housing the ADC, so it
1303 can not be removed. Before the door was cleaned, many of these signals were detectable
1304 after a few hours of integration, but cleaning the door resulted in a clean spectrum for the

⁶The spectrum analyzer automatically calibrates the displayed spectrum to its internal attenuator and pre-amplifier. If external gain/attenuation are used, they must be accounted for manually.

⁷Alcohol fumes are nasty. Be careful to open the door and use a fan to blow in air from the hall. Take frequent breaks. Don't get dizzy while standing on a chair!



Figure 3.12: Photo showing setup to measure SE of 314. Photo taken using Vivaldi antennas for data shown in Fig. 3.14. The same setup was used with bicon antennas for the 50-300 MHz data shown in Fig. 3.13. The bicon antenna shown in the background of this photo was not used for this test.

1305 9-day data Run 1.4. The spectrum from the veto antenna (discussed in Sec. 2.5.5) is shown

1306 in Fig. 3.15

314 Shielding Effectiveness

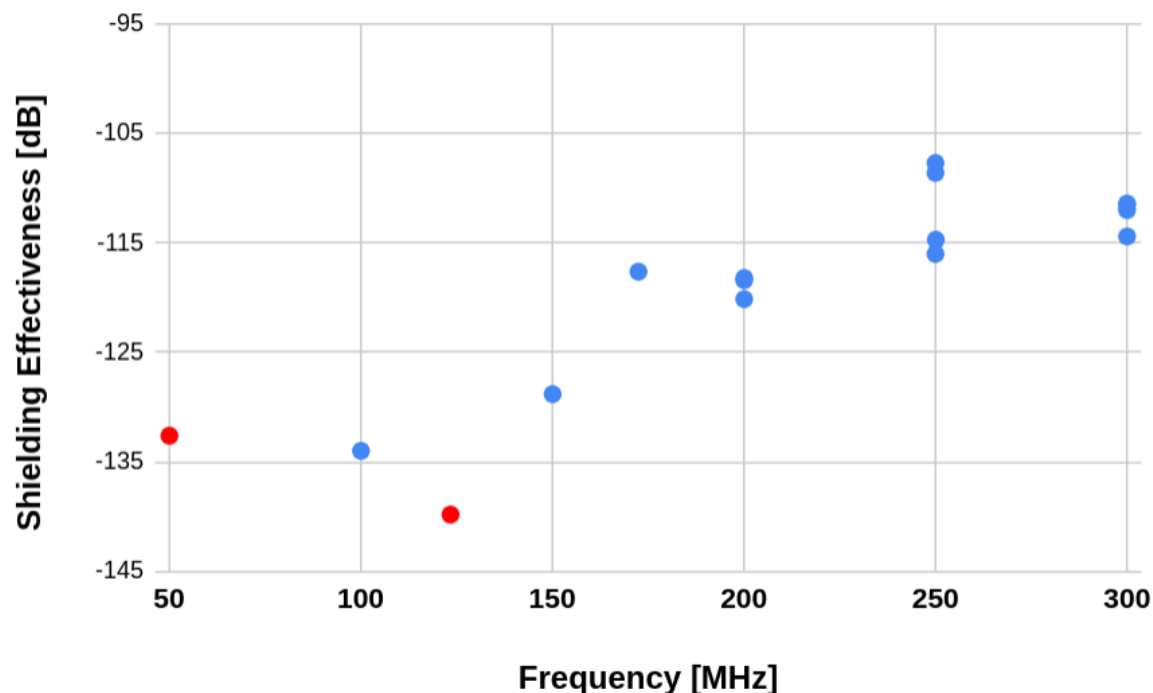


Figure 3.13: Shielding effectiveness of shielded room measured with bicon antenna. Red points indicate measurements limited by the noise floor of the spectrum analyzer located outside the shielded room and are an upper limit. The true SE is lower (better). To get the true SE for these points, measurement would require a stronger amplifier inside the room. SE measurements are all better than required for Run 1.4, and no RFI candidates were detected. At a few frequencies the antenna inside the room was moved to get a sense of the uncertainty of the measurement.

314 Shielding Effectiveness

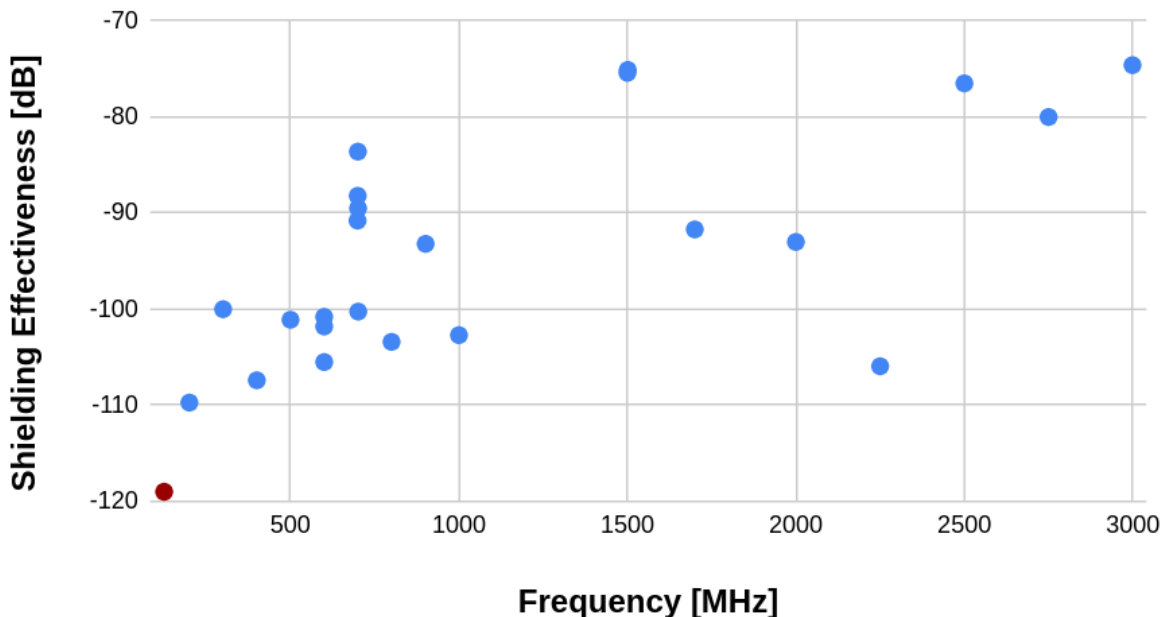


Figure 3.14: Shielding effectiveness of shielded room measured with Vivaldi antenna. Red points indicate measurements limited by the noise floor of the spectrum analyzer located outside and are an upper limit; true SE is lower (better). Measurement would require a stronger amplifier inside the room. At a few frequencies the antenna inside the room was moved to get a sense of the uncertainty of the measurement.

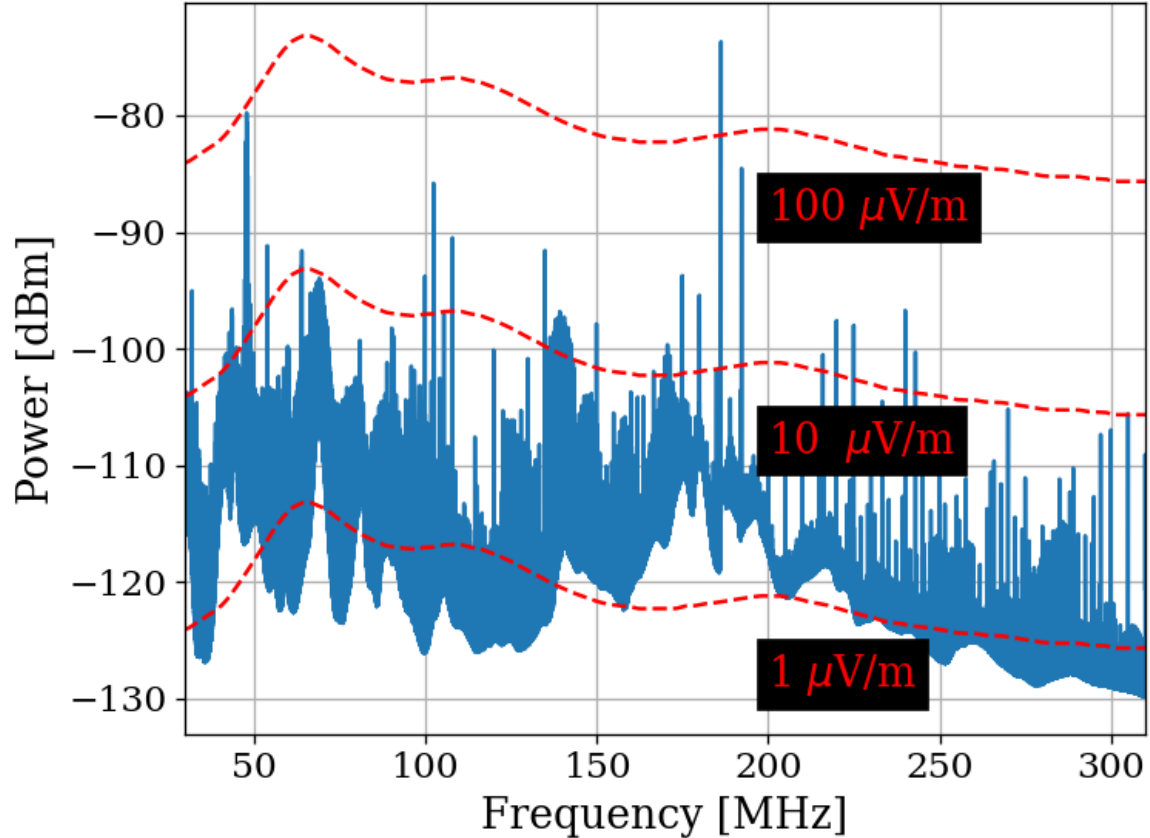


Figure 3.15: Spectrum from veto antenna during the 300 MHz data run. Spectrum plotted as measured power in dBm. Red curves indicate the equivalent field strength. These curves track the free-space antenna factor with frequency for the Com-Power AB900 [44] bicon. Two identical AB900-A antennas are used, one to search for dark photons in the shielded room, and a second to monitor the local RFI background.

1307 3.3 Spectrum Analyzer Characterization

1308 This section outlines several tests performed to ensure the GPU-based real time spectrum
1309 analyzer (RTSA) system performs as expected. Lots of background information that relates
1310 to this system is described in Sec. 2.5.7.

1311 3.3.1 Spectrum analyzer calibration

1312 The first step in determining if the RTSA system is working adequately is to make sure
1313 it is able to correctly identify known, injected signals and noise. This calibration step is
1314 important since the FFT is normalized manually (see Eq. 2.15), and it is rather easy to
1315 mess up. The test signals were generated with a Rigol DSG830 signal generator. The time-
1316 domain peak-to-peak voltage measured by the RTSA system agreed with the injected voltage
1317 to about 2 %. The signal generator's output frequency and power were verified in both the
1318 frequency and time domain using a separate oscilloscope and spectrum analyzer. This is an
1319 important step since cable losses are significant at this level of precision. They can be taken
1320 into account by consulting the data sheet for the cable⁸.

1321 Next, it is important to understand how the system handles noise spectra, since this is the
1322 primary use of the system. This is tested by amplifying the Johnson noise of a terminator
1323 (see Sec. 2.1.1.2) and measuring the power spectral density. Knowing the gain and noise
1324 figure of the amp chain allows for calibration using the procedure outlined in detail earlier
1325 in this chapter, see Sec. 3.1, specifically Fig. 3.7. These results were confirmed several times

⁸There are several cheap black SMA cables which are great for testing, but not for calibration. They have more than 5 dB of loss above 1 GHz. Use a nice cable for these tests, and blow out the SMA connector with compressed air while you are at it.

1326 preceding the data run. Note that due to windowing, other spectrum analyzers will disagree
1327 with the theoretical calculation by a few dB if the equivalent noise bandwith (ENBW) of
1328 the window function is not included. Also remember to take cable effects into account as
1329 discussed in the previous paragraph.

1330 3.3.2 Spurious signal performance of the ADC

1331 Any practical spectrum analyzer will have small, coherent, signals which sneak into the the
1332 analog signal path and, after being digitized and Fourier transformed, manifest as spurious
1333 signals or *spurs* (see Sec. 2.1.5.1). These spurs likely come from clock signals within the same
1334 enclosure as the ADC. They can also come from local oscillators bleeding through mixers in
1335 a mixed, high frequency system such as the Rigol RSA 5065TG [57] or the future, upgraded
1336 dark radio system discussed in Ch. 5.

1337 Regardless of their origin, the spurs must be characterized such that if a known spur is
1338 detected it can be classified as such and rejected quickly. Ideally, the system has enough
1339 gain that any spurs are subdominant to the amplified thermal noise, as discussed in Eq. 2.1.
1340 However, since there is a maximum amount of gain that can be added before clipping the
1341 ADC (see Sec. 2.5.4.3, this is not always possible.

1342 Experience with the Teledyne RTSA system has shown that spurs are rather simple to
1343 classify because they do not change much with time in either frequency or amplitude. Their
1344 frequency drifts by ~ 1 kHz and their amplitude changes by a few dB but this does not matter
1345 much.

1346 To classify them, the input of the Teledyne is terminated and a scan is performed few
 1347 minutes using the exact same system configuration as for the run (with the possible exception
 1348 of the number of averages). See Appendix A for details. The averaged, spectrum of the
 1349 terminated inputs are is shown in Fig. 3.16.

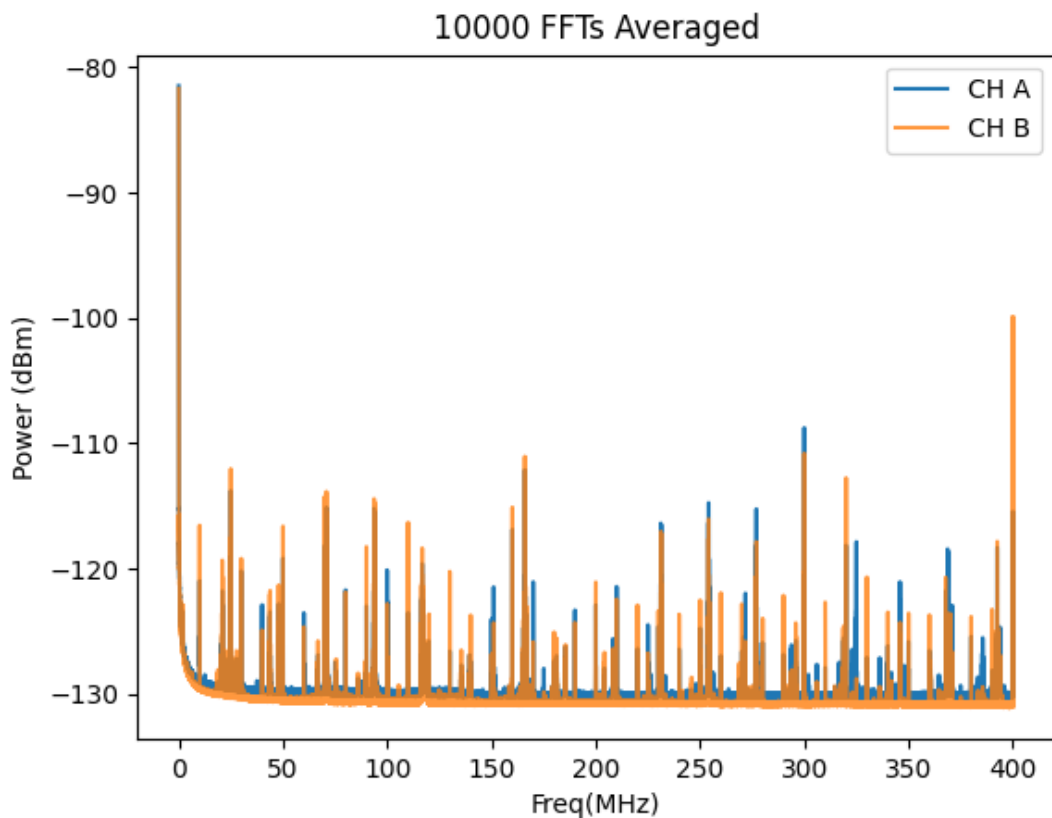


Figure 3.16: Scan of terminated input of Teledyne spectrum analyzer system to measure spur performance. Spectrum acquired with run 1A parameters ($\Delta\nu_{RF} = 47.7$ Hz) with 10,000 averages (~ 3.5 minutes). Plot taken directly from test mode of the system (not post-processed in any way). The largest spur in the 50-300 MHz range is at 299.97 MHz and is also the single significant signal in Run 1.4 (see Sec. 4.2.5).

1350 Once a test scan is acquired, comparing the largest spurs (≈ -110 dB) to the expected
 1351 output-referred background ([Johnson noise + LNA noise] * Gain ≈ -81 dBm/ $\Delta\nu_{RF}$) allows

1352 the calculation of the number of averages which are required before the spurs are significant.
1353 Working this out is a good test of understanding of Sec. 2.2. This spur should be detectable
1354 with 95% confidence after about 4 days, which is exactly what happened in Run 1.4. The
1355 false positive candidate is described in Sec. 4.2.5.

1356 3.3.3 ADC clock performance

1357 Any ADC requires a clock which dictates the precise time a sample should be acquired. This
1358 subsection deals with the evaluation of the performance of that clock.

1359 Determining the performance of a clock generally relies on having a better (read: more
1360 expensive) clock known as a *standard* and measuring the clock under test against the stan-
1361 dard. The Valon 5009 RF synthesizer was tested against a rubidium frequency standard and
1362 was found to be just on the threshold of stable enough to work (this threshold is explained in
1363 Sec. 2.5.7). To ensure the measurement is not limited by clock instability, the sample clock
1364 of the ADC is synchronized to a 10 MHz rubidium frequency standard (Stanford Research
1365 Systems FS725) which is further steered by the one pulse-per-second (pps) signal from a
1366 GPS receiver. This system has medium and long term fractional frequency stability (Allan
1367 deviation [59, 60]) of $\sigma_y(\tau) < 3 \times 10^{-12}$ (where τ is the averaging time) and phase noise of
1368 less than -65 dBc/Hz at offset frequencies > 50 Hz from the carrier [61]. This means that
1369 over the course of a single acquisition, the power contained in a bin will spread to an adjacent
1370 bin by less than 1 part in 10^6 which is more than sufficient for our experiment.

1371 This is a rare example of something in this experiment where we trust the data sheet.

1372 We do not have access to a clock which is better than this, so confirming its performance
1373 is difficult. Furthermore, even if the specs are an order of magnitude worse than advertised
1374 there is still more than enough stability for the experiment. This statement holds at higher
1375 frequencies. Since the Q of the signal is fixed, higher frequencies have wider bins so the
1376 relevant offset frequency at which the phase noise is measured increases with frequency. The
1377 dimensionless Allan deviation is also not affected.

1378 **3.3.4 Real-time data collection efficiency**

1379 As a final test, one would like to know how efficient data scans can be acquired and averaged.
1380 We call a 100 % efficient system *real time* as described in Sec. 2.5.7. Figure 3.17 illustrates
1381 this efficiency. For Run 1.4, it is $\sim 99.765\%$. However, in practice run logistics such as moving
1382 the antenna prevent the full efficiency of the system from being realized.

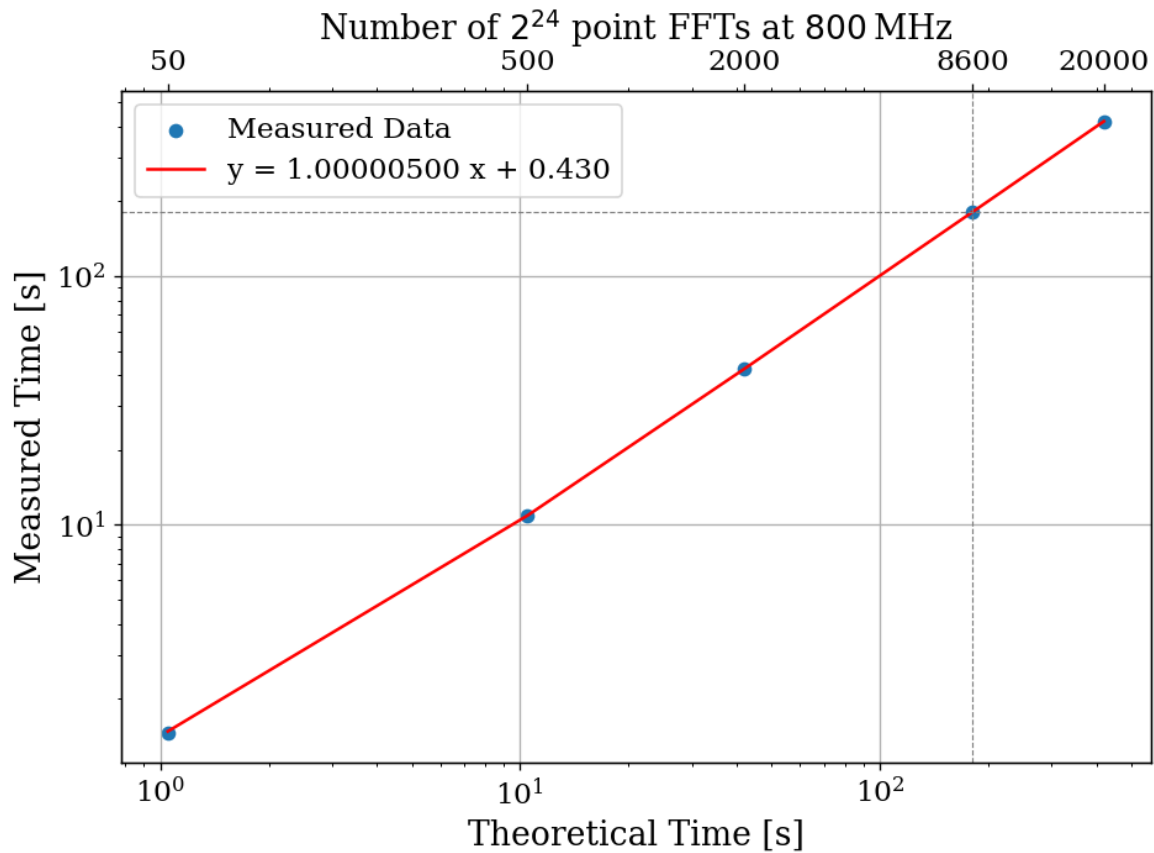


Figure 3.17: Acquisition efficiency for GPU-based real-time spectrum analyzer computed from measured vs. theoretical times. The constant offset of 0.43 s corresponds to a small set up period when starting an acquisition containing, in the case of run 1A, 8600 FFTs. In the limit of an infinite length acquisition, the system's efficiency is off from the slope and is 99.9995%. The more realistic efficiency is a function of number of FFTs per acquisition and for Run 1.4 = $180.3551 \text{ [s]} / 180.7782 \text{ [s]} = 99.765\%$.

₁₃₈₃ Chapter 4

₁₃₈₄ Data Acquisition, Data Analysis and
₁₃₈₅ Calibration

1386 Thus far this thesis has focused on building up a background on the dark radio technique
1387 as well as the design and testing of the experiment and it's sub-systems. This chapter outlines
1388 the process of acquiring actual data, analyzing that data to search for a small power excess,
1389 and in the absence of that excess, converting the null result into a exclusion limit on the dark
1390 photon mass/epsilon parameter space. Section 4.4 covers an injection test which confirms
1391 the experiment's ability to integrate all of the machinery developed and detect a realistic,
1392 hardware-injected dark photon proxy-signal. This chapter borrows heavily from my paper,
1393 New Limit on Dark Photon Kinetic Mixing in the 0.2-1.2 μeV Mass Range From the Dark
1394 E-Field Radio Experiment[36], which was published August 2024.

1395 I feel the cleanest way to mentally model the contents of this chapter is by compartmentalizing the first steps outlined above. For this reason, the chapter is organized as follows.
1396
1397 In Sec. 4.1 the data are acquired over a 9-day period. The procedure is outlined, and where
1398 appropriate references to previous sections are provided which are helpful in understanding
1399 how different procedures were developed. This section concluded with the output-referred
1400 power spectral density, S_o which must be searched for a power excess. We call this search
1401 *analysis* and it is covered in Sec. 4.2. The task of analysis is to extract a dark photon signal
1402 from this spectrum if it is present. Otherwise, in its absence, we would like to set a limit on
1403 the amount of output-referred power one would be able to detect *most of the time* were a
1404 narrow signal to be present in this averaged dataset. We quantify the meaning of “most of
1405 the time” by conducting a series of Monte Carlo “pseudo-experiments” on artificial signal-
1406 containing spectra for synthetic signals of varying powers and frequencies. With a limit on
1407 dark photon power extracted, Sec. 4.3 works back through the system to revolve a limit

1408 on epsilon above which we have some confidence we would have observed a signal. This
1409 produces the exclusion limit, which is ultimately the deliverable of this experiment. This
1410 limit is shown in Sec. 4.5.

1411 4.1 Data Acquisition

1412 Data were collected during a 9-day run from May 10 to May 19, 2023. This data run is
1413 referred to as run 1.4 throughout this thesis, and its details are shown in Table ??.

Specification	Value
Analysis span	50-300 MHz
Antenna	AB-900A biconical antenna
RTSA	Teledyne GPU system (Sec. 2.5.7)
Frequency resolution ($\Delta\nu_{RF}$)	47.7 Hz
Length of record	2^{24}
Sample rate	800 MHz
Window type	None (flattop)
Acquisition time per spectrum	20.96 ms
Run start time	2023-05-10 11:29:48
Total time of run	8 days, 21.13 hours
Efficacy (Time spent scanning antenna/total time)	92.03%

Table 4.1: Run 1.4 Details. Many specifications are related and can be computed from each other but are listed for reference. Efficacy differs from calculation in Fig. 3.17 mainly because of switching to terminator and brief daily pauses to move the antenna.

1414 Each day was subdivided into data-collection (23 hours 15 minutes) and setup (45 min-
1415 utes) periods. The setup period includes moving the antenna, changing a 12 V battery for
1416 the LNA (Sec. 2.5.6), file management and documentation. In order to reduce the data
1417 rate and storage requirements, all data were pre-averaged into 3-minute chunks and then

1418 saved. This pre-averaging is shown in Fig. 2.36. Additionally, an RF switch (see Fig. 2.28)
1419 is actuated for a 3 minute scan for every 15 antenna scans in order to monitor the status
1420 of the amplifier chain. For the data analysis, all 9 days of data were averaged together to
1421 create a single spectrum S_o (Fig. 4.1). If candidates are found, their time dependence can
1422 be observed by looking at the 3-minute pre-averages. All further analysis is performed on
1423 the full 9-day S_o spectrum and is described below (Sec. 4.2).

1424 4.1.1 Raw data, S_o

1425 All 9 days of pre-averaged data from the run are averaged together. The stability of the
1426 sample clock (Sec. 3.3.3) ensures that this is a simple process; frequency bins ($\Delta\nu_{RF} =$
1427 47.7 Hz) corresponding to a given frequency are added and normalized to the total number
1428 of pre-averaged spectra. This process produces the raw spectrum, S_o (Fig. 4.1), on which
1429 we will perform a search for power excess.

1430 Inspection of S_o reveals small power variations over spans of tens of kHz. The origin of
1431 these variations is explored in Sec. 2.3, but it is summarized here. Given an antenna in a
1432 cavity in thermal equilibrium with the input of an LNA, whose input is assumed to be real
1433 and matched, one would expect an output PSD which is constant with respect to frequency
1434 up to small variations in LNA gain. The theory for this is outlined by Dicke in [62]. These
1435 variations are not noise; for a given antenna position we repeatedly measure the same shape
1436 (though the noise riding on these variations *is* random). The origin of the observed small
1437 variations lies in the effective temperature difference between the room and LNA causing a

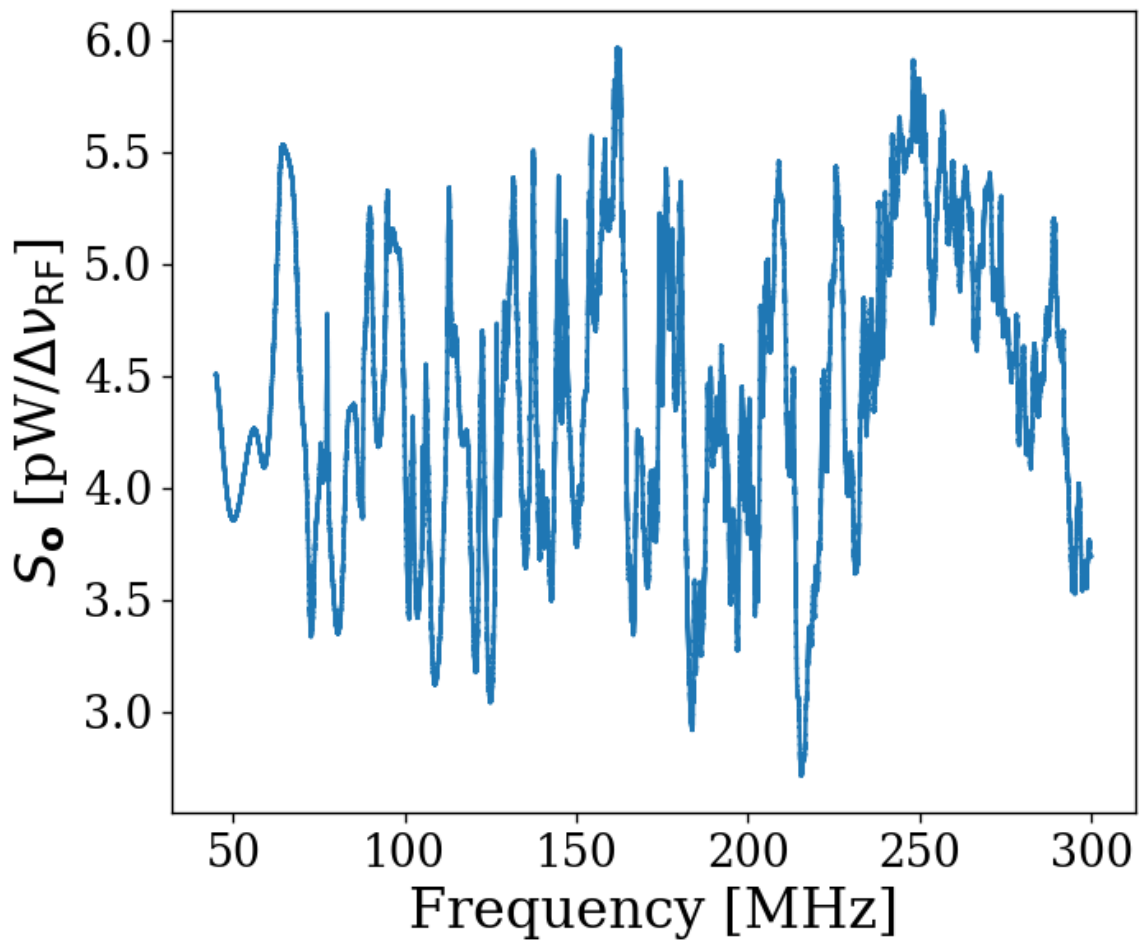


Figure 4.1: Run 1A averaged, output-referred antenna power spectrum S_o . Data were taken over a 9 day period at 9 antenna positions. The narrow variations are mainly due to the effective temperature difference between the room and LNA (Sec. 2.3), though there is a small contribution due to amplifier gain and noise temperature variations (Sec. 4.1.1). The variations seen here are not noise; their shape is repeatable for a given antenna position. The noise on this background is not visible at this level of zoom, but can be seen in Fig. 4.4, which shows a zoomed-in view of the spectrum at 240 MHz. The noise can also be seen nicely in Fig. 4.17



Figure 4.2: Run 1A averaged, output-referred, antenna and terminator power spectra

1438 net power flow from the antenna into the LNA. This effective temperature difference partially
1439 excites modes of the antenna/cavity system, causing the observed variations. We suspect this
1440 effect originates from a small reactive component of the LNA's input causing the electronic
1441 cooling described originally by Radeka [16]. This effect can be eliminated by adding an

1442 isolator between the antenna and LNA [29, 63] though for our experiment, it is impractical
1443 to get an isolator that covers such a wide band at relatively low frequency. Furthermore, the
1444 relatively wide (tens of kHz) variations can be handled by fitting to them which we discuss
1445 in Sec. 4.1.

1446 4.2 Data Analysis

1447 At this point, we have compiled a single, averaged, output-referred power spectrum, S_o
1448 (Fig. 4.1). The task of *analysis* is to extract a dark photon signal from this spectrum if
1449 it is present. Otherwise, in its absence, we would like to set a limit on the amount of
1450 output-referred power one would be able to detect *most of the time* were a narrow signal
1451 to be present in this averaged dataset. We quantify the meaning of “most of the time”
1452 by conducting a series of Monte Carlo “pseudo-experiments” on artificial signal-containing
1453 spectra for synthetic signals of varying powers and frequencies. The following subsections
1454 are organized as follows:

1455 4.2.1: Fit S_o to extract an estimate of the background B (which we call \hat{B}) whose origin was
1456 discussed in Sec. 4.1.1. See Fig. 4.4.

1457 4.2.2 Divide the spectrum by \hat{B} to generate the *normalized spectrum*, which very nearly
1458 follows a Gaussian distribution. Discuss statistics of the normalized spectrum and
1459 choose a global significance level and its associated *significance threshold*. See Fig. 4.5.
1460 Also note this was derived in Sec. 2.2.

1461 4.2.3 Apply a matched filter to the normalized spectrum and establish a significance thresh-

1462 old on its output using the same method defined in the previous section. See Fig. 4.6.

1463 The previous three steps comprise our *detection algorithm* which is shown in Fig. 4.3.

1464 4.2.4 Perform a Monte Carlo analysis to simulate the required power of a signal that can be

1465 detected above the significance threshold 95% of the time. We use this to recover a

1466 95% exclusion limit on the output referred power spectrum.

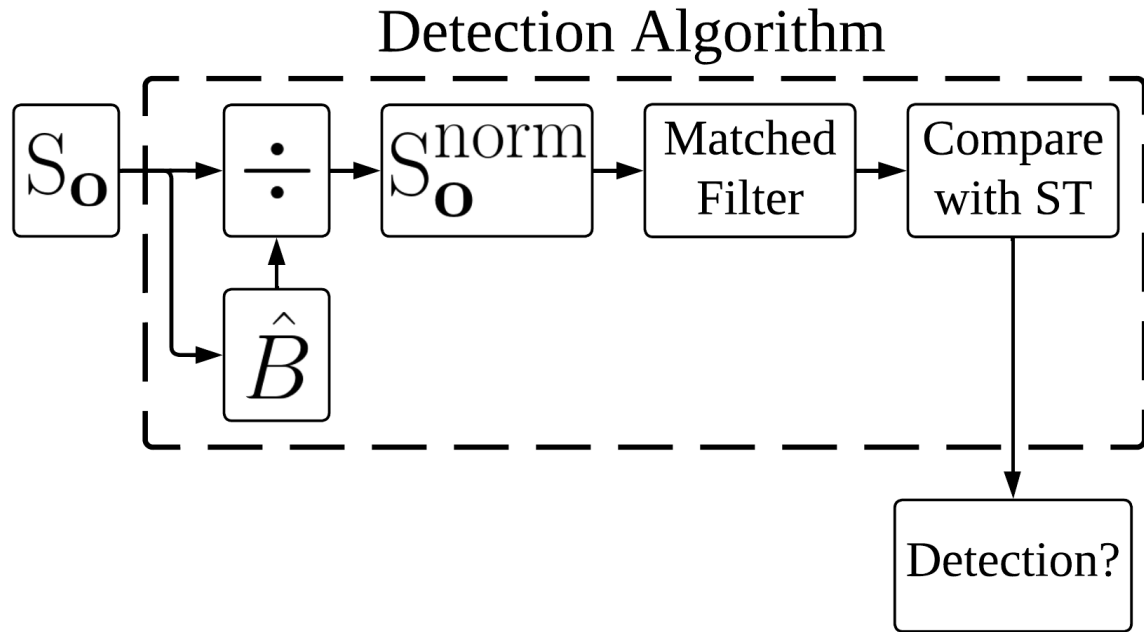


Figure 4.3: Flow chart outlining the logic of signal processing in the detection algorithm of sections 4.2.1 through 4.2.3. \hat{B} is the smoothed fit to S_o generated by low pass filtering. The output, *Detection?*, is a Boolean array which signifies a detection or lack thereof at each frequency bin. We detect a candidate if a bin contains more power than a significance threshold (ST) (Sec. 4.2.2).

1467 In Sec. 4.3 we convert this threshold on S_o into an actual limit on ϵ .

1468 Throughout the figures of this section we will follow a relatively large (40 fW, output-
1469 referred) software-injected, synthetic dark photon signal at 240 MHz to illustrate what a
1470 candidate would look like as it passes through the analysis procedure. This signal is added
1471 to S_o . For clarity, a single interfering candidate had been removed. This is discussed in
1472 Sec. 4.2.5.

1473 As a final note, at this point if you are unfamiliar with the data analysis, it would be
1474 advantageous to spend a few minutes looking through Figs. 4.17 through 4.19 to get a sense
1475 of the task at hand. It can be disorienting dealing with a spectrum that contains 8 million
1476 frequency points, zooming in on a signal can be very informative.

1477 4.2.1 Fit background, $\hat{B}(\nu)$ ¹

1478 As shown in Fig. 4.1, the measured power spectrum looks like flat thermal noise *multiplied* by
1479 some frequency dependent background, $B(\nu)$ ². However, for this section we will not concern
1480 ourselves with the origin of B or any details of the experiment aside from two assumptions:

- 1481 1. The measured background is the product of a normally distributed spectrum and some
1482 background. This is enforced by the central limit theorem due to the large number of
1483 averaged spectra, independent of any experimental specifics.
- 1484 2. The line shape of the signal is known and the width of this signal is much narrower
1485 than the width of features on the background, viz. $\Delta\nu_{DP} \ll \Delta\nu_B$

¹Code for this section can be found at: https://github.com/josephmlev/darkRadio/tree/master/daqAnalysisAndExperiments/run1p4/run1p4_analysis/analysisClass.ipynb

²When I was first working on this, I used $H(\nu)$ to represent this background. This naming convention persists in the analysis code.

1486 The first assumption (1) implies that if we were able to extract the background, dividing
1487 S_o by this extracted background would yield a *dimensionless*, normally distributed power
1488 spectral density on which to perform a search for a dimensionless signal. The second as-
1489 sumption (2) will be critical in both performing the fit to the background (this section), and
1490 performing matched filtering (Sec. 4.2.3).

1491 In light of these assumptions, we attempt to fit for the background power spectrum. Since
1492 this fit estimates B , we use the symbol \hat{B} to refer to it. As discussed in [17], a particularly
1493 effective fitting technique that can discriminate between the wide bumps of S_o and a narrow
1494 signal is to use a low pass filter. We implement this filter in two stages:

- 1495 1. A median pre-filter (51 bins or about 2.4 kHz wide) attenuates any very narrow, very
1496 large excursions which would interfere with any following filters, causing them to
1497 “ring”³
- 1498 2. A 6th-order Butterworth low pass filter (corner frequency of 210 bins or 10 kHz)

1499 These bin widths/frequencies should be interpreted as the width of spectral features on
1500 S_o that are attenuated and will, therefore, not show up in the background fit. A narrow
1501 zoom of this fit with a synthetic signal is shown in orange in Fig. 4.4.

³I recommend that this pre-filtering step is omitted if the spectrum analyzer in use doesn’t produce large spurs. It is the slowest part of the analysis chain. It also causes the filtered spectrum to deviate slightly from Gaussian.

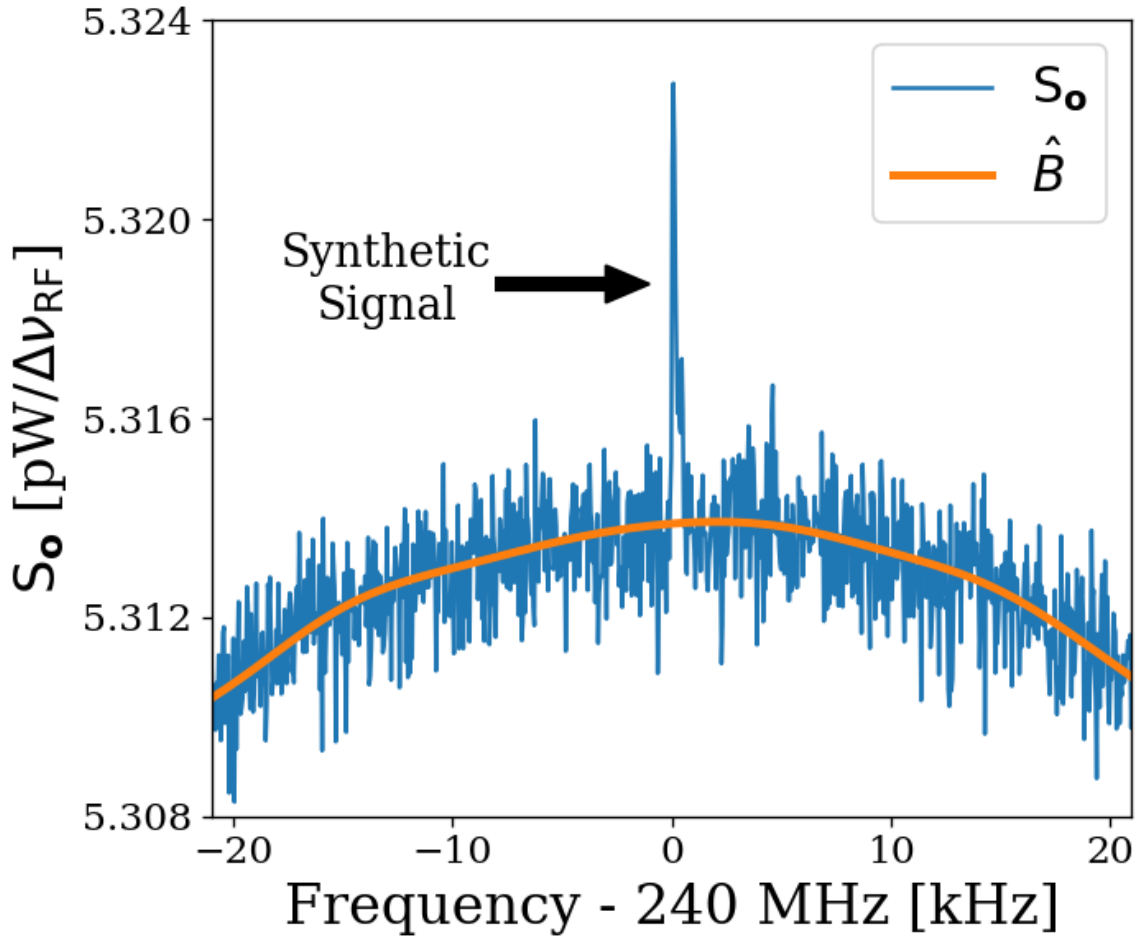


Figure 4.4: Fitting background \hat{B} in the presence of a synthetic signal injected at 240 MHz. Starting from the averaged, output-referred spectrum (S_o), we fit the background using a series of filters (section 4.2.1, and Fig. 4.3). This figure is a highly zoomed in view (240 MHz \pm 20 kHz) in order to show the noisy Rayleigh signal shape.

1502 **4.2.2 Normalized spectrum, S_o^{norm}**

1503 Once we have a fit to the background, \hat{B} , division of S_o by this fit yields a dimensionless,

1504 Gaussian distributed spectrum

$$S_o^{\text{norm}} \equiv \frac{S_o}{\hat{B}}. \quad (4.1)$$

1505 As discussed in Sec. 2.1.1.3, this normalized spectrum (Fig. 4.5) should have a mean $\mu_{\text{norm}} = 1$
 1506 and a standard deviation given by the Dicke radiometer equation $\sigma_{\text{norm}} = (\tau \Delta\nu_{\text{RF}})^{-1/2}$ where
 1507 τ is the total integration time (≈ 9 days) and $\Delta\nu_{\text{RF}}$ is the width of a bin (47.7 Hz). This
 1508 works out to a predicted σ_{norm} of 1.727×10^{-4} . μ_{norm} and σ_{norm} calculated from the data
 1509 are $1 - 1.2 \times 10^{-5}$ and 1.741×10^{-4} respectively, which agree with the predicted values
 1510 to better than 1%. Knowing the statistics of the background allow us to set a threshold
 1511 above which we have some confidence that a candidate is not a random fluctuation. This
 1512 significance threshold was derived in Sec. 2.2.1. As a reminder, the probability that all N
 1513 bins are less than z standard deviations, $z\sigma$, for a standard normal distribution is given
 1514 by $\left\{ \frac{1}{2} [1 + \text{erf}(z/\sqrt{2})] \right\}^N$, where $\text{erf}(z)$ is the standard error function and z is real. A 5%
 1515 ST for 5.2×10^6 bins (our 50-300 MHz analysis span) works out to 5.6σ . This is shown in
 1516 Fig. 4.5.

1517 It is possible to set a simple limit using this significance threshold on the normalized
 1518 spectrum, which was our method in [4]. However, knowing the line shape of the dark photon
 1519 signal provides additional information that improves sensitivity (up to a factor of ≈ 2) at
 1520 the higher frequency end of the spectrum, as shown in Fig. 4.8.

1521 **4.2.3 Signal-matched filter**

1522 As discussed in 4.2.2, one simple method to set a limit is to look for single-bin excursions
 1523 above some threshold. However, galactic dynamics impart a dark photon candidate with
 1524 a Rayleigh-distributed, spectral signature, which has a dimensionless width $Q_{\text{DP}} \approx 10^6$

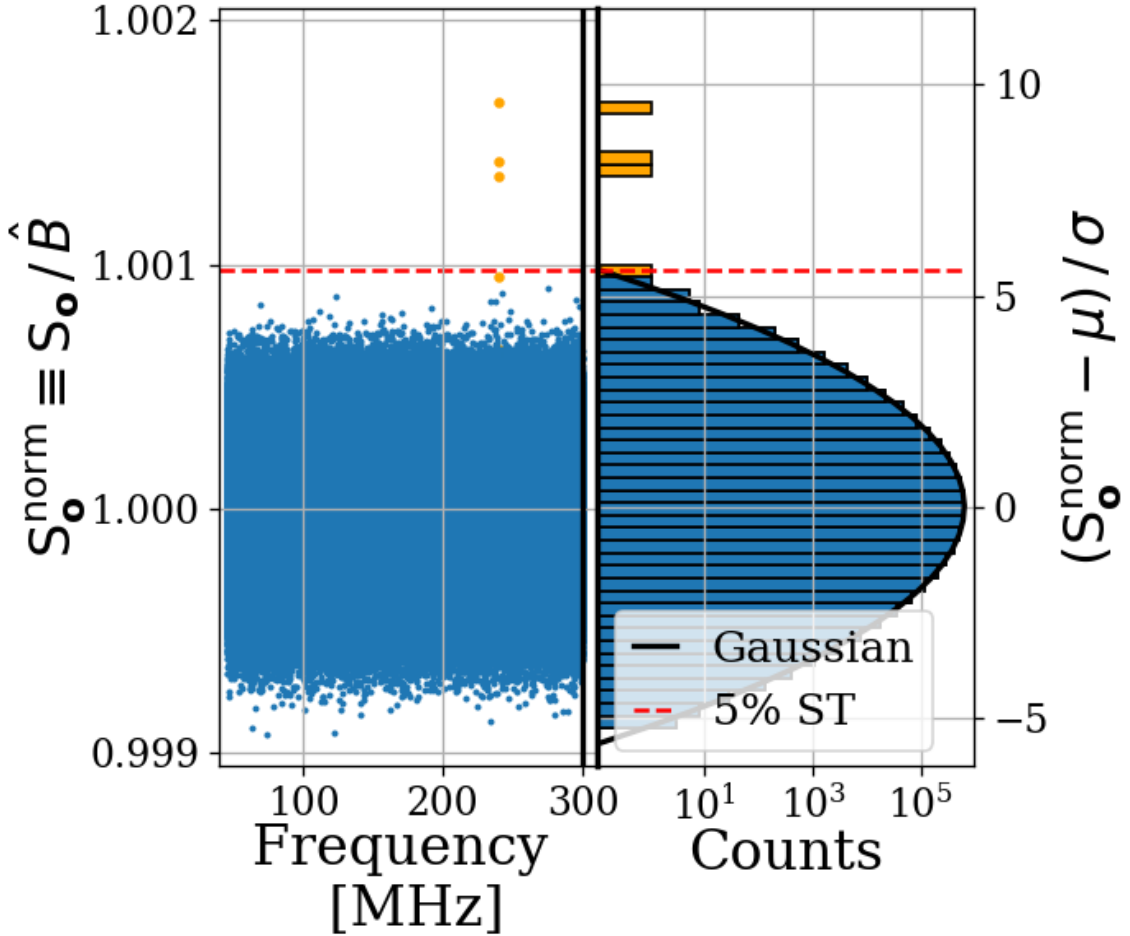


Figure 4.5: Dividing S_o by \hat{B} yields a dimensionless, normally distributed power spectrum that we define as S_o^{norm} . We show S_o^{norm} in two ways: a normalized power/frequency spectrum (*left*) and rescaled into Z-score units and collapsed into a histogram (*right*). The histogram shows power excess and Gaussian fit, but frequency information is lost. We compute a 5% significance threshold ST (*dashed red*), above which we will detect a candidate by chance 5% of the time. Bins adjacent to the 240MHz synthetic signal show up in orange on both plots. A single interfering signal has been removed for clarity. We discuss this further in Sec. 4.2.5

1525 [30]. This means that the expected width of a candidate signal over our analysis span (50-
1526 300 MHz) varies between 50-300 Hz. We set $\Delta\nu_{\text{RF}} = 47.7$ Hz to maximize SNR for the lowest
1527 expected signal width. However, this divides signal power between adjacent bins, an effect

1528 that becomes more pronounced at higher frequencies, leading to a decrease in sensitivity.
1529 By using a signal processing technique known as *signal-matched filtering* [64, 65], we restore
1530 some of the sensitivity lost due to the splitting of signal between the fixed-width frequency
1531 bins of the FFT. A similar “optimal weighting” procedure has been well established in axion
1532 haloscope experiments, notably by [17, 66]. Below, the signal-matched filter is referred to
1533 simply as a matched filter.

1534 For a known signal shape, the detection technique which optimizes SNR is the matched
1535 filter. This is implemented on the normalized power spectrum using the Rayleigh spectral
1536 line shape of [30] as a template. Since we have a constant $\Delta\nu_{\text{RF}}$ and expect the width of
1537 the signal to vary across our span, we must calculate several templates of varying width to
1538 match the expected line shape. Every 10% of fractional frequency change, a new template
1539 is generated and used to search that small sub-span of the normalized spectrum, each of
1540 which is also normally distributed though with its own standard deviation. This results in
1541 20 subspans (50-55 MHz, 55-60.5 MHz etc.). The normalized spectra of all 20 subspans and
1542 the histogram of the 227-250 MHz subspan are shown in Fig. 4.6.

1543 As the width of the templates increase, the standard deviation of the output decreases,
1544 resulting in the $\nu^{-1/2}$ shape of the 5% significance threshold shown in Fig. 4.6. It should be
1545 noted that since the total number of bins remains 5.2 million, the 5% significance threshold
1546 still corresponds to 5.6σ ; the shaping in Fig. 4.6 is due to the variation in σ for different
1547 templates, not a change in the $z = 5.6$ pre-factor.

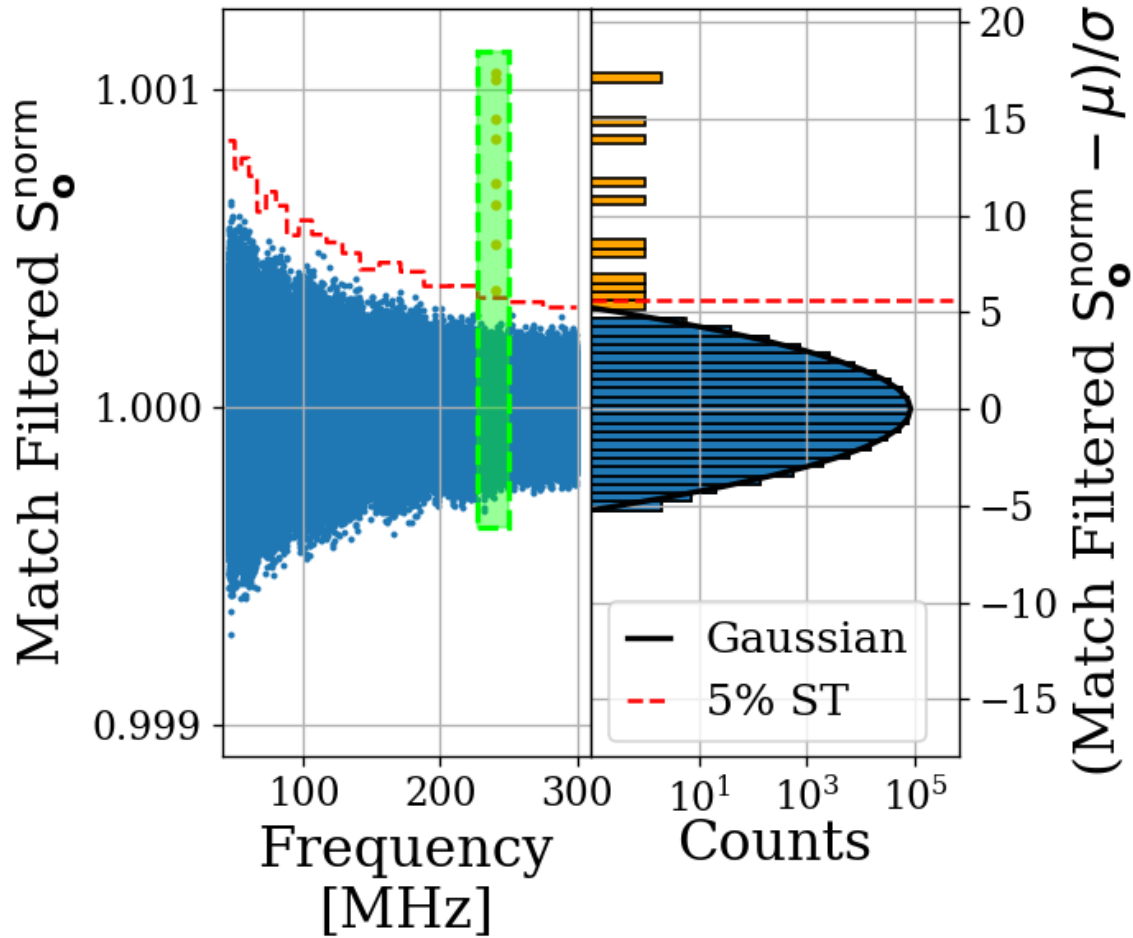


Figure 4.6: S_o^{norm} after it has been passed through a matched filter. The template varies in width throughout the frequency span resulting in 20 subspans, each with a constant 5% significance threshold ST (*dashed red*). Histogram only includes 227-250 MHz subspan (enclosed in the green box). The signal-to-threshold ratio of the synthetic signal (orange) improves by a factor of about 1.8 as compared to Fig. 4.5 without a matched filter. The frequency dependence of this effect is shown in Fig. 4.8. A single interfering signal has been removed for clarity.

1548 4.2.4 Monte carlo: pseudo experiments

1549 The previous three sub-sections outline the procedure for detecting the presence of a signal
1550 of known spectral line shape embedded in wide-band noise. We refer to this procedure as a

1551 *detection algorithm* (see Fig. 4.3) which we now calibrate through a Monte Carlo method.

1552 A synthetic spectrum is constructed by multiplying some B by randomly generated Gaussian
1553 white noise characterized by μ_{norm} and σ_{norm} , as discussed in section 4.2.2. A signal
1554 of known, total integrated, output-referred power and frequency, $\lambda(p, \nu)$, can now be added
1555 to this spectrum to create a test spectrum which can be passed through the detection al-
1556 gorithm. The frequencies of the synthetic signals are evenly spaced (approximately every
1557 10 MHz). However because the signal spans a limited number of bins (one to six), the shape
1558 of the discretized signal is very sensitive to where its peak lands relative to the bins. To
1559 compensate for the fact we don't know where a dark photon's peak would land relative to
1560 the frequency bins, the frequency of the synthetic signal is randomly jittered by $\pm\Delta\nu_{\text{RF}}/2$,
1561 which is drawn from a uniform probability distribution at each iteration of the Monte Carlo.
1562 By repeating this with randomly generated Gaussian noise and various synthetic signals
1563 (including a small jittering of signal frequency outlined above), statistics are built up about
1564 how much total integrated power is required to detect a signal as a function of frequency
1565 *most of the time*. We quantify this as the statistical power of the detection algorithm and
1566 denote it $100\% - Y = 95\%$ following the standard convention of hypothesis testing.

1567 This Monte Carlo allows us to treat the detection algorithm as a black box which can be
1568 calibrated by passing it a known input (a synthetic S_o containing a synthetic signal, both
1569 software-generated) and looking at its output; a Boolean array of frequency bins representing
1570 signal detection. These data along with a simple linear fit to the 95% confidence interval
1571 are shown in Fig. 4.7.

1572 The output MC_{lim} , normalized to standard deviation can simply be converted back to the

	Only Noise	Noise + Signal
Detection	X	100% – Y
No Detection	100% – X	Y

Table 4.2: Threshold parameters that are part of the detection algorithm and Monte Carlo. X is the significance of the analysis. It is a parameter passed to the detection algorithm which specifies the significance threshold. The quantity 100% – Y is the statistical power of the analysis. It is a parameter in the MC, which specifies a threshold on signal power where a given signal is detected in 100% – Y of the MC iterations. We choose both X and Y = 5%.

1573 limit on the total output-referred power contained in injected signals which can be detected
 1574 95% of the time,

$$P_o^{\lim} = MC_{\lim} \sigma_{\text{norm}} \hat{B}. \quad (4.2)$$

1575 MC_{\lim} is then a measure of how much the analysis' efficacy is reduced compared to an
 1576 ideal analysis where a signal with 5.6σ of power is detected at 95% significance half of the
 1577 time (remember, it's still a random process. Refer back to Sec 2.2).

1578 P_o^{\lim} is shown in Fig. 4.8 in blue. Also shown in Fig. 4.8 is a limit that does not include
 1579 any matched filtering (orange) to highlight the frequency dependent improvement of the
 1580 matched filter; this limit is only for illustration and not used in the following sections.

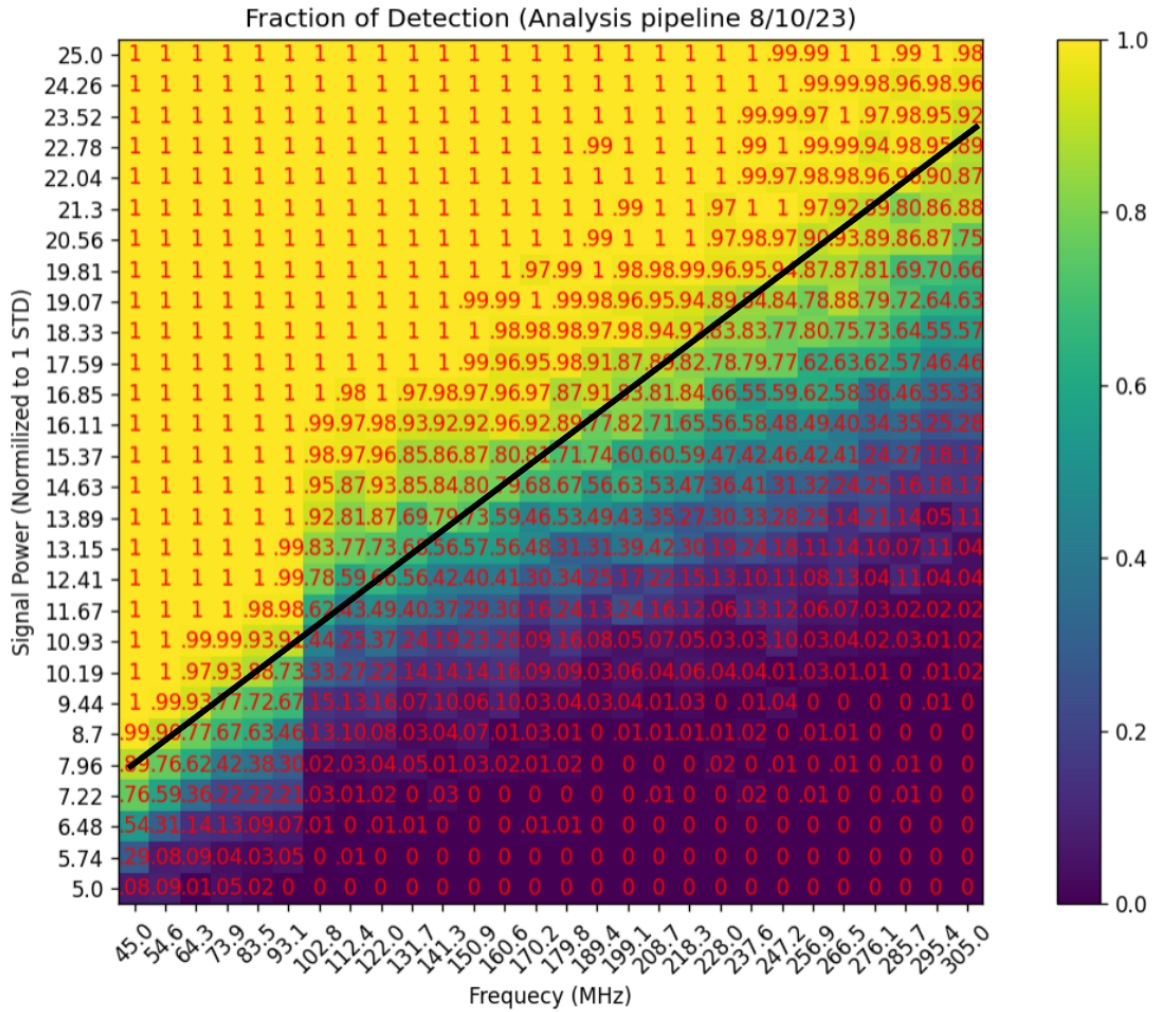


Figure 4.7: Result of Monte Carlo pseudo experiments on signal detection. Color/red numbering show fraction of detection for each frequency/injected signal power of the 784 combinations tested. Black line inserted by eye and gives an approximate fit to the frequency vs. injected signal power which results in a detection 95% of the time. Approximate form of back line is $y = 0.0686x + 2.411$

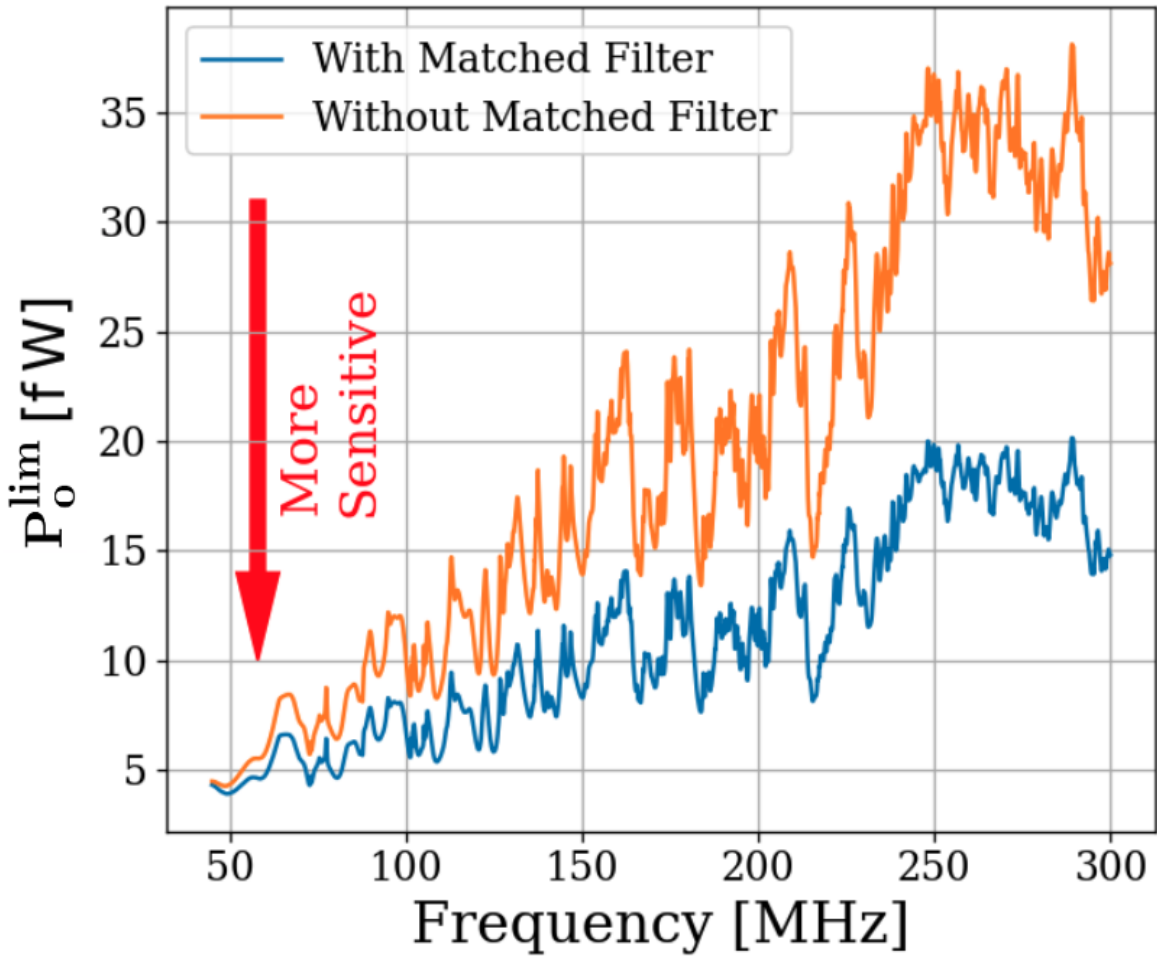


Figure 4.8: Limit on output-referred total integrated signal power, P_o^{\lim} . Limits computed with (blue) and without (orange) a matched filter (Sec. 4.2.3). The limits are similar at lower frequency but the matched filter improves sensitivity at higher frequencies where the signal power is split among more bins. The blue curve is used in the following sections.

1581 **4.2.5 Rejection of a single candidate**

1582 Passing S_o through the detection algorithm diagrammed in Fig. 4.3 yields a single candidate
1583 at 299.97 MHz which is approximately 1 kHz wide. This candidate first became detectable
1584 above the noise after about 4 days of averaging, indicating it is just on the threshold of what
1585 we are able to detect. Four factors cause us to conclude the candidate is an interfering signal
1586 originating from within the PC or ADC, allowing us to remove it:

1587 • The candidate is present not only in the main spectrum, but also the veto and termi-
1588 nator spectrum.

1589 • Inspection of the time evolution of this signal shows a narrow signal (about two bins,
1590 or 100 Hz wide) which seems to wander in frequency periodically over the course of a
1591 day and therefore with temperature. This is expected behavior for a quartz oscillator.

1592 • Reducing the gain of the system causes the SNR of the candidate to *increase*, indicating
1593 it enters the signal path after the gain stages.

1594 • Changing the clock rate causes the frequency of the candidate to change.

1595 The limit set in this section is referred to the output of the amplifier chain. A single
1596 significant candidate was found, but the method of ruling it out was outlined above. The
1597 topic of the next section will be to work back through the amp chain, to an E-field limit in
1598 the cavity and ultimately to a limit on ϵ .

1599 4.3 Calibration

1600 In this section we describe the calibration of our experiment and estimate our uncertainty.

1601 The previous section concluded with a limit on the output-referred power P_o^{\lim} (Fig. 4.8),

1602 which we now must convert into a frequency dependent limit on ϵ .

1603 We begin by inverting Eq. 1.7,

$$\epsilon(\nu) < \sqrt{\frac{|\mathbf{E}_{\text{ant}}^{\lim}|^2 \varepsilon_0}{2 \rho_{DM}}}, \quad (4.3)$$

1604 where the *lim* superscript indicates a limit, below which a detectable electric field may be

1605 hiding. The $<$ should be taken to mean that in setting a limit on $|\mathbf{E}_{\text{ant}}^{\lim}|$, ϵ is constrained to

1606 be less than the right hand side (if it exists at all).

1607 The first step of calibration is to convert from output-referred power to *antenna referred*

1608 *power*. This represents the signal power presented to the LNA by the antenna via a matched

1609 transmission line and is given by

$$P_{\text{ant}}(\nu) = \frac{P_o}{G} - T_{\text{amp}} k_B \Delta\nu_{\text{RF}}, \quad (4.4)$$

1610 where G and T_{amp} are the frequency-dependent amplifier gain and noise temperature (74–75 dB

1611 and 100–120 K respectively, measured via the Y-factor method, see Sec. 3.1.1) and k_B is

1612 Boltzmann’s constant.

1613 Ultimately, the exclusion limit is set by fluctuations on this baseline described by

$$\begin{aligned}
P_{\text{ant}}^{\lim}(\nu) &= \frac{P_{\text{o}}^{\lim}}{G} - \left(\frac{2}{n} \right)^{1/2} T_{\text{amp}} k_B \Delta\nu_{\text{RF}} \\
&= \frac{P_{\text{o}}^{\lim}}{G} - \left(\frac{2 \Delta\nu_{\text{RF}}}{\tau} \right)^{1/2} T_{\text{amp}} k_B,
\end{aligned} \tag{4.5}$$

where the *lim* superscript indicates an exclusion limit, n is the total number of spectra averaged together, and τ is the total integration time. In the second line we have used $n = \Delta\nu_{\text{RF}} \tau$. In practice, the LNA correction is small; the first term divided by the second varies with frequency between 7 and 50. The $\tau^{-1/2}$ dependence of P_{o}^{\lim} is implicit because it was calculated from S_{o} which is itself an averaged spectrum. As mentioned above, this $\tau^{-1/2}$ dependence implies that the limit on ϵ scales as $\tau^{-1/4}$.

In the remainder of this section we explore the relationship between P_{ant}^{\lim} and $|\mathbf{E}_{\text{ant}}^{\lim}|$ allowing us to use our experimental data to set a constraining limit on ϵ by employing Eq. 4.3.

4.3.1 Average effective aperture, $\langle A_e(\nu) \rangle$

An antenna's effective aperture, A_e [m^2], represents the effective area that it has to collect power density or irradiance [W/m^2] from an incident Poynting vector. It was defined in Eq. 2.9.

A_e is useful for an antenna in free space, however some modifications must be made to construct an analogous quantity for an antenna in a cavity.

The first modification is to average over many configurations of the system. The background for this is given in Sec. 2.4. As discussed, we denote this averaging with $\langle \rangle$ so that the

1631 average, effective aperture is denoted $\langle A_e \rangle$. It is interesting to note that by averaging over
1632 configurations (namely antenna direction), $\langle A_e \rangle$ simplifies since $\langle D(\Omega) \rangle = 1$ by construction
1633 [20].

1634 The second modification is to introduce a resonant enhancement factor which corresponds
1635 to the system's tendency to "ring up" in the same way any resonator will. We refer to
1636 this as *composite Q* and represent it as \tilde{Q} . It is analogous to the standard quality factor
1637 of a resonator with one important modification; we operate our experiment across a wide
1638 frequency range so we define \tilde{Q} across the continuum of these resonances, not only on classical
1639 eigenmodes of the system.

1640 These modifications allow us to construct a relationship between an observable E-field
1641 (\mathbf{E}_{ant} in Eq. 4.3) and the power available at the port of an antenna for a given aperture

$$\langle P_{\text{ant}} \rangle = \frac{|\mathbf{E}_{\text{ant}}|^2}{\eta_0} \langle \tilde{Q} A_e \rangle, \quad (4.6)$$

1642 where η_0 is the impedance of free space. With this in mind, we perform an RF simulation
1643 to compute $\langle \tilde{Q} A_e \rangle$.

1644 4.3.2 Simulation of $\langle \tilde{Q} A_e \rangle$

1645 It is difficult to make claims about statistical uniformity in the "undermoded" regime where
1646 modes are not sufficiently mixed [67], so we have employed a commercial electromagnetic
1647 finite-element modeling software package (COMSOL Multiphysics RF module [45]). The
1648 original paper explicitly on modeling reverb chambers seems to be [68], though it only

1649 considers a 2-dimensional model and is rather rudimentary. Within the simulation, a model
1650 of the antenna (with a 50Ω feed) is placed in a simplified room with wall features removed.
1651 Spot testing at various frequencies has shown that averaging results from various antenna
1652 positions using this simplified simulation behaves very similarly to one with the room features
1653 included at a fraction of computational complexity.

1654 Two similar simulations are run; driving an E-field while measuring the antenna's re-
1655 sponse and driving a second small monopole antenna and measuring the response of the
1656 primary antenna.

1657 In the first simulation, we drive currents on the walls which correspond to a surface E-
1658 field magnitude of 1 V/m (made up of equal components in the x, y and z directions) using
1659 COMSOL's source electric field option. This field takes the place of \mathbf{E}_{ant} in Eq. 4.6. The
1660 antenna/cavity system resonates and causes an enhancement by \tilde{Q} . The power received at
1661 the antenna's port is measured, allowing the calculation of $\tilde{Q} A_e$, again from Eq. 4.6. By
1662 repeating this simulation for several positions, averaging allows us to compute $\langle \tilde{Q} A_e \rangle$.

1663 The second simulation shares the same geometry, but is used to compute a correction
1664 factor to account for differences between simulation and measurement and to estimate un-
1665 certainty on the first simulation through comparison to physical measurement. Rather than
1666 driving the system through currents on the walls, power is injected into the system with
1667 a 40 cm monopole. From this simulation, two port scattering parameters (S parameters,
1668 defined in 4.3.3) are computed. A similar test is performed on the physical system using a
1669 vector network analyzer (VNA) which provides a physical measurement of the S parameters
1670 to compare with the simulation. The processing of the simulated and measured S parameter

1671 datasets are discussed in the following sub-section. A screenshot of the COMSOL model GUI
 1672 is shown in Fig. 4.9. The resulting S parameters from the simulation are plotted against the
 1673 measured S parameters in Fig. 4.10

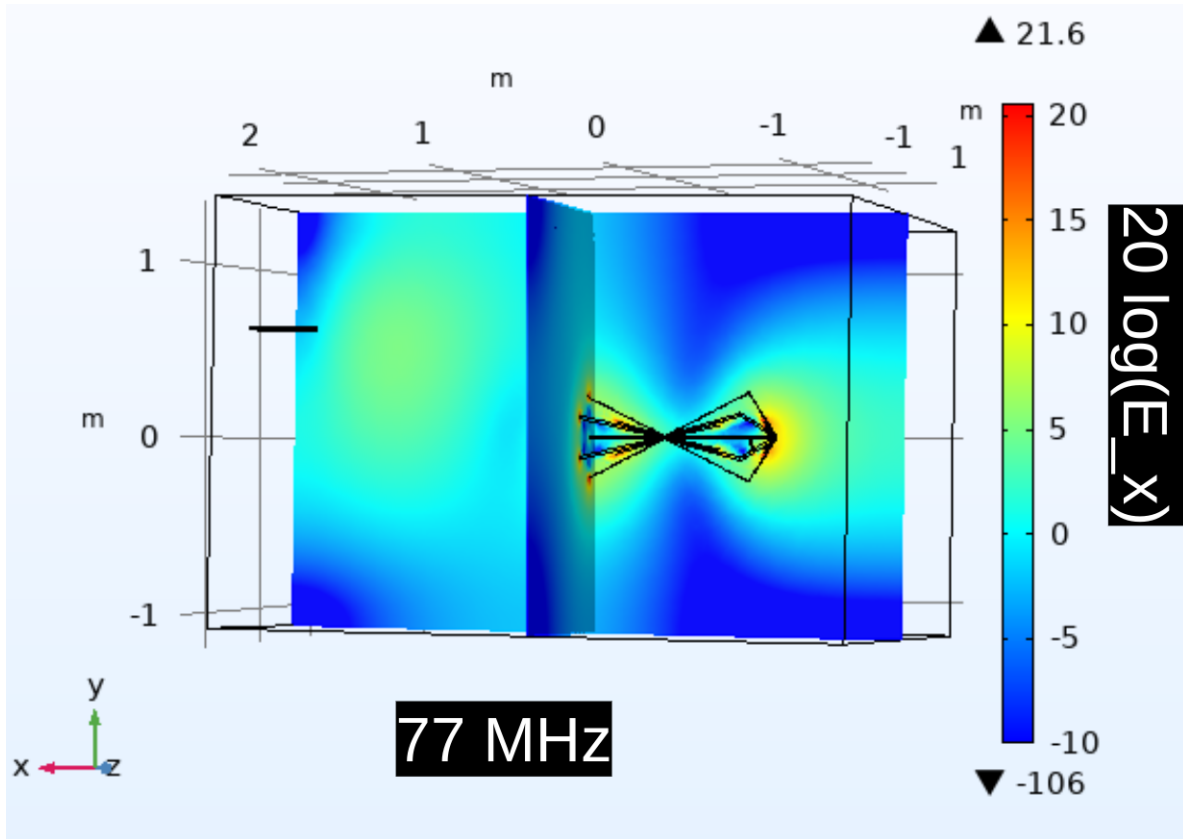


Figure 4.9: Screenshot of COMSOL simulation GUI for two-antenna validation. Shown only at a single position and single frequency (77 MHz). There are 18 antenna positions, 3 E-field components, and ≈ 1000 frequency points, so there are many similar figures to this one. X component of electric field shown as color in dB compared to 1 V/m.

1674 Both simulations are run at the same 18 positions; 9 of which are approximately equiv-
 1675 alent to the physical antenna positions while the other 9 are different in order to estimate
 1676 how many positions are required for decent convergence of $\langle \tilde{Q} A_e \rangle$. Repeatedly averaging 9
 1677 different, random positions (with replacement) results in about 20% variation on their aver-

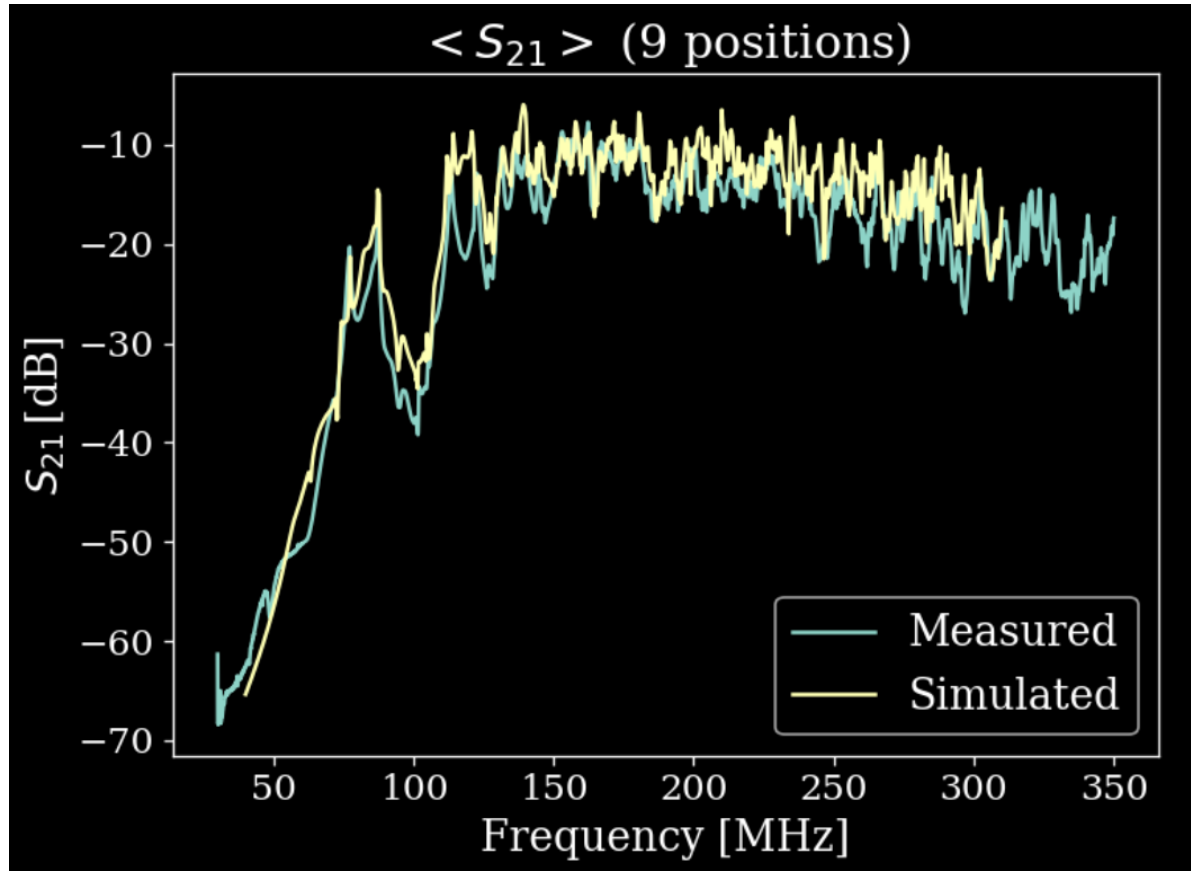


Figure 4.10: Simulated vs measured $\langle S_{21} \rangle$ comment: Replot without dark theme.

1678 aged S_{12} coefficients at each frequency, allowing us to conclude 9 positions and polarizations

1679 provides acceptable convergence.

1680 4.3.3 Correction and uncertainty of $\langle \tilde{Q} A_e \rangle$

1681 As outlined above, we approximate the uncertainty of the simulation by injecting power into

1682 the system via a second antenna and comparing the results to simulation.

1683 For a two port microwave device, the ratio between the voltage presented at port one

1684 and the voltage measured at port two is known as S_{21} . For our system, S_{21} is a measurable

1685 quantity which is similar to a dark photon detection in that it requires the antenna to convert
1686 an electric field (which has interacted with the room) into a port voltage. Having frequency
1687 dependent measurements of S_{21} for simulation and measurement give us a correction to
1688 the simulation (to account for discrepancies in geometry) and estimate the uncertainty on
1689 $\langle \tilde{Q} A_e \rangle$.

1690 The difference between the measured and simulated values of $\langle |S_{21}| \rangle$ can be described by

$$\langle |S_{21}^{\text{meas}}|^2 \rangle = \alpha \langle |S_{21}^{\text{sim}}|^2 \rangle, \quad (4.7)$$

1691 where meas/sim indicates measured/simulated and the average is over all 18 measured/sim-
1692 ulated positions and orientations of the antenna. We have taken the square since we are
1693 interested in the aperture, which is proportional to the square of the voltage. This equa-
1694 tion implies α is a frequency dependent, multiplicative correction factor which results in a
1695 corrected $\langle |S_{21}^{\text{sim}}|^2 \rangle$. We find α to have a mean of 0.6, a minimum of 0.1 and a maximum of
1696 2.

1697 To determine uncertainty on effective aperture, we define the following test statistic

$$\Delta = \frac{\langle |S_{21,n}^{\text{meas}}|^2 \rangle - \alpha \langle |S_{21,n}^{\text{sim}}|^2 \rangle}{\langle |S_{21}^{\text{meas}}|^2 \rangle}, \quad (4.8)$$

1698 where n refers to the subset of n measured/simulated positions sampled randomly with re-
1699 placement. Δ defines the fractional difference between corrected, simulated S_{21} and measured
1700 S_{21} . The test statistic, Δ , is calculated 1000 times, providing a distribution of frequency
1701 dependent Δ s. The curves bounding 63% of these curves are taken to be the uncertainty on

1702 Δ . Thus we can calculate the corrected $\langle \tilde{Q} A_e \rangle$ as well as its uncertainty. This is shown as
 1703 a function of frequency in Fig. 4.11. The uncertainty on it is shown in gray, and is simply

$$\delta\langle \tilde{Q} A_e \rangle = \langle \tilde{Q} A_e \rangle \delta\Delta. \quad (4.9)$$

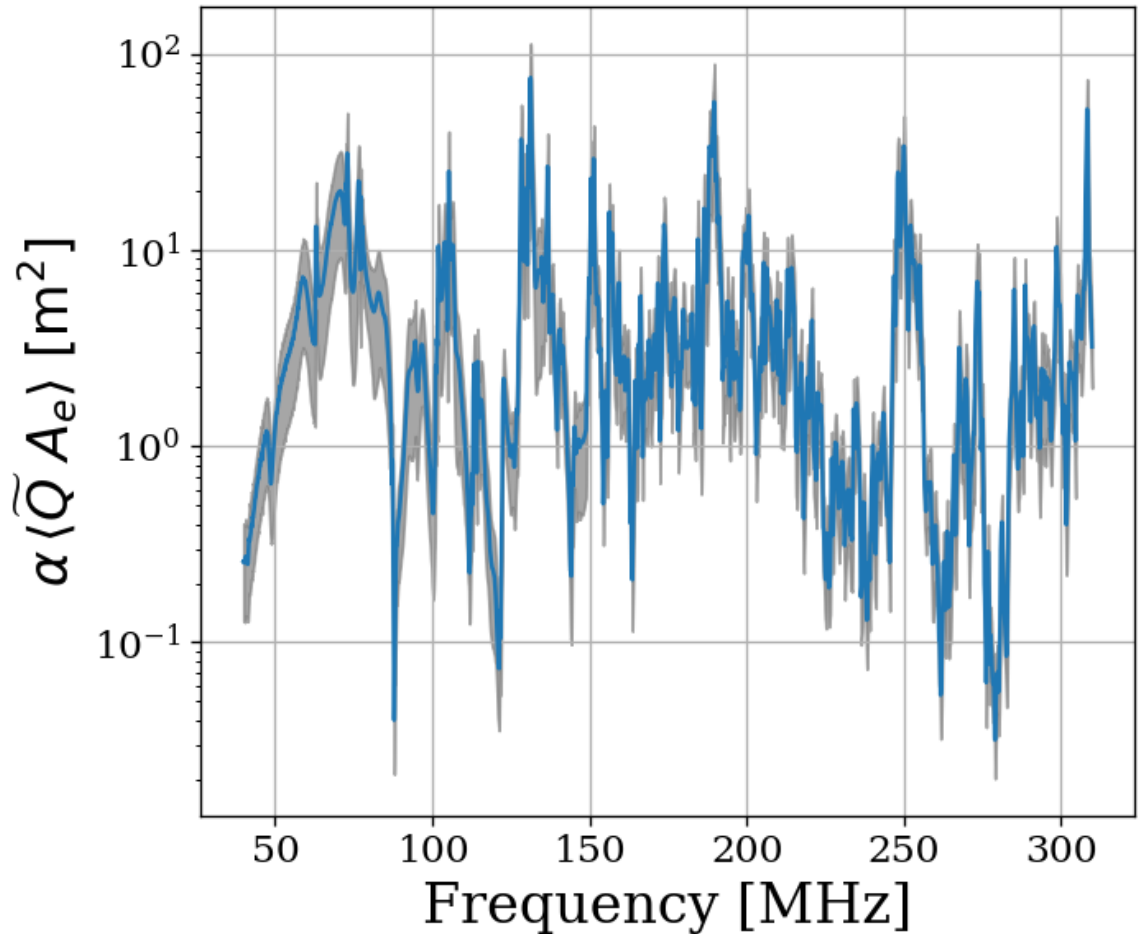


Figure 4.11: Corrected average effective aperture. Calculated with COMSOL RF. The aperture correction α (Eq. 4.7) and its uncertainty (*gray*) are estimated by comparing simulations to measured S parameters.

1704 A brief summary of the system's aperture is in order. In free space an antenna's ability

1705 to couple an incoming wave's power density into a transmission line is given by it's effective
 1706 aperture, Eq. 2.9. An antenna in a cavity acts as a coupled oscillator which exhibits very
 1707 complex resonances above the first few modes (around 100 MHz for our system). Attempts
 1708 to simulate an aperture for the antenna-cavity system are difficult because of the system's
 1709 extreme dependence on placement of any conductor in the room, especially the antenna.
 1710 Averaging over system configurations (antenna positions and polarizations in our case) allows
 1711 for a significantly more repeatable *statistical* treatment of the aperture/quality factor, which
 1712 we call $\langle \tilde{Q} A_e \rangle$. Comparison of simulated and measured S_{21} gives a small, dimensionless
 1713 correction factor α , Eq. 4.7.

1714 Armed with $\alpha \langle \tilde{Q} A_e \rangle$ we are now able to compute a limit on epsilon using measured and
 1715 simulated quantities via Eqs. 4.5 and 4.6,

$$\epsilon(\nu) < \sqrt{\frac{1}{2c\rho_{\text{DM}}} \frac{P_{\text{ant}}^{\text{lim}}}{\alpha \langle \tilde{Q} A_e \rangle}}, \quad (4.10)$$

1716 where c is the speed of light, ρ_{DM} is the local dark matter density and $P_{\text{ant}}^{\text{lim}}$ is defined in
 1717 Eq. 4.5. We have separated the equation into constants (or in the case of ρ_{DM} , values which
 1718 we fix) and values which we measure or simulate.

1719 In order to validate our entire detection system, we inject sub-threshold signals into the
 1720 shielded room to verify we are able to detect them.

1721 **4.4 Hardware Injection Test**⁴

1722 To validate detection methodology, a separate, proof-of-concept run with an a proxy dark
1723 photon signal injected into the shielded room was performed. Apart from the injection
1724 antenna (a 40 cm monopole, see Sec. 4.3.2), the setup was equivalent to run 1.4, including
1725 the data analysis. The proxy dark photon signal (detailed in Sec. 4.4.1.2) was injected at a
1726 frequency set by a colleague and was unknown to me at the time of analysis, constituting a
1727 “blind” analysis.

1728 **4.4.1 Injection test prerequisites**

1729 **4.4.1.1 Determination of required injected power**

1730 **comment: S parameters need to be squared. Check on this. See Besnier [69]** To accomplish
1731 the test, a minimum detectable power required for injection P_{inject} must be computed. P_{inject}
1732 should correspond to a signal that can be detected in a predictable amount of time (with
1733 some uncertainty, discussed in detail in Sec. 2.2.2). A simple way to begin is to read off the
1734 detectable, total integrated, power from Fig. 4.8. In other words the power contained in a
1735 dark photon line, integrated over the few bins spanned by the line ($Q_{\text{DP}} \approx 10^6$, discussed in
1736 Sec. 2.1.2). This gives the amount of output-referred power that would be detectable 95%
1737 of the time after 9 days of integration. Since we don’t want to wait 9 days for this test, it is
1738 simple to convert this detection limit into one which would be produced in a shorter time by
1739 the Dicke radiometer equation, Eq. 2.16. Namely, the limit on power scales like the square

⁴Code for this section can be found at: <https://github.com/josephmlev/darkRadio/tree/master/daqAnalysisAndExperiments/run1p4/injectionTesting/injectionTesting.ipynb>

1740 root of time ⁵, so a one hour integration will require a factor $\sqrt{9 \text{ days}/1 \text{ hour}} = 14.7$ more
1741 power than is shown in Fig. 4.8.

1742 At this point the simplest way to proceed is to measure the the average through-power
1743 of the monopole to the bicon in several antenna positions $\langle |S_{21}|^2 \rangle$. This is the same as the
1744 set up described in Sec. 4.3.2. The bicon was moved to 9 positions and the resulting S
1745 parameters were measured at the reference planes shown in Fig. 4.12. They are shown in
1746 Fig. 4.13 after being averaged together.

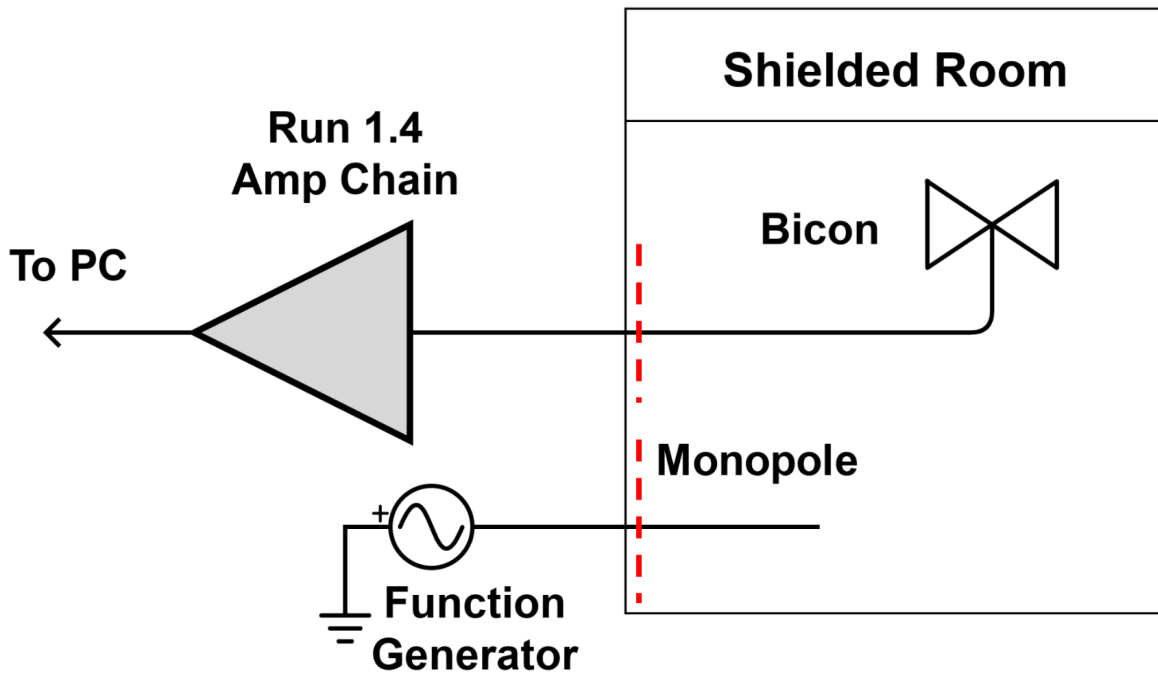


Figure 4.12: Schematic of hardware injection test. Dashed red lines indicate reference planes used to measure S parameters, shown in Fig. 4.13. “Amp Chain” includes amplifiers, attenuators and filters as described in Sec. 2.5.4.

⁵It is important to point out that one needs to test whether or not the system in question actually behaves as predicted by the Dicke equation for the amount of averaging in question. After lots of averaging, one may encounter non-thermal backgrounds which do not scale properly. It is shown in Fig. 4.16 that the dark radio system follows the Dicke radiometer equation at least for 9 days.

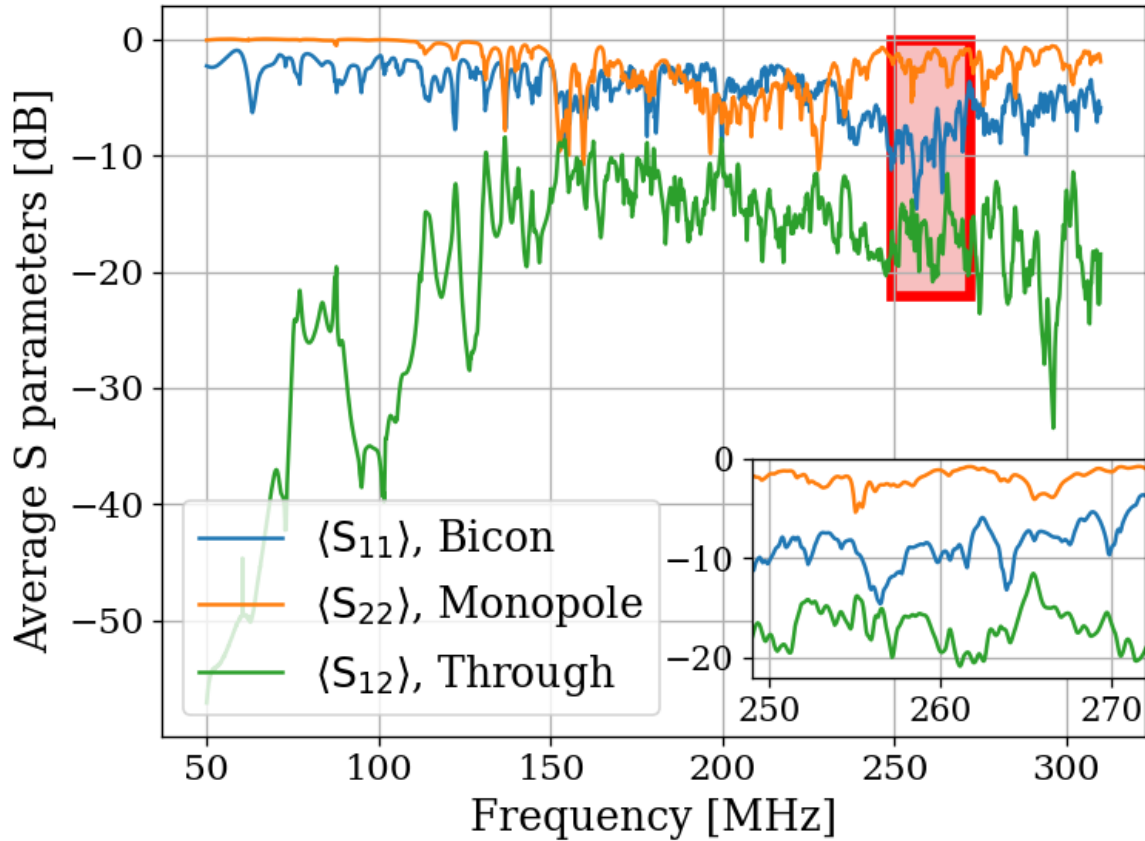


Figure 4.13: Average S parameters of hardware injection test. Taken at 9 positions of the bicon antenna and averaged together (linearly). Ports 1 and 2 are defined to be for the bicon and monopole respectively. Note that $\langle S_{12} \rangle = \langle S_{21} \rangle$ so only $\langle S_{12} \rangle$ is shown. Inset shows zoom on area enclosed by red box.

1747 Knowing the output-referred limit, the system's average $\langle |S_{21}|^2 \rangle$, and the gain G, allows
 1748 for a calculation of the required signal strength (as a function of frequency) which will become
 1749 detectable after a known amount of time. In order to simplify the test, a smaller 1 MHz
 1750 band is chosen between 268 and 269 MHz for the blind injection, where $\langle |S_{21}|^2 \rangle$ is constant
 1751 to about 1dB. At first glance, this seems to be cheating, however there are still approximately
 1752 21,000 frequency bins in this span, so a detection is very unlikely to be random. Furthermore,

1753 the entire 50-300 MHz span is sent to the detection algorithm (Discussed in Sec. 4.2 and
1754 illustrated in Fig. 4.3) which produces an output without knowing about this frequency
1755 restriction.

With all this in mind, the signal power required is simply

$$P_{\text{inject}} = \frac{P_{\text{o}}^{\text{lim}}}{G \langle S_{21} \rangle},$$

1756 where each term is a function of frequency. For the parameters described in this sec-
1757 tion (including the increase in the power limit $\sqrt{9 \text{ days}/1 \text{ hour}} = 14.7$), this works out to
1758 $\approx 6 \times 10^{-19} \text{ W}$ or -152.5 dBm. The Rigol DSG830 signal generator is not calibrated to
1759 such low levels, so this was achieved through attenuation ⁶.

1760 4.4.1.2 Proxy dark photon signal injection

1761 Now that the power for signal injection has been established, the finite-width proxy-signal
1762 ($Q_{\text{DP}} \approx 10^6$) can be generated. This is discussed in Sec. 2.1.2. An intuitive way to accomplish
1763 this would be with an arbitrary waveform generator injecting a time domain signal which is
1764 the Fourier transform of the the expected Rayleigh line shape, Eq. 2.24. This is the method
1765 of the ADMX experiment (see for example [70]). Another option would be to frequency-
1766 modulate a sine wave such that it slowly sweeps out the line shape, spending am amount of
1767 time at each frequency weighted by Eq. 2.24. While intuitive, I was unable to get this to
1768 work. Zhu et al.'s method of frequency hopping [71] is the discretized version of this and
1769 it was very simple to implement. The signal generator is set to change frequencies at some

⁶Experience with this signal generator has shown it exhibits the best performance is when it is set around -30 dBm. Higher than this, large non-harmonic distortions appear contaminating the run. Smaller, and the signal-to-spurious-noise-floor of the generator is poor, also contaminating the run.

1770 interval (discussed below). The frequency which is set is randomly drawn from the PDF of
1771 Eq. 2.24.

1772 There are two considerations that determine the frequency hop period τ_{FH} that the
1773 frequency is changed⁷. First, τ_{FH} should be much longer than the acquisition time of a single
1774 buffer τ_{FFT} ⁸. On the Rigol signal generator, the power is briefly shut off while the frequency
1775 is changed. $\tau_{\text{FFT}} \ll \tau_{\text{FH}}$ ensures that most FFTs of data don't contain a frequency-hop.
1776 Second, τ_{FH} should be small compared to the total time of integration τ , so that there are
1777 many frequencies represented in the entire run. In the limiting case, $\tau_{\text{FH}} = \tau$ will yield an
1778 averaged spectrum containing a single injected frequency; the proxy-signal will be a delta
1779 function in the frequency domain.

1780 Testing has shown that $\tau_{\text{FH}}/\tau_{\text{FFT}} \approx 10$ is more than adequate to address the first consider-
1781 ation. For run 1A (and therefore, this test which shares settings with run 1A), $\tau_{\text{FFT}} = 2^{24}/800$
1782 MHz = 21 ms, so τ_{FH} was set to 250 ms. This means that over 1 hour, the frequency will be
1783 set to $\approx 1.4 \times 10^4$, which addresses the second concern. A histogram of this signal is shown
1784 in Fig. 4.14.

⁷Zhu et al. randomized this period to prevent any unintentional periodic signals entering. I didn't find this to be necessary.

⁸One can likely bypass this restriction by coordinating the signal generator and ADC such that there is some dead time between collection of buffers, in which the frequency is set. Testing has shown that this restriction is adequate to avoid this extra programming step

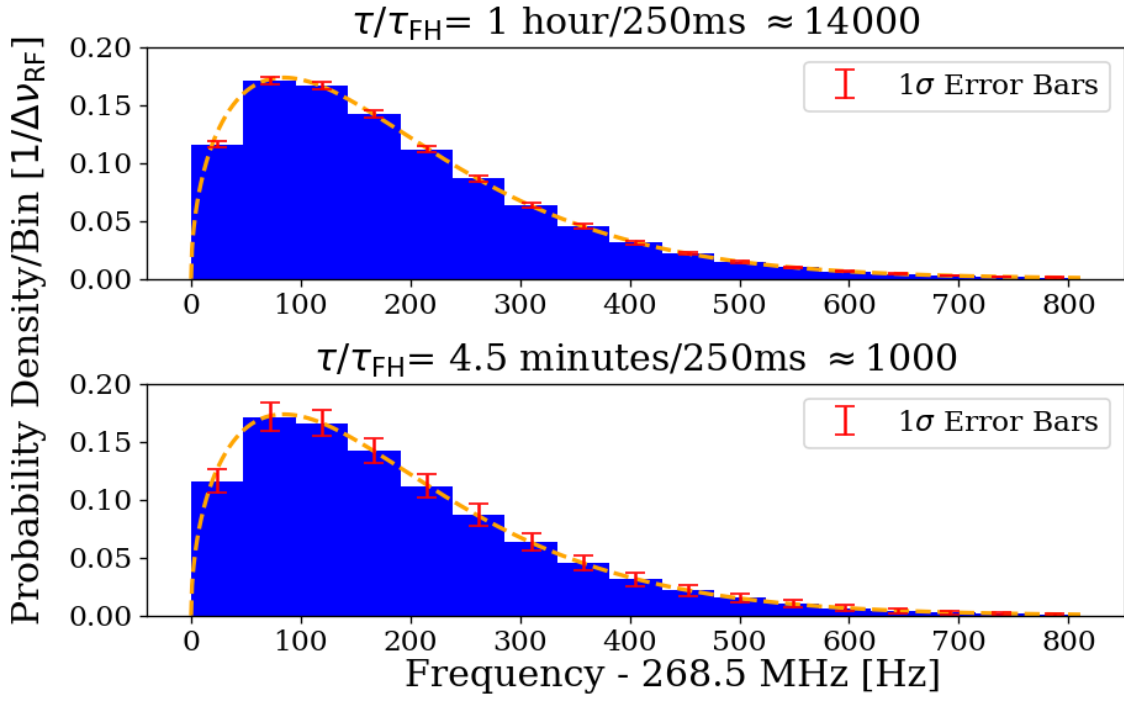


Figure 4.14: Histogram of frequencies used for hardware injection test, with realistic $\Delta\nu_{RF} = 47.7$ Hz. Orange dashed curve is expected line shape from 2.24, and is the PDF frequencies are drawn from. Blue histogram and error bars generated from Monte Carlo simulation and shows the mean value per bin, with 1σ error bars in red. This involves generating 1000 lists of random frequencies (each of length τ/τ_{FH}), binning the data and calculating the standard deviation of each bin. τ is the total acquisition time and τ_{FH} is the amount of time spent on each frequency before “hopping” to the next. Their ratio, τ/τ_{FH} is the number of frequencies which are injected in a given injection test, and was approximately 1.4×10^4 for the one hour test outlined in this section. Two plots give an idea of how error scales with τ/τ_{FH} .

1785 **4.4.2 Performing the injection test**

1786 Due to the uncertainties involved, more data were taken than the required 1 hour. This also
 1787 helped produce the pretty plot in Fig. 4 of Levine et al. [36]. 3.6 hours of data were collected,
 1788 and saved in 30 second pre-averages so that progressively more data could be averaged if
 1789 the signal was not detected at the predicated time. As mentioned above, the signal injected

1790 was at a relatively high frequency withing the span so that it would be split up into 5 or 6
1791 bins, testing the matched filter's effectiveness. The bicon was moved to 9 positions. Spectra
1792 resulting from 9 antenna positions and 30 seconds of pre-averaging at each position were
1793 averaged together giving 4.5 minute time resolution. Three of these spectra are shown in
1794 Fig. 4.15. The standard deviation of these spectra average down with the square root of time,
1795 closely following the Dicke radiometer equation (discussed in Sec. 2.1.1.3). This scaling is
1796 shown in Fig. 4.16.

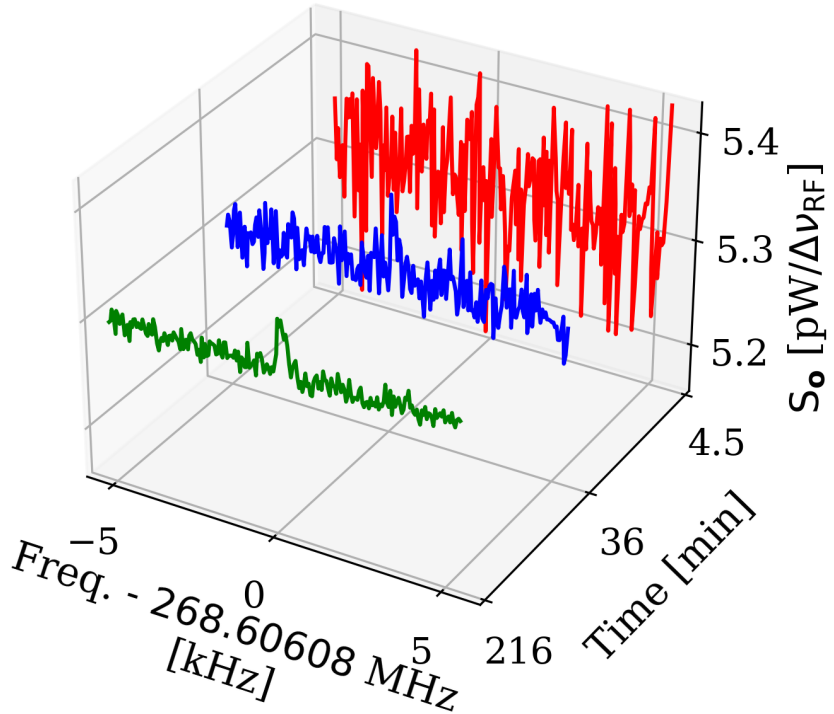


Figure 4.15: Output-referred power spectral density from the hardware injection test illustrating noise averaging down to reveal a persistent, hardware-injected, dark photon proxy signal. Spectra shown are highly zoomed around the injected frequency, 268.60608 MHz. The red, blue and green spectra represent 4.5, 36 and 216 minutes of integration time respectively. The standard deviation of these spectra (excluding the bins containing the injected signal) average down with the square root of time as expected. The blue spectrum shows the amount of averaging required for the signal to be detected by the detection algorithm (including the matched filter) at 5% significance. The tight zoom shown here is less than 1 part in 10^4 of the full 50-300 MHz spectrum analyzed.

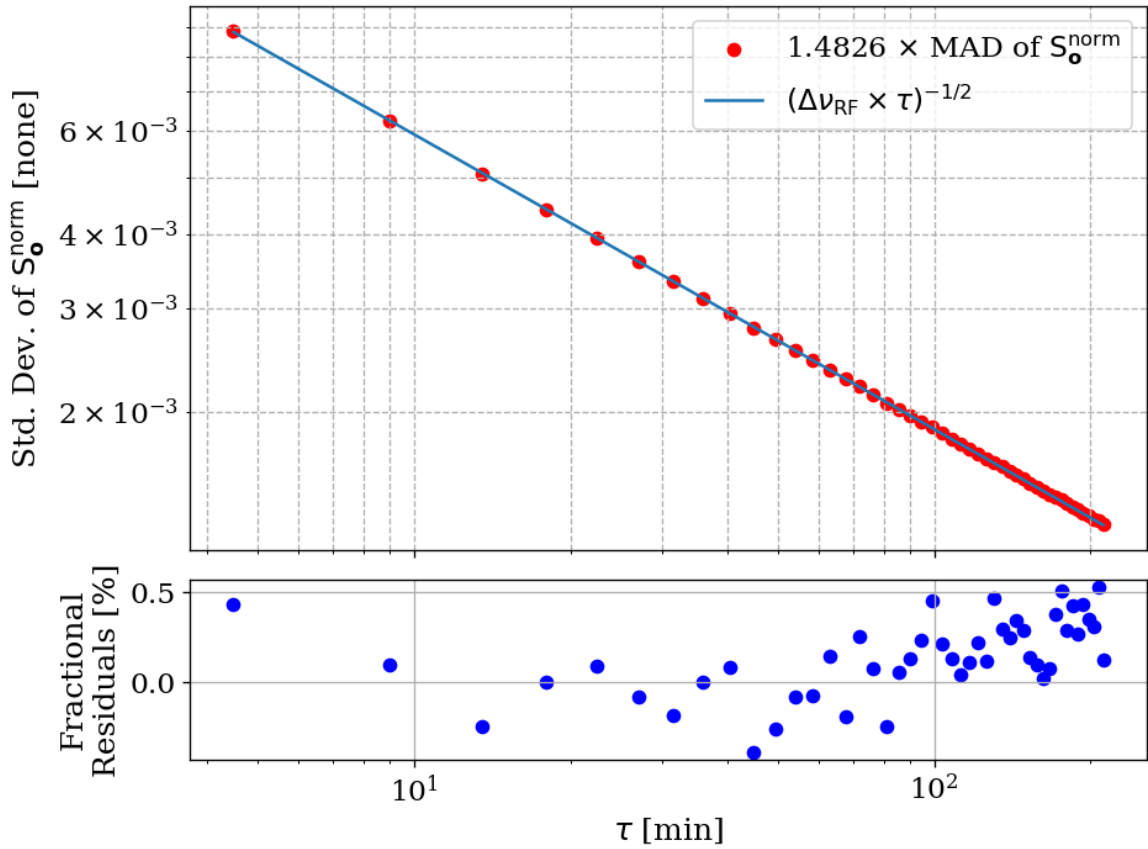


Figure 4.16: Standard deviation of output-referred power spectral density from the hardware injection test, computed with median absolute deviation (MAD). The blue curve represents the predicted standard deviation from the Dicke radiometer equation, Eq. 2.16. Each point corresponds to 9 antenna positions with an additional 4.5 minutes of data averaged (see Sec. 4.4.2). MAD provides a more robust measure of variability, reducing the influence of outliers and offering a better fit than direct standard deviation calculations.

1797 These spectra were generated one at a time and passed through the detection algorithm.
1798 The first spectrum where a signal was detected was at 36 minutes, shown in blue in Fig. 4.15.
1799 Although hardly detectable to the eye, the matched filter detects the signal with 5% signifi-
1800 cance. At the point the signal was detected (i.e. before all data were averaged together), the
1801 injection frequency was confirmed to have been correctly identified, resulting in a success-
1802 ful, blind, hardware injection test. Only after this confirmation were all the date averaged
1803 together to make Fig. 4.15.

1804 **4.4.3 Inspection of Data**

1805 This final subsection simply contains some full page figures which show data from the injec-
1806 tion test. They are all the same 34 minutes of data, but at different stages of processing,
1807 closely following the three main steps of Analysis, Sec. 4.2. They are meant to simulate the
1808 experience of inspecting a 2^{24} point FFT's power spectrum in a matplotlib widget window.
1809 The zoom is seemingly unending, a feature that is difficult to appreciate in a printed docu-
1810 ment. These figures should provide some context for how futile a manual search of unfiltered
1811 data would be. Try and pick out the signal in the top left panel of Fig. 4.17!

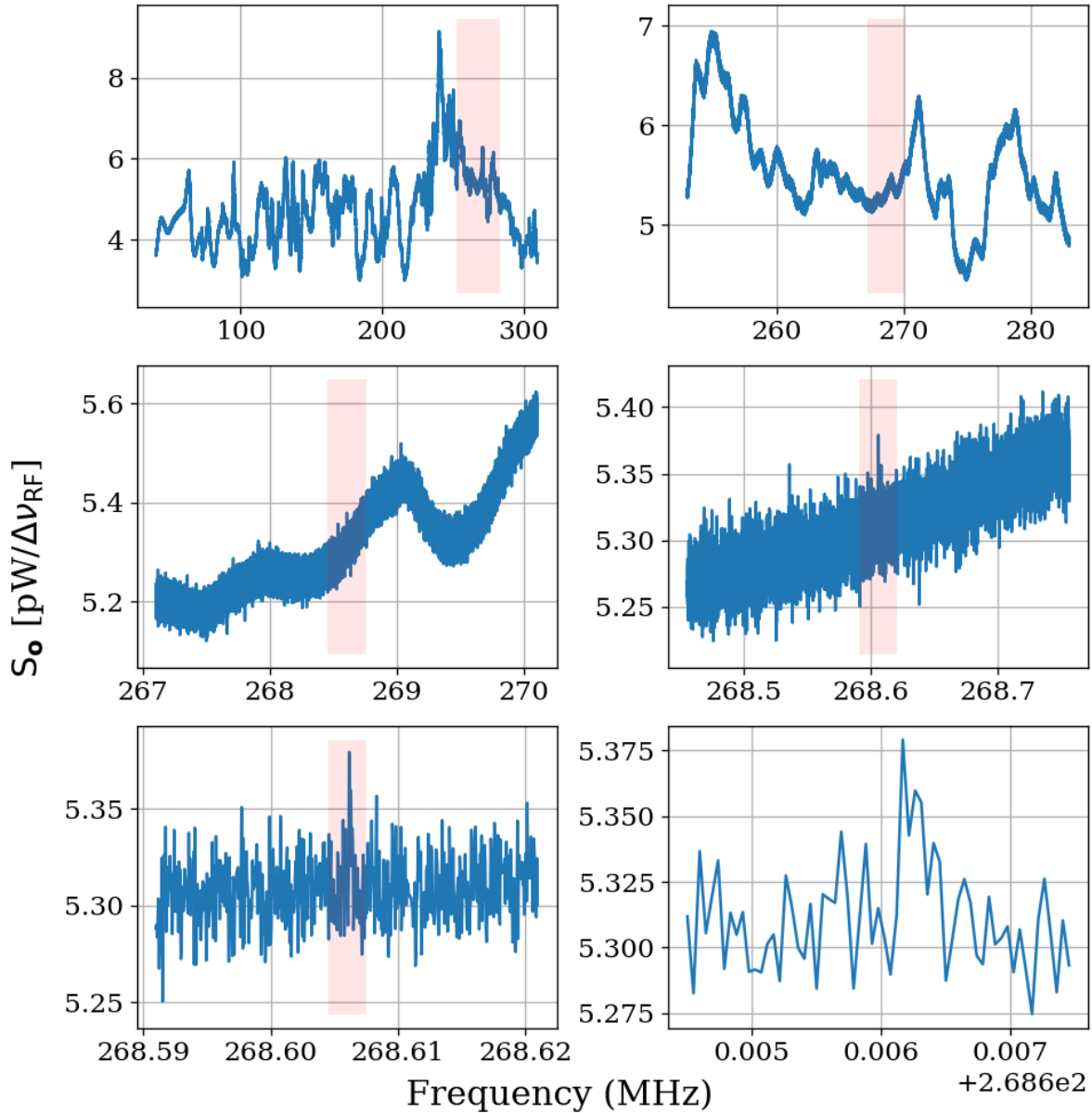


Figure 4.17: Output-referred power spectrum from hardware injection test. Injected signal at 268.60608 MHz. All spectra correspond to a total of 36 minutes of averaging, split evenly between 9 antenna positions. Full 50-300 MHz span contains $\approx 5.2 \times 10^6$ bins. Light pink boxes show zoom level on following plot.

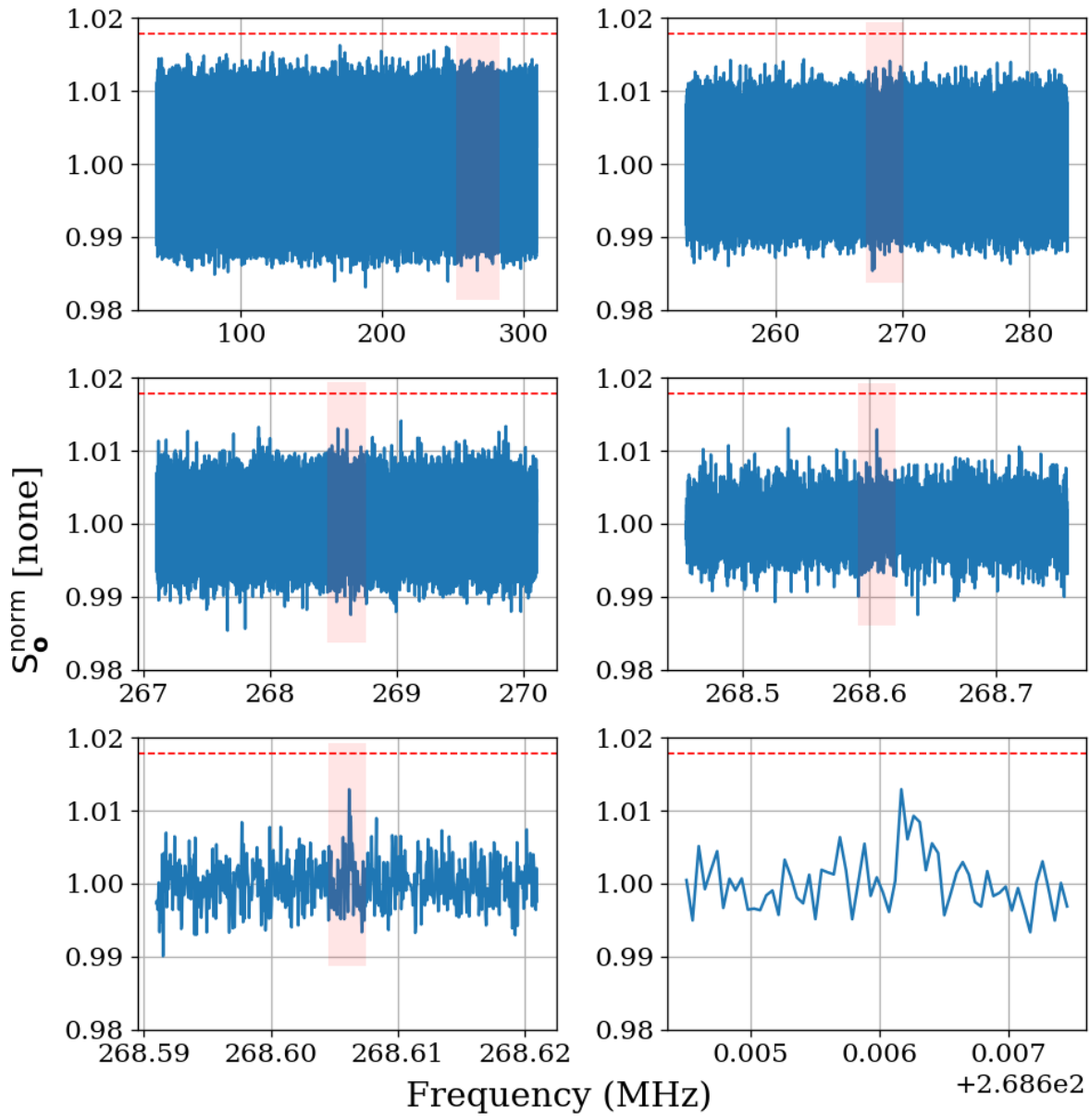


Figure 4.18: Normalized, output-referred power spectrum from hardware injection test. Injected signal at 268.60608MHz. Light pink boxes show zoom level on following plot. Red dashed line indicates the 5% significance threshold, derived in Sec. 2.2.1. Signal is not detectable above threshold.

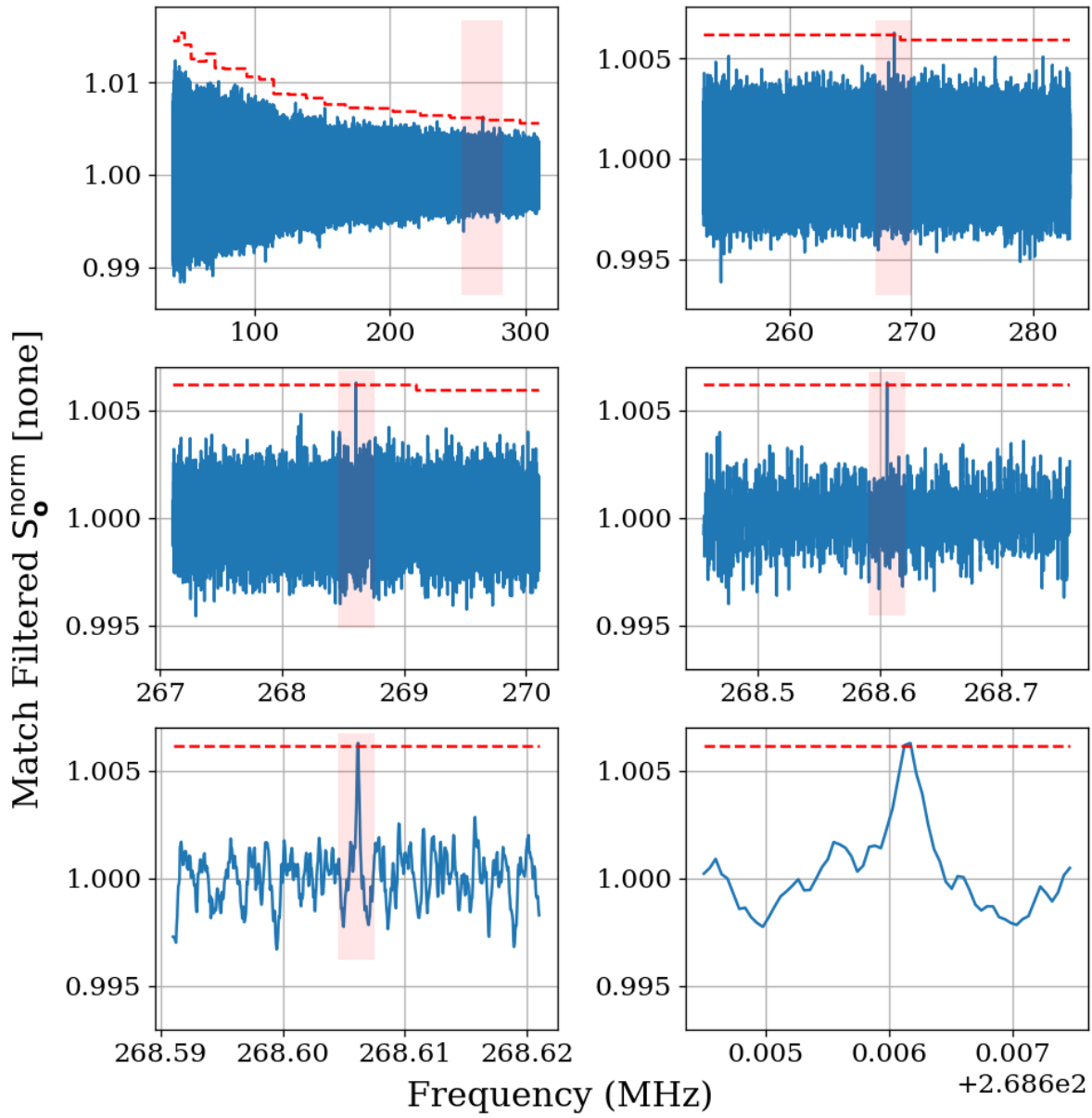


Figure 4.19: Matched filtered, output-referred power spectrum from hardware injection test. Injected signal at 268.60608MHz. Light pink boxes show zoom level on following plot. Red dashed line indicates the 5% significance threshold, derived in Sec. 2.2.1. Introducing the matched filter pushed signal above detectable above threshold compared to Fig. 4.18.

1812 **4.5 Results**⁹

1813 In this section, we report a 95%, frequency-dependent, exclusion limit on the kinetic mixing
1814 strength ϵ of the dark photon (Fig. 4.20). We discuss uncertainties on measured data, identi-
1815 fication of a candidate signal and our process to exclude it. Finally, we display our results in
1816 context by plotting these new limits on top of an aggregation of existing limits in Fig. 4.21.
1817 Future runs of this experiment from 0.3-14 GHz in similar room temperature RF enclosures
1818 and 100 K noise temperature LNAs are indicated (the foundation for such a system is out-
1819 lined in Ch. 5). We have only indicated planned runs, however at microwave frequencies,
1820 highly resonant cryogenic cavities and cryogenic LNAs as well as sub-THz instrumentation
1821 are feasible and could result in an order of magnitude improvement in the limit over the
1822 indicated frequency range and beyond.

1823 **4.5.1 Discussion of uncertainties**

1824 The systematic uncertainty in this experiment comes primarily from three sources, listed in
1825 order of their contribution from greatest to least:

- 1826 1. Fractional uncertainty on the simulated antenna aperture, which is discussed in Sec. 4.3.3,
1827 $\approx 60\%$
- 1828 2. Fractional uncertainty on the first-stage amplifier noise temperature, $\approx 10\%$
- 1829 3. Fractional uncertainty on the gain of the amplifier chain, $\approx 5\%$

⁹Code for this section can be found at: <https://github.com/josephmlev/darkRadio/tree/master/COMPUTELIMIT>

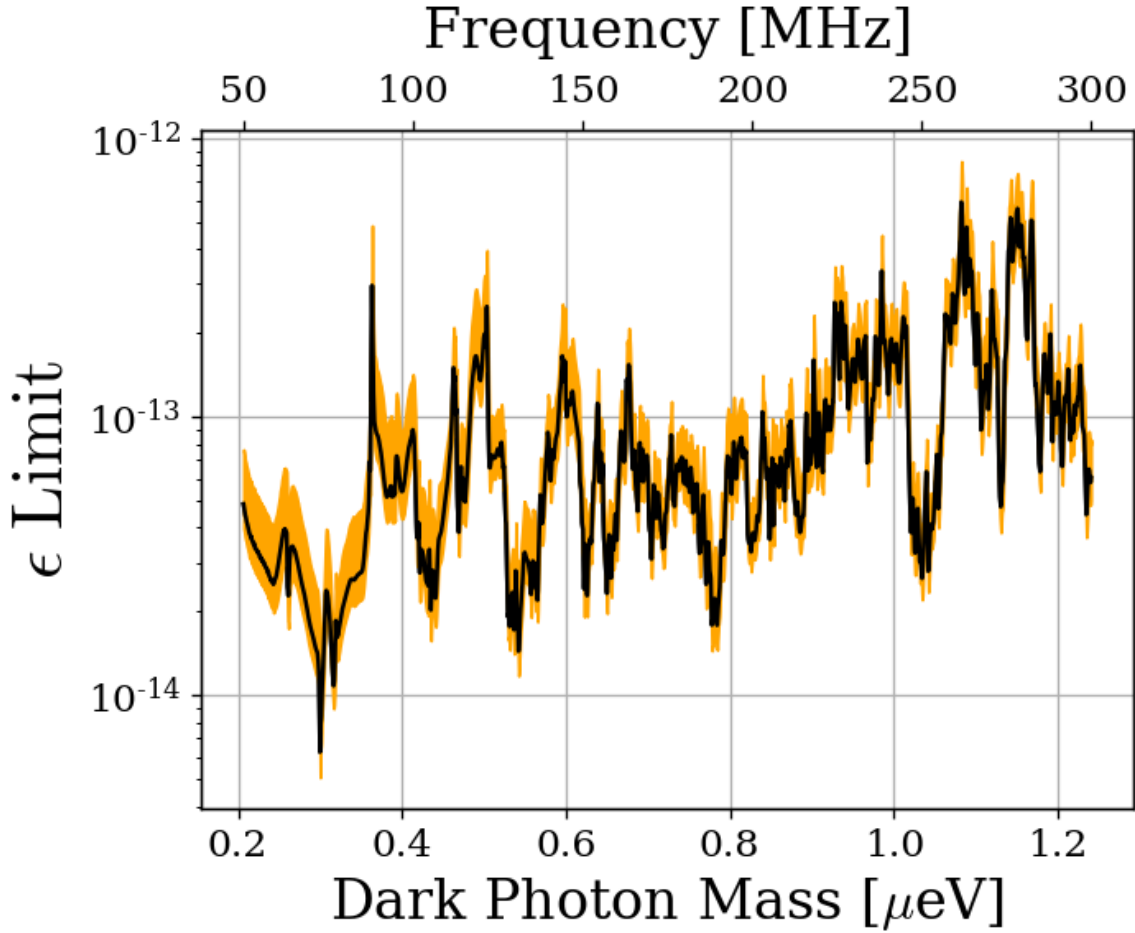


Figure 4.20: 95 % exclusion limit on ϵ with uncertainty shown in orange shaded region. This is based on a local dark matter density of $\rho_{\text{DM}} = 0.45 \text{ GeV/cm}^3$. The error estimate does not take the comparatively small gain and amplifier noise temperature errors into account.

1830 The uncertainty on the simulated antenna aperture is significantly larger than the other

1831 two, and so we neglect them in the uncertainty in the ϵ limit.

1832 We follow the convention of similar experiments where we fix the value of ρ_{DM} and

1833 solve for an ϵ limit given this value. Therefore we treat ρ_{DM} as a known constant with no

1834 uncertainty.

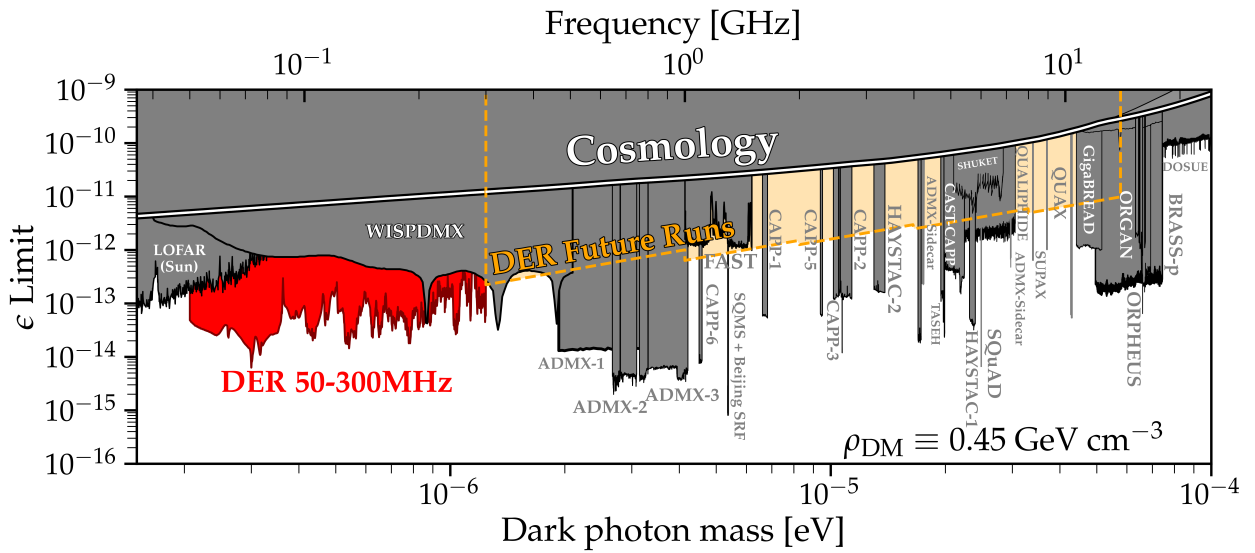


Figure 4.21: Dark photon limits of various experiments circa August 2024, with this work shown in red. The ragged lower bound is due to the complex structure of the resonant modes of the shielded room. Plot adapted by Ben Godfrey from [72] using code found at [73] and includes limit projections of various axion experiments. Astrophysical limits such as CMB interactions with the dark photon are in the region labeled *Cosmology*. Planned wideband extensions of our experiment search from 0.3-14 GHz in similar room temperature RF enclosures are indicated (*yellow*).

₁₈₃₅ Chapter 5

₁₈₃₆ Beyond 300 MHz

To infinity and beyond!

₁₈₃₇

Buzz Lightyear

₁₈₃₈ Where does this experiment go in the future?

₁₈₃₉ **5.1 Preliminary Run 1B results**

₁₈₄₀ **5.2 Mixer System**

₁₈₄₁ **5.3 Cryogenics**

¹⁸⁴² Appendix A

¹⁸⁴³ Overview of RTSA code base

¹⁸⁴⁴ A basic overview of the code which are used to acquire and process data are outlined here.

¹⁸⁴⁵ The version control is very simple and each experiment has it's own directory containing

¹⁸⁴⁶ several key files. The general usage template from which other experiments can be developed

¹⁸⁴⁷ is in the `teledyneTemplate` directory. The important files, in order of importance, are

¹⁸⁴⁸ • `settings.py`: Settings are controlled from this file. If the DAQ code isn't to be

¹⁸⁴⁹ modified, this is all the user must interact with in normal usage. While it is a python

¹⁸⁵⁰ script, it functions more like a text file. Descriptions and notes about allowed values

¹⁸⁵¹ are included as comments. Read them carefully, settings can conflict.

¹⁸⁵² • `drDaq*.py`: Main script which calls all the helper functions. To take data, run this

¹⁸⁵³ script after modifying (and saving) `settings.py`. There is usually a suffix indicating

¹⁸⁵⁴ the date and information about version.

¹⁸⁵⁵ • `avgFftModule.py`: This is modified code from teledyne. It handles all the heavy

1856 lifting: Interfacing with the C++ API, pinning GPU memory, transfer of data from
1857 PCIE card to the GPU, computation of the FFT on the GPU. This is all wrapped in
1858 a class called `avgFft`. An instance of this class is called `avgSpec` and is the workhorse
1859 of `drDaq.py`

1860 • `daqHelpers.py`: Lots of helper functions which are separated here to keep other code
1861 clean. It is imported as a module in other files. Lots of useful code lives in here,
1862 including the code that converts time series to power spectra (normalization is non-
1863 trivial, see Eq. 2.15), writes info to `database.txt`, saves the pre-averaged spectra
1864 including metadata in an HDF5 file.

1865 • `plotTesting.py`: This uses `dash` to host a web app which allows interactive `plotly`
1866 graphs for simple visualisation of run data. This is extremely useful as it can tell you
1867 if amplifiers die. Without this, all data would have to be averaged and more fully
1868 analyzed, but this is a good light-weight option. There is some creative use of data
1869 down sampling so it runs quickly while not removing any candidates. An example
1870 window is shown in Fig. A.1.

1871 • `backup.sh`: Simple shell script which backs up run data to locations of your choosing.
1872 In the `teledyneTemplate` directory, it is set up to back up to the secondary hard disk
1873 drive in the DR2 machine, and to peloton, but this can be easily modified. When taking
1874 real data, this script should not be run at the same time as `drDaq.py`. `backup.sh`
1875 should be run first, so it completes while the antenna is moved and batteries changed.
1876 This ensures there is not a heavy load on the hard drive due to back ups while data

1877 acquisition is ongoing. `valonInit.py`: sets up the valon signal generator to work as a
1878 clock. This should probably be a function inside of `daqHelpers.py`, but there may have
1879 been a reason I kept it separate.

1880 • `gdrapi.py` Comes from Teledyne. Defines functions for the api. I have not modified
1881 it at all.

1882 • `helperCupy.py` Comes from Teledyne. Defines functions for the GPU. I have not
1883 modified it at all.

1884 • `streamingHelpers.py` comes from Teledyne. Defines functions for streaming from
1885 PCIE card to GPU. I have not modified it at all.

1886 A Tips for using the RTSA system

1887 • As of September 2024, you must boot into kernel version 5.15.

1888 • Make sure to run `insmod.sh` in the `teledyneInstall/gdrcopy` directory after restart-
1889 ing the machine.

1890 – look at `teledyneInstall/installGuide.txt` on how to handle common errors
1891 involving this process.

1892 • Read through the `settings.txt` file carefully! Some settings will conflict with others,
1893 but they are mostly noted. There are also some notes about possible upgrades which
1894 could be made, some of which without much effort.

1895 **B Data structure and processing**

1896 Figure 2.36 shows the handling of data as it comes in as an RF time series and is converted
1897 to pre-averaged spectra. While significantly less cumbersome than the raw data, processing
1898 these spectra still represents a challenge. This subsection outlines how I have attempted to
1899 handle it. While it is a little convoluted, this is the third iteration of how to handle this
1900 data processing and is likely simpler than it seems on first blush. In other words, there is
1901 probably a better way to do this, but don't knock it til you try it.

1902 **B.1 Writing data**

1903 Once a pre-averaged spectrum is computed by dividing the running sum by `NOF_BUFFERS_TO_RECEIVE`,
1904 this can be written to an HDF5 file. Whether or not it is, can be controlled by the `SAVE_H5`
1905 boolean variable¹. Each pre-averaged spectrum is uniquely specified by `ACQ_NUM` in a given
1906 data run. In order to simplify backups and avoid placing all our eggs in one HDF5 basket,
1907 `NUM_SPEC_PER_FILE`² pre-averaged spectra are saved into a single HDF5 file, before starting
1908 a new file. These files are simply named as a zero-indexed number followed by their `.hdf5`
1909 extension. These files are saved in `SAVE_DIRECTORY`³. I usually make this save directory in
1910 a secondary SSD named `drBiggerBoy` in order to preserve the main drive. I think the stress

¹This variable exists because when testing things or taking miscellaneous measurements, you will frequently want to acquire a single spectrum without engaging the complex machinery of the HDF5 saving procedure.

²I have kept this around 16 and not experimented much outside of this range, but it's probably fine. This keeps the files around 1 GB. For run 1.4, this is about 45 minutes of antenna data and 3 minutes of terminator data per file, so if a file is corrupted it's not a big deal. I have never had a problem, this is paranoia inherited from Ben.

³A reminder that this is specified, like all other variables, in `settings.py`. Note you must create this directory ahead of time and include a sub-directory called `data`. It says this in the comments of `settings.py` which you are reading, right?

1911 of continuous reads and writes will probably kill this drive, so I prefer to keep it separate
1912 from the main boot drive, drBigBoy.

1913 When `SAVE_H5 == 1`, a `database.txt` file is created in `SAVE_DIRECTORY`, shown in Table
1914 A.1.

Attribute	Pre-averaged spectrum 0	Pre-averaged spectrum 1
ACQ_NUM	0	1
DATETIME	2023-05-10 11:32:48.365	2023-05-10 11:35:49.193
SWITCH POS	0	1
ANT POS IDX	0	0
TEMP	295.64	295.54
LEN FFT LOG2	24	24
SAMPLE RATE MHZ	800.0	800.0
NOF BUFFERS	8600	8600
AMP1	1012_E_PbAcid	1012_E_PbAcid
AMP2	ZKL_9p05VReg	ZKL_9p05VReg
LPF	HSP50+	HSP50+
HPF	288S+	288S+
ATTENUATOR	4dB_FIXED	4dB_FIXED
ADC	ADQ32	ADQ32
CLOCK	SRS_VIA_VALON	SRS_VIA_VALON
File Number	0	0

Table A.1: Example database file from run 1.4. In this run, `ACQ_NUM` counts up to 4175, and these spectra are saved between 261 HDF5 files. Some of the values are auto-generated (`temp`, `DATETIME`, etc.) while others are manually entered into `settings.txt` (`AMP1`, `LPF`, etc.) Note that this table has been transposed in order to fit on the page.

1915 When setting up a data run, you must test that the data are saved how you expect. I have
1916 had success by reducing `NOF_BUFFERS_TO_RECEIVE` to a small number⁴, and taking a simu-
1917 lated data run. The process of switching is hacked together and can give you unpredictable

⁴`NOF_BUFFERS_TO_RECEIVE` times the time per buffer must be larger than around 2 seconds or it will crash

1918 results. Did I mention to read the comments in `settings.py`?

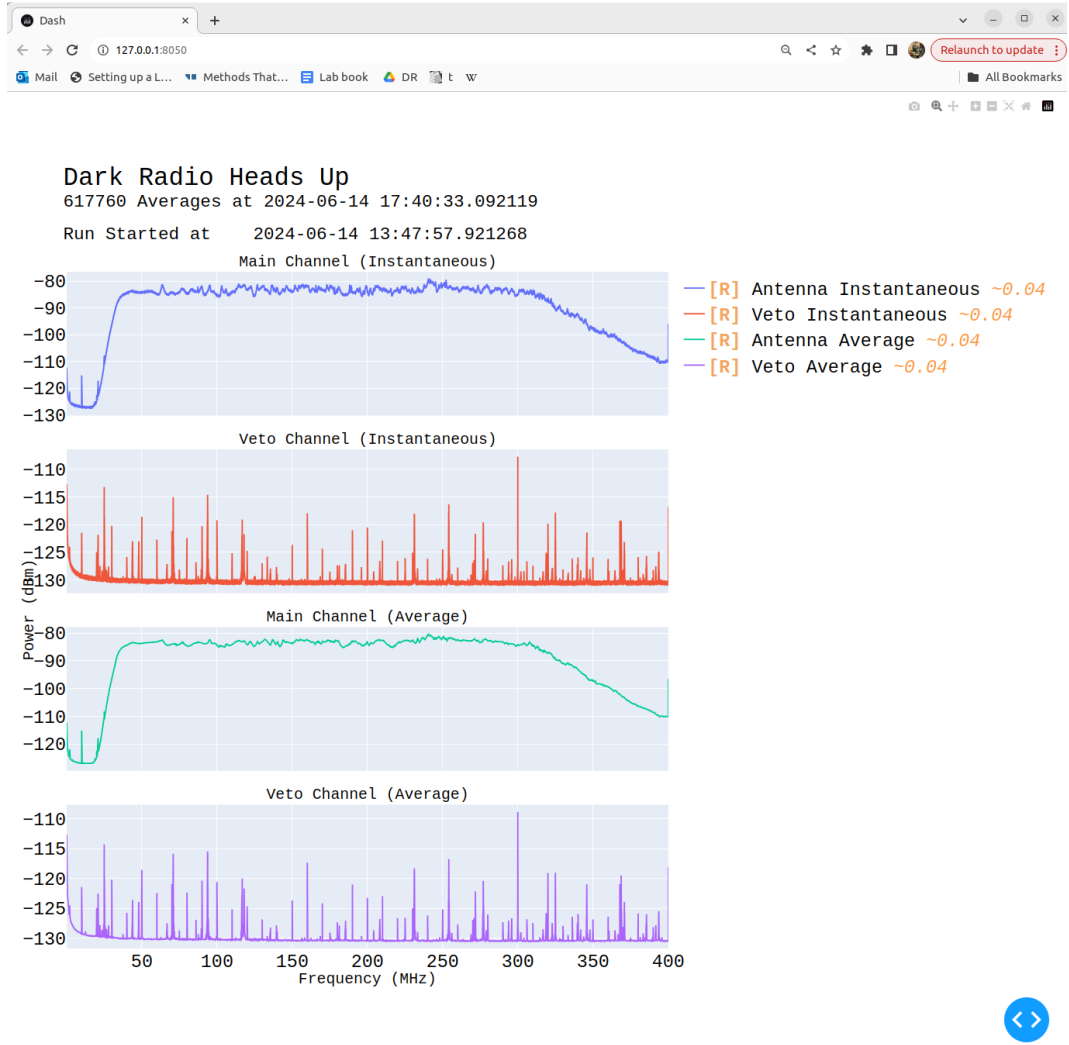


Figure A.1: Real time heads up window for data acquisition. Built with Plotly and Dash, and displays in web browser, in this case Google Chrome. Spectra contain 2^{23} frequency bins, so are down-sampled so as to display 10^4 bins at any given level of zoom. This allows for interaction with the plot in real time with very little lag. The resolution currently displayed (in MHz) is shown in yellow next to the legend (right of first plot). This down-sampling is "smart" in that it will show any excursions, and is implemented with the `plotlyResampler` package in `MinMaxAggregator` mode. Mousing over a curve causes a "Tooltip" to appear, indicating the frequency and power at that point in the curve. The frequency axes are all linked, so zooming on one plot will cause all plots to display the same frequency range. Icons on upper right allow for navigation of plot. Frustratingly there is no back button, so be careful when zooming on a very narrow feature; a wrong move means you have to go all the way back out and start over.

1919 **B.2 Reading and averaging data**⁵

1920 After taking a data run, you should have a `SAVE_DIRECTORY` containing a directory full of
1921 many HDF5 files and a `database.txt` file (and possibly a directory of plotting spectra if
1922 that is chosen in `settings.txt`. The basic idea is to “pre-process” the HDF5 files into a
1923 single, large HDF5 file which can be more quickly accessed to compute a single, averaged
1924 S_o spectrum for further analysis (see next chapter). The `database.txt` file is loaded into
1925 python as a pandas dataframe in order to find specific spectra in this large data structure.

1926 I tried (for a while) to keep the files separate to allow for multi-processing to speed up
1927 the averaging, but I ran into issues. The most serious issue is that all the files live on the
1928 same drive, so you can’t get much of a speed up since the drive is read-limited to around
1929 500 MB/s. I found multiprocessing is more effort than it’s worth. It takes about 20 minutes
1930 to pre-average run 1.4 (9 days of data, 3 minute pre-averages yields 4175 spectra which take
1931 about 280 GB), and you only have to do this once after a run.

1932 Following the example of `run1p4_packAvgAllAnalysis.ipynb`, the first step is to load
1933 `database.txt` as a pandas dataframe which can be used to index the pre-processed file.
1934 Next, a list of which `ACQ_NUMs` correspond to an antenna and terminator must be computed,
1935 after removing any which are known to be contaminated⁶. The list of indices which are
1936 to be averaged together is called either `antIdx` or `termIdx`. Note that you can devise any
1937 number of ways to generate these lists, or even hard code them. The code given is just an

⁵Code for this section can be found at: https://github.com/josephmlev/darkRadio/tree/master/daqAnalysisAndExperiments/run1p4/run1p4_analysis/run1p4_packAvgAllAnalysis.ipynb

⁶In run 1.4, the first antenna and terminator spectra are thrown out, since the computer monitor was on to verify the run started successfully. This was out of paranoia and probably didn’t do anything.

1938 example.

1939 Next, info in the dataframe (no power spectra data yet) are analyzed as a sanity check.

1940 These are not super important but a good check.

1941 The cell beginning with the comment `#pack pre proc dataset` is where the heavy lifting
1942 happens. A large HDF5 file is initialized. It contains two datasets, one for each channel
1943 (main experiment and veto in run 1.4). Note that in this example, it is hard coded to expect
1944 8388609 frequency bins ($2^{23} + 1$), and this must be changed if doing something other than a
1945 2^{24} -point FFT. The HDF5 sub-files are iterated over, their data is read, and written into the
1946 pre-processed HDF5 file. Make sure not to remove the error handling for closing the HDF5
1947 file, or you will corrupt it and have to rerun the pre-processing.

1948 Now that the pre-processed HDF5 file has been packed with data and a list of indices
1949 to be averaged has been generated, averaging is trivial (though still takes a few minutes, so
1950 maybe test it with a sub set of `antIdx`. The code is provided below:

```
1951
1952 def avgSpecFromPacked(avgIdxs, specStr):
1953     sum = np.zeros(2**23+1)
1954     for i in avgIdxs:
1955         sum += f[specStr][:,i]
1956     avgSpec = sum/(len(avgIdxs))
1957
1958     return avgSpec
```

Listing A.1: Python function for averaging spectra from pre-processed data

1959 Note that this assumes a single HDF5 file, `f`, is in scope. `specStr` is a string which
1960 specifies which channel to average, for example `spec_W_chA`.

1961 The output of this function is S_o which can be passed to following functions for further
1962 analysis.

¹⁹⁶³ Bibliography

- 1964 [1] Fritz Zwicky. “The Redshift of Extragalactic Nebulae”. In: (1933).
- 1965 [2] Vera C. Rubin and Jr. Ford W. Kent. “Rotation of the Andromeda Nebula from a
1966 Spectroscopic Survey of Emission Regions”. In: (1970).
- 1967 [3] Marco Battaglieri *et al.* *US Cosmic Visions: New Ideas in Dark Matter 2017: Community Report*. 2017. DOI: 10.48550/ARXIV.1707.04591. URL: <https://arxiv.org/abs/1707.04591>.
- 1970 [4] Benjamin Godfrey et al. “Search for dark photon dark matter: Dark E field radio pilot
1971 experiment”. In: *Phys. Rev. D* 104 (1 July 2021), p. 012013. DOI: 10.1103/PhysRevD.
1972 104.012013. URL: <https://link.aps.org/doi/10.1103/PhysRevD.104.012013>.
- 1973 [5] E. E. Barnard and A. C. Ranyard. “Structure of the Milky Way”. In: *Knowledge: An
1974 Illustrated Magazine of Science* 17 (Nov. 1894), p. 253.
- 1975 [6] Kelvin, William Thomson, Baron. *Baltimore Lectures on Molecular Dynamics and the
1976 Wave Theory of Light*. English. Collection: University of California Libraries. London,
1977 Baltimore: C. J. Clay and sons; Publication agency of the Johns Hopkins University,
1978 1904, pp. xxi, 703. URL: <https://archive.org/details/baltimorelecture00kelvrich>.

- 1979 [7] Richard H. Maurer. “The Idea Man”. In: *SLAC Beam Line* 31.1 (2001). Accessed:
1980 2024-06-23. URL: <https://www.slac.stanford.edu/pubs/beamline/31/1/31-1-maurer.pdf>.
- 1982 [8] Anthony Tyson. “Mapping Dark Matter with Gravitational Lenses”. In: *Physics Today* 45.6 (June 1992), pp. 24–32. ISSN: 0031-9228. DOI: 10.1063/1.881309. eprint: https://pubs.aip.org/physicstoday/article-pdf/45/6/24/11176778/24_1_online.pdf. URL: <https://doi.org/10.1063/1.881309>.
- 1986 [9] R. Clausius. “XVI. On a mechanical theorem applicable to heat”. In: *The London, Edinburgh, and Dublin Philosophical Magazine and Journal of Science* 40.265 (1870),
1987 pp. 122–127. DOI: 10.1080/14786447008640370. eprint: <https://doi.org/10.1080/14786447008640370>. URL: <https://doi.org/10.1080/14786447008640370>.
- 1990 [10] Herbert Goldstein, Charles P. Poole, and John L. Safko. *Classical Mechanics*. 3rd. San
1991 Francisco: Addison-Wesley, 2002. ISBN: 9780201657029.
- 1992 [11] A. S. Eddington. “The Kinetic Energy of a Star Clusters”. In: *Monthly Notices of*
1993 *the Royal Astronomical Society* 76.6 (Apr. 1916), pp. 525–528. ISSN: 0035-8711. DOI:
1994 10.1093/mnras/76.6.525. eprint: <https://academic.oup.com/mnras/article-pdf/76/6/525/18494199/mnras76-0525.pdf>. URL: <https://doi.org/10.1093/mnras/76.6.525>.
- 1997 [12] Gianfranco Bertone and Dan Hooper. “History of dark matter”. In: *Reviews of Modern*
1998 *Physics* 90.4 (2018), p. 045002.

- 1999 [13] F. D. Kahn and L. Woltjer. “Intergalactic Matter and the Galaxy.” In: *American
2000 Journal of Physics* 130 (Nov. 1959), p. 705. doi: 10.1086/146762.
- 2001 [14] Hugo van Woerden and Richard G. Strom. “The beginnings of radio astronomy in
2002 the Netherlands”. In: *Journal of Astronomical History and Heritage* 9.1 (June 2006),
2003 pp. 3–20.
- 2004 [15] Virginia Trimble. “History of Dark Matter in Galaxies”. In: *Planets, Stars and Stel-
2005 lar Systems: Volume 5: Galactic Structure*. Ed. by Gerard Gilmore. New York, NY:
2006 Springer, 2013, pp. 1093–1116.
- 2007 [16] V. Radeka. “Signal, Noise and Resolution in Position-Sensitive Detectors”. In: *IEEE
2008 Transactions on Nuclear Science* 21.1 (1974), pp. 51–64. doi: 10.1109/TNS.1974.
2009 4327444.
- 2010 [17] B. M. Brubaker et al. “HAYSTAC axion search analysis procedure”. In: *Physical Re-
2011 view D* 96.12 (Dec. 2017). doi: 10.1103/physrevd.96.123008. URL: <https://doi.org/10.1103%2Fphysrevd.96.123008>.
- 2013 [18] C. Boutan et al. *Axion Dark Matter eXperiment: Run 1A Analysis Details*. 2023. arXiv:
2014 2312.16668.
- 2015 [19] Maximiliano Silva-Feaver et al. “Design Overview of DM Radio Pathfinder Experi-
2016 ment”. In: *IEEE Transactions on Applied Superconductivity* 27.4, 2631425 (June 2017),
2017 p. 2631425. doi: 10.1109/TASC.2016.2631425.
- 2018 [20] David Hill. “Plane Wave Integral Representation for Fields in Reverberation Cham-
2019 bers”. en. In: 40 (1998-08-01 00:08:00 1998).

- 2020 [21] W. L. Stutzman and G. A. Thiele. *Antenna Theory and Design*. John Wiley Sons,
- 2021 1998.
- 2022 [22] J.D. Kraus. *Antennas*. McGraw-Hill, 1950. ISBN: 07-035410-3.
- 2023 [23] H. Nyquist. “Thermal Agitation of Electric Charge in Conductors”. In: *Phys. Rev.* 32
2024 (1 July 1928), pp. 110–113. DOI: 10.1103/PhysRev.32.110. URL: <https://link.aps.org/doi/10.1103/PhysRev.32.110>.
- 2025
- 2026 [24] J. B. Johnson. “Thermal Agitation of Electricity in Conductors”. In: *Phys. Rev.* 32 (1
2027 July 1928), pp. 97–109. DOI: 10.1103/PhysRev.32.97. URL: <https://link.aps.org/doi/10.1103/PhysRev.32.97>.
- 2028
- 2029 [25] Robert H Dicke. “The measurement of thermal radiation at microwave frequencies”.
2030 In: *Review of Scientific Instruments* 17.7 (1946), pp. 268–275.
- 2031 [26] Albert Einstein. “Über die von der molekularkinetischen Theorie der Wärme geforderte
2032 Bewegung von in ruhenden Flüssigkeiten suspendierten Teilchen”. In: *Annalen der
2033 Physik* 322.8 (1905), pp. 549–560.
- 2034 [27] Herbert B. Callen and Theodore A. Welton. “Irreversibility and Generalized Noise”.
2035 In: *Phys. Rev.* 83 (1 July 1951), pp. 34–40. DOI: 10.1103/PhysRev.83.34. URL:
2036 <https://link.aps.org/doi/10.1103/PhysRev.83.34>.
- 2037 [28] C. L. Mehta. “Coherence-time and effective bandwidth of blackbody radiation”. In:
2038 *Il Nuovo Cimento (1955-1965)* 28.2 (1963), pp. 401–408. DOI: 10.1007/BF02828589.
2039 URL: <https://doi.org/10.1007/BF02828589>.

- 2040 [29] Raphael Cervantes et al. *Deepest Sensitivity to Wavelike Dark Photon Dark Matter*
2041 *with SRF Cavities*. 2022. arXiv: 2208.03183 [hep-ex].
- 2042 [30] Alexander V. Gramolin et al. “Spectral signatures of axionlike dark matter”. In: *Physi-*
2043 *cal Review D* 105.3 (Feb. 2022). ISSN: 2470-0029. DOI: 10.1103/physrevd.105.035029.
2044 URL: <http://dx.doi.org/10.1103/PhysRevD.105.035029>.
- 2045 [31] Michael S. Turner. “Periodic signatures for the detection of cosmic axions”. In: *Phys.*
2046 *Rev. D* 42 (10 Nov. 1990), pp. 3572–3575. DOI: 10.1103/PhysRevD.42.3572. URL:
2047 <https://link.aps.org/doi/10.1103/PhysRevD.42.3572>.
- 2048 [32] Greg Durgin. *Lecture on Noise Figure*. Accessed: 2024-06-23. 2017. URL: https://www.youtube.com/watch?v=M_SRUF4TQgA.
- 2049 [33] Pasternack Enterprises. *PE15A1012: 1 Watt Amplifier Operating From 0.01 GHz to*
2050 *6 GHz*. Accessed: 2024-05-17. 2024. URL: <https://www.pasternack.com/images/>
2051 *ProductPDF/PE15A1012.pdf*.
- 2052 [34] SP Devices. *ADQ32 Datasheet*. Accessed: 2024-06-23. 2024. URL: https://www.spdevices.com/en-us/Products_/Documents/ADQ32/20-2378%20ADQ32%20datasheet.pdf.
- 2053 [35] Benjamin Godfrey. “A Novel Search for Dark Photons”. Ph.D. dissertation. UC Davis,
2054 2022. URL: <https://escholarship.org/uc/item/72b776v4>.
- 2055 [36] Joseph Levine et al. *New Limit on Dark Photon Kinetic Mixing in the 0.2-1.2 μeV*
2056 *Mass Range From the Dark E-Field Radio Experiment*. 2024. arXiv: 2405.20444
2057 [hep-ex]. URL: <https://arxiv.org/abs/2405.20444>.

- 2061 [37] L.A. Wainstein and V.D. Zubakov. *Extraction of Signals from Noise*. Englewood Cliffs,
2062 NJ: Prentice-Hall, 1962. ISBN: 9780132981330.
- 2063 [38] Andy Marvin and Simon Jonathan Bale. “Thermal Noise Measurements in a Rever-
2064 beration Chamber”. English. In: *IEEE Transactions on Electromagnetic Compatibility*
2065 64.3 (June 2022). © 2022 IEEE. This is an author-produced version of the published
2066 paper. Uploaded in accordance with the publisher’s self-archiving policy. Further copy-
2067 ing may not be permitted; contact the publisher for details, pp. 893–896. ISSN: 0018-
2068 9375. DOI: 10.1109/TEMC.2022.3142937.
- 2069 [39] F. Reif. *Fundamentals of Statistical and Thermal Physics*. Long Grove, IL: Waveland
2070 Press, 2009. ISBN: 9781577666127.
- 2071 [40] *Series 83 RF Shielded Enclosure*. Lindgren R.F. Enclosures, Inc. 2021. URL: <https://www.ets-lindgren.com/datasheet/shielding/rf-shielding-and-accessories/11003/1100307>.
- 2074 [41] David A. Hill. *Electromagnetic Theory of Reverberation Chambers*. Technical Note
2075 1506. Gaithersburg, MD: National Institute of Standards and Technology, 1998. URL:
2076 https://tsapps.nist.gov/publication/get_pdf.cfm?pub_id=24427.
- 2077 [42] D.A. Hill. “A reflection coefficient derivation for the Q of a reverberation chamber”. In:
2078 *IEEE Transactions on Electromagnetic Compatibility* 38.4 (1996), pp. 591–592. DOI:
2079 10.1109/15.544314.

- 2080 [43] Lawrence Krauss et al. “Calculations for cosmic axion detection”. In: *Physical Review*
2081 *Letters* 55.17 (1985), pp. 1797–1800. DOI: 10.1103/PhysRevLett.55.1797. URL:
2082 <https://doi.org/10.1103/PhysRevLett.55.1797>.
- 2083 [44] *Biconical Antenna AB-900A*. Rev. D05.19. Com-Power Corporation. May 2019. URL:
2084 <https://documentation.com-power.com/pdf/AB-900A-1.pdf>.
- 2085 [45] *COMSOL Multiphysics*. 5.4. Available at <https://www.comsol.com/>. COMSOL, Inc.
2086 One First Street, Suite 4 Los Altos, CA 94022.
- 2087 [46] Zhong Chen and Michael D. Foegelle. “A numeric investigation of ground plane effects
2088 on biconical antenna factor”. In: *Electromagnetic Compatibility, 1998. 1998 IEEE In-*
2089 *ternational Symposium on*. Vol. 2. IEEE. IEEE, 1998, pp. 802–806. DOI: 10.1109/
2090 ISEMC.1998.750302. URL: <https://ieeexplore.ieee.org/document/750302>.
- 2091 [47] John D. Kraus. *Antennas*. 2nd. New York: McGraw-Hill, 1988, p. 892. ISBN: 9780070354227.
- 2092 [48] Mini-Circuits. *ZKL-1R5: 50 Ω Gain Block Amplifier*. Accessed: 2024-06-23. 2024. URL:
2093 <https://www.minicircuits.com/pdfs/ZKL-1R5.pdf>.
- 2094 [49] Texas Instruments. *LM317: 3-Terminal Adjustable Regulator*. Accessed: 2024-06-23.
2095 2024. URL: <https://www.ti.com/lit/ds/symlink/lm317.pdf?ts=1720749307506>.
- 2096 [50] Alan V. Oppenheim, Alan S. Willsky, and S. Hamid Nawab. *Signals and Systems*. 2nd.
2097 Upper Saddle River, NJ: Prentice Hall, 1996. ISBN: 978-0138147570.
- 2098 [51] Mini-Circuits. *ZX75LP-288-S+: Low Pass Filter*. Accessed: 2024-06-23. 2024. URL:
2099 <https://www.minicircuits.com/pdfs/ZX75LP-288-S+.pdf>.

- 2100 [52] Mini-Circuits. *SHP-50+: High Pass Filter*. Accessed: 2024-06-23. 2024. URL: <https://www.minicircuits.com/pdfs/SHP-50+.pdf>.
- 2101
- 2102 [53] *Biconical Antenna*. AB-900A. Rev. D. Com-Power Corporation. May 2019.
- 2103 [54] *The Y Factor Technique For Noise Figure Measurements*. 1MA178. Version 5e. Rhode
- 2104 & Schwarz. Oct. 2021.
- 2105 [55] *Noise Figure Measurement Accuracy: The Y-Factor Method*. 1MA178. Version 5e.
- 2106 Keysight Technologies. Oct. 2021.
- 2107 [56] Wikipedia contributors. *Y-factor Sketch*. Accessed: 2024-06-23. 2024. URL: https://en.wikipedia.org/wiki/Y-factor#/media/File:Y-factor_sketch.jpg.
- 2108
- 2109 [57] Rigol Technologies. *RSA5000 Series: Real-Time Spectrum Analyzer Datasheet*. Ac-
- 2110 cessed: 2024-06-23. 2024. URL: https://beyondmeasure.rigoltech.com/acton/attachment/1579/f-0816/1/-/-/-/RSA5_datasheet.pdf.
- 2111
- 2112 [58] “IEEE Standard Method for Measuring the Effectiveness of Electromagnetic Shielding
- 2113 Enclosures”. In: *IEEE Std 299-1997* (1998), pp. 1–48. DOI: [10.1109/IEEESTD.1998.88115](https://doi.org/10.1109/IEEESTD.1998.88115).
- 2114
- 2115 [59] David W. Allan. “Statistics of atomic frequency standards”. In: *Proceedings of the*
- 2116 *IEEE 54.2* (1966), pp. 221–230.
- 2117 [60] Keysight Technologies. *Analyzing Frequency Stability in the Frequency and Time Do-*
- 2118 *mains*. Tech. rep. 5991-4797EN, August 11, 2014. USA: Keysight Technologies, 2014.

- 2119 [61] Stanford Research Systems. *FS725 Rubidium Frequency Standard Manual*. Accessed:
2120 2024-06-23. 2024. URL: <https://www.thinksrs.com/downloads/PDFs/Manuals/FS725m.pdf>.
- 2122 [62] R. H. Dicke. “The Measurement of Thermal Radiation at Microwave Frequencies”.
2123 In: *Rev. Sci. Instrum.* 17 (1946), p. 268. DOI: 10.1063/1.1770483. URL: <https://aip.scitation.org/doi/10.1063/1.1770483>.
- 2125 [63] S. Al Kenany et al. “Design and operational experience of a microwave cavity axion de-
2126 tector for the 20-100 micro-eV Range”. In: *Nuclear Instruments and Methods in Physics*
2127 *Research Section A: Accelerators, Spectrometers, Detectors and Associated Equipment*
2128 854 (May 2017), pp. 11–24. ISSN: 0168-9002. DOI: 10.1016/j.nima.2017.02.012.
2129 URL: <http://dx.doi.org/10.1016/j.nima.2017.02.012>.
- 2130 [64] G. Turin. “An introduction to matched filters”. In: *IRE Transactions on Information*
2131 *Theory* 6.3 (1960), pp. 311–329. DOI: 10.1109/TIT.1960.1057571.
- 2132 [65] Robert N McDonough and Anthony D Whalen. *Detection of signals in noise*. Academic
2133 Press, 1995.
- 2134 [66] S. Asztalos et al. “Large-scale microwave cavity search for dark-matter axions”. In:
2135 *Phys. Rev. D* 64 (9 Oct. 2001), p. 092003. DOI: 10.1103/PhysRevD.64.092003. URL:
2136 <https://link.aps.org/doi/10.1103/PhysRevD.64.092003>.
- 2137 [67] G. Orjubin et al. “Statistical model of an undermoded reverberation chamber”. In:
2138 *IEEE Transactions on Electromagnetic Compatibility* 48.1 (2006), pp. 248–251. DOI:
2139 10.1109/TEMC.2006.870705.

- 2140 [68] Charles F. Bunting. *Statistical Characterization and Simulation of a Reverberation*
2141 *Chamber Using Finite-Element Techniques*. Tech. rep. 20060022547. NASA Techni-
2142 cal Reports Server (NTRS), 2006. URL: <https://ntrs.nasa.gov/citations/20060022547>.
- 2143
- 2144 [69] Philippe Besnier, Christophe Lemoine, and Jerome Sol. “Various estimations of com-
2145 posite Q-factor with antennas in a reverberation chamber”. In: *2015 IEEE Interna-*
2146 *tional Symposium on Electromagnetic Compatibility (EMC)*. 2015, pp. 1223–1227. DOI:
2147 [10.1109/ISEMC.2015.7256344](https://doi.org/10.1109/ISEMC.2015.7256344).
- 2148 [70] R. Khatiwada et al. “Axion Dark Matter Experiment: Detailed design and operations”.
2149 In: *Review of Scientific Instruments* 92.12 (Dec. 2021), p. 124502. ISSN: 0034-6748.
2150 DOI: [10.1063/5.0037857](https://doi.org/10.1063/5.0037857). eprint: https://pubs.aip.org/aip/rsi/article-pdf/doi/10.1063/5.0037857/16136265/124502\1_online.pdf. URL: <https://doi.org/10.1063/5.0037857>.
- 2151
- 2152
- 2153 [71] Yuqi Zhu et al. “An improved synthetic signal injection routine for the Haloscope
2154 At Yale Sensitive To Axion Cold dark matter (HAYSTAC)”. In: *Review of Scientific*
2155 *Instruments* 94.5 (May 2023). ISSN: 1089-7623. DOI: [10.1063/5.0137870](https://doi.org/10.1063/5.0137870). URL: [http://dx.doi.org/10.1063/5.0137870](https://dx.doi.org/10.1063/5.0137870).
- 2156
- 2157 [72] Andrea Caputo et al. “Dark photon limits: A handbook”. In: *Phys. Rev. D* 104 (9
2158 Nov. 2021), p. 095029. DOI: [10.1103/PhysRevD.104.095029](https://doi.org/10.1103/PhysRevD.104.095029). URL: <https://link.aps.org/doi/10.1103/PhysRevD.104.095029>.
- 2159

2160 [73] Ciaran O'Hare. *cajohare/AxionLimits*: *AxionLimits*. <https://cajohare.github.io/AxionLimits/>. Version v1.0. July 2020. DOI: 10.5281/zenodo.3932430.